THE ROLE OF TOPOLOGICAL DEFECTS AND TEXTURES IN THE KINETICS OF PHASE ORDERING

BY

MARTIN ZÁPOTOCKÝ

Dipl., Univerzita Karlova, 1989
M.A., Columbia University, 1992

THESIS

Submitted in partial fulfillment of the requirements
for the degree of Doctor of Philosophy in Physics
in the Graduate College of the
University of Illinois at Urbana-Champaign, 1996

Urbana, Illinois

UNIVERSITY OF ILLINOIS AT URBANA-CHAMPAIGN

THE GRADUATE COLLEGE

AUGUST 1996

WE HEREBY RECOMMEND THAT THE THESIS BY

MARTIN ZAPOTOCKY

ENTITLED THE ROLE OF TOPOLOGICAL DEFECTS AND TEXTURES IN THE KINETICS OF PHASE ORDERING

BE ACCEPTED IN PARTIAL FULFILLMENT OF THE REQUIREMENTS FOR THE DEGREE OF DOCTOR OF PHILOSOPHY

Paul M. Goldbart

Director of Thesis Research

Head of Department

Committee on Final Examination†

Yoshi Oono

Chairperson

Paul M. Goldbart

Dale J. Van Harlingen

John D Stack

† Required for doctor's degree but not for master's.

O-517

THE ROLE OF TOPOLOGICAL DEFECTS AND TEXTURES IN THE KINETICS OF PHASE ORDERING

Martin Zápotocký, Ph.D.
Department of Physics
University of Illinois at Urbana-Champaign, 1996
Paul M. Goldbart, Advisor

In this thesis, I present the results of a theoretical investigation of ordering processes induced by symmetry-breaking quenches in two physical systems. Both systems investigated possess a rich homotopy structure of the order-parameter space, which results in numerous topologically stable objects being generated during the quench, and influencing the properties of the system during the subsequent approach to equilibrium. The results reported are mostly computational in nature. The two systems investigated are (i) nematic liquid crystals, which support topologically stable abelian (in the uniaxial nematic case) and non-abelian (in the biaxial nematic case) singular defects, and (ii) the $O(3)$-symmetric vector (i.e., Heisenberg-type) system in 2 spatial dimensions, which supports topologically stable, but non-singular objects—topological textures.

In the case of nematic systems, the numerical investigation concentrates on the phase-ordering process and point defect dynamics following a quench into both the uniaxial and biaxial nematic phases of a quasi–2-dimensional liquid crystalline system. The time dependences of the correlation function, structure factor, energy density, and number densities of topological defects are computed. By comparing the growth laws for the characteristic length scales extracted from the order-parameter correlations and from the total number of topological defects in the system, it is determined that weak violations of dynamical scaling occur in the system, even at the latest times studied. The observed scaling violations are attributed to the presence of a logarithmic correction to the asymptotic power-law growth of the average inter-defect separation. Following the quench to the biaxial nematic phase, there are four topologically distinct defect species present in the system, the populations of which

are studied in detail. It is found that only two types of defect are observed in large numbers at late times, and a mechanism for the selection of the prevailing defect species is proposed.

In addition to the computational investigation of the phase ordering process in 2-dimensional nematic systems, analytical derivations of the singular (power-law) short-distance behavior of the contribution to the structure factor (i.e., the light scattering intensity) for all types of topologically stable defects encountered in 2- and 3-dimensional uniaxial and biaxial nematics are presented.

The second system studied—the Heisenberg-type model in 2 spatial dimensions—is first implemented numerically as the discretized $O(3)$ nonlinear σ-model with the standard form of free energy and with purely dissipative dynamics. Two distinct mechanisms for the decay of the order-parameter variations—single texture unwinding, and topological charge annihilation—are identified and characterized in this system. It is found that whereas at early times after the quench the annihilation process dominates, the unwinding processes become of comparable importance at later times. By examining the correlations in the order parameter and in the topological charge density, it is shown that dynamical scaling is strongly violated during the phase-ordering process, and multiple characteristic length-scales growing as distinct power-laws in time are identified.

In order to study in detail the origins of the observed multi-scaling behavior, the phase-ordering process is then studied within a modified $O(3)$ nonlinear σ-model with an additional free energy term (analogous to the so-called Skyrme term, familiar in high-energy physics) that stabilizes the textures against shrinking and unwinding. It is found that this modification influences the multi-scaling properties of the system in a dramatic way, and that with single-texture unwindings suppressed, the form of the spectrum of exponents characterizing the decay of the moments of the topological charge density distribution can be predicted successfully by a simple two–length-scale argument.

Acknowledgements

First of all, I wish to express my gratitude to my advisor, Prof. Paul Goldbart, for shaping my education and for providing continuous and consistent support for my professional growth during the last four years. He was always willing to share his knowledge, help with all the tasks connected to our common research or my research with other collaborators, and take time to provide feedback for my ideas, even the more far-fetched ones. His insistence on professionalism, clear presentations, and precise writing has been of great benefit to me. I am also personally grateful for his concern and understanding during the more difficult periods of my stay in Urbana.

I have greatly benefited from my collaboration and numerous interactions with Prof. Nigel Goldenfeld and Prof. Yoshi Oono. Their deep knowledge of statistical physics and their sharp critical minds have served as invaluable resources for me. Even though the results our collaboration are not directly reflected in this thesis, I would like to thank also Dr. Dmitrii Maslov, for contributing to my education in Urbana, and for providing me with an example of just how efficient a postdoc can be.

A part of the results presented in this thesis originated from my extensive collaboration with Prof. Wojtek Zakrzewski and (more recently) with Dr. Andrew Rutenberg. I wish to thank them for their patience and persistence in the face of dealing with a truly long-distance collaboration, as well as their flexibility and willingness to branch into new and interesting topics. I have learned a number of useful methods in their respective fields from both of them.

I was lucky to be able to attend a number of conferences and summer schools; the lectures and talks of, as well as personal interactions with numerous participants, have

greatly contributed to my education. I wish to mention at least Prof. Alan Bray, from whose papers, talks, and personal comments I derive much of my current knowledge in the field of phase ordering kinetics. In addition to the funding generously provided by my advisor, my travel was often supported by grants from the conference organizers. I wish to thank in particular the Newton Institute for Mathematical Sciences at the University of Cambridge for hospitality and for the funding of my three enjoyable and productive visits there. The work presented in this thesis has been especially strongly influenced by my attendance at the Topological Defects Programme at the Newton Institute in August and September 1994, as well as at the Gordon Conference on Liquid Crystals in June 1995. I would like to thank the organizers of both meetings for making this possible.

I am grateful to Prof. Tim Halpin-Healy from Columbia University for providing me with a serious and at the same time very pleasant research experience in statistical mechanics, which prepared me for an efficient start of my thesis research at the University of Illinois.

I thank Elena Pourmal from the Materials Research Laboratory Center for Computation at the University of Illinois for her highly qualified and efficient help with a number of computing issues, and Jennifer Shannon from the Physics Department for her cheerful coping with my requests for allocation of at times outrageous amounts of computing resources.

I am very grateful to my parents for their continuous encouragement of all my efforts, for their concern and support during all the years I've spent abroad, and for always making me feel at home whenever I was able to return to Prague. I thank the members of the Carey family for their friendship and for kindly providing a "home away from home" for me on the East Coast during the last five years. Last but not least, I thank Saehee Chang for her love and support during more than two years.

The work presented in this thesis was primarily supported by the United States National Science Foundation through grant DMR89-20538 (administered by the Materials Research Laboratory of the University of Illinois at Urbana-Champaign). Ad-

ditional support was provided by a Fellowship from the Department of Physics at the University of Illinois at Urbana-Champaign, as well as a United States National Science Foundation Presidential Young Investigator Award DMR91-57018 (P. M. Goldbart, recipient).

Contents

Chapter 1

Introduction and Overview

The process of phase-ordering kinetics—that is, the approach to equilibrium following a quench between two different thermodynamically stable phases of an ordered system—has been intensively studied since the early 1960s. Phase ordering occurs in many physical situations, and phase-separation processes in systems such as binary alloys, block co-polymers, and binary fluids are of great technological importance. The task of describing this process theoretically, especially its late-time asymptotic regime, has proven to be challenging. This is mainly due to the fact that, subsequent to the quench, the system undergoing phase ordering is far from thermodynamic equilibrium, and the well-developed methods of equilibrium and near-equilibrium statistical physics cannot be used to describe the system fully.

Initially, studies of phase ordering concentrated on systems with scalar order parameters (such as binary alloys). More recently, advances have been made in both experimental and theoretical investigations of phase ordering in systems with continuous symmetries, such as ferromagnets, antiferromagnets, liquid helium, and liquid crystals. In particular, nematic liquid crystals have proven to be a very convenient system for the experimental study of phase ordering. It is interesting to note that recent experimental investigations of phase ordering in liquid crystals and superfluid ^{3}He have to a large degree been motivated by theoretical studies of the mechanism of generation of large-scale inhomogeneities in the early Universe.

The feature of phase ordering that has attracted the most attention is the pres-

ence, in many systems, of a late time asymptotic regime where the correlations of the appropriate order parameter exhibit dynamical scaling, and where a well-defined characteristic length scale, growing as a power law in the time elapsed since the quench, emerges in the system. While a fundamental treatment of the origins of the scaling property remains a theoretical challenge, much progress has been made in investigating a number of specific features of the late-time regime. In the early work on phase ordering for systems with discrete symmetry, it was found to be advantageous to concentrate on the behavior of the domain walls—i.e., singularities of the scalar order parameter—which are generated in the system in large numbers following the quench. Likewise, it has been shown that many features of phase ordering in systems with *continuous* symmetry can be understood in terms of the *topological defects* (such as vortices, disclinations, and hedgehogs) of the corresponding order parameter.

The main purpose of this thesis is to give a detailed discussion of the role of topology—i.e., the homotopy structure of the order parameter space—in phase ordering kinetics. To this end, we study in detail the process of phase ordering in specific physical systems—uniaxial and biaxial nematics in two and three spatial dimensions, and the Heisenberg model in two spatial dimensions—with rich topological properties. The method used is mostly numerical simulations, with measurements concentrating on identifying the nature of and the role played by the topologically stable objects in the system. One of the principal features emerging from this analysis is the explicit connection of *violations of dynamical scaling* in some of the systems studied to the behavior of the topologically nontrivial degrees of freedom.

The thesis is organized as follows. In Chapters 2–4, we introduce the concepts that are used throughout the thesis serve as the motivation for the investigations reported in Chapters 5–7 and Appendix A. In Chapter 2, we briefly review, from the group-theoretical point of view, the description of spontaneous symmetry breaking through the concept of the order-parameter space. In Chapter 3, we present the topological classification of defects and textures in ordered media, and give detailed examples relevant to systems studied in the later chapters. In Chapter 4, we give

a brief introduction to the field of phase ordering kinetics, focusing on the example of spinodal decomposition in binary alloys, and summarize which systems (in spatial dimension two and higher) are currently believed to satisfy or to violate the property of dynamical scaling.

In Chapter 5, we investigate phase-ordering kinetics in nematic films (i.e., in effectively two-dimensional (2D) systems with full $O(3)$ nematic order-parameter symmetry), concentrating in particular on the behavior of topologically stable point defects in such systems. In both the uniaxial and biaxial nematic cases, we observe weak violations of dynamical scaling during the phase-ordering process at even the latest times reached in our simulations, and attribute these to the presence of a logarithmic correction to the asymptotic power-law growth of the average inter-defect separation. While there is only one species of topologically stable defect in the case of the uniaxial nematic, there are four distinct species of topological defects in the biaxial nematic case. The fundamental homotopy group classifying those defects is non-abelian, which leads to non-trivial physical effects. In our simulations of the phase-ordering process, we observe all four species of topological defects that are predicted to occur in the biaxial nematic, and confirm the defect combination laws predicted by the topological classification scheme. We find that at late times after the quench from the isotropic to the biaxial nematic phase, only two species of defects are present at large numbers, and propose a mechanism for the selection of the prevailing defect species based on the defect combination laws and the defect reaction energetics.

In addition to the numerical investigation of the phase ordering process in 2D nematic systems in Chapter [19], we present (in Appendix A) analytical derivations of the singular (power-law) short-distance behavior of the contribution to the structure factor (i.e., the light scattering intensity) for all types of topologically stable defects encountered in 2D and 3D uniaxial and biaxial nematics. Of particular interest is the short distance behavior of the structure factor arising from the ring defect in 3D uniaxial nematics, which consists of two separate power-law regimes having distinct exponents and amplitudes.

In Chapters 6 and 7, we investigate phase ordering in $O(3)$-symmetric vector (i.e. Heisenberg-type) systems in two spatial dimensions, which support topologically stable, but non-singular objects—topological textures (also frequently called skyrmions). In Chapter 6, we implement numerically the Heisenberg-type system as the discretized nonlinear $O(3)$ σ-model with the standard form of the free energy and with purely dissipative dynamics. We concentrate on the role played by topological textures and antitextures during the phase-ordering process. We identify and characterize two distinct mechanisms for the decay of the order-parameter variations—single texture unwinding, and topological charge annihilation. Our results show that while at early times after the quench the annihilation process dominates, the unwinding processes become of comparable importance at later times. We calculate the correlations in the order parameter and in the topological charge density, show that dynamical scaling is strongly violated, and identify multiple characteristic length-scales growing as distinct power-laws in time.

In order to study in detail the origins of the observed multi-scaling behavior, we then study (in Chapter 7) phase ordering in a *modified* nonlinear $O(3)$ σ-model that includes an additional free-energy term (analogous to the Skyrme term familiar in high-energy physics) the effect of which is to stabilize the textures against shrinking and unwinding. We find that this modification influences the multi-scaling properties of the system in a dramatic way. The stabilization of the textures is most clearly reflected in the change of the spectrum of exponents that characterize the decay (with time elapsed since the quench) of the moments of the topological charge density distribution. In the regime where the Skyrme term completely suppresses single-texture unwindings, we are able to predict successfully the form of the spectrum by using a two–length-scale argument.

The research described in this thesis was undertaken under the supervision of my advisor, Paul M. Goldbart. My other collaborators were Nigel Goldenfeld (Chapter 5), Wojtek J. Zakrzewski (Chapters 6 and 7), and Andrew D. Rutenberg (Chapter 7).

Chapter 2

Broken symmetry and the order-parameter space

The bulk of this thesis is concerned with the dynamics of ordered systems following quenches during which the system is abruptly taken from a higher-symmetry phase to a lower-symmetry phase. In this chapter, we briefly review the concept of the order-parameter space as defined through symmetry operations, and give several examples of order parameters spaces relevant to later chapters. Our presentation of material in Chapters 2 and 3 is to a large degree influenced by Mermin's excellent review article [1].

2.1 Group-theoretic definition of the order-parameter space

Phase transitions are commonly accompanied by spontaneous symmetry breaking [2]. By this, we mean that some of the symmetry operations of the state of the system before the phase transition no longer leave the state of the system invariant after the phase transition. A canonical example is that of a Heisenberg ferromagnet, where the magnetic properties of the system are isotropic before the transition to the ferromagnetic state, but a randomly selected preferred direction (given by the magnetization) is acquired after the transition.

It is important to realize, however, that not all of the rotational invariance is lost during the ferromagnetic phase transition. After the magnetization direction is randomly selected, the rotating of the system by any angle about the magnetization axis leaves the state of the system unchanged. The rotational symmetry is therefore

reduced from the full rotational symmetry of the three-dimensional spin space, described by the group $SO(3)$, to the symmetry of rotations about a fixed axis, described by the group $SO(2)$. Other symmetry operations—i.e., the translational symmetry and the space reflection symmetry—are unchanged during the transition.

To identify precisely those symmetry operations that are lost during the phase transition, we have to find the *minimum* set of rotational operations that are needed to transform a system with a given magnetization direction (say along the z-axis) to a system with an arbitrary magnetization direction. In this way, the remaining rotational symmetry $SO(2)$ is "factored out". As the collection of all possible magnetization directions spans the surface of a unit sphere in three dimensions, we may *represent* the minimum set of rotational operations by such a surface. The fundamental mathematical object which is represented geometrically in this way will be called *the order-parameter space.*

The precise definition of the order-parameter space may be given as follows. Let G be the symmetry group of the system before the phase transition, and H be the remaining symmetry group after the phase transition (frequently called the "little group"). According to the discussion in the previous paragraph, if two rotations (or, in general, other symmetry operations) g_1 and g_2 from the group G differ only by a rotation h from the group H—i.e., if $g_2 = hg_1h^{-1}$—then g_1 and g_2 should not be considered as two distinct elements of the order-parameter space. As is known from group theory [4], any element $g \in G$ belongs to exactly one of the *conjugacy classes* of H in G, defined as sets of elements of G related by the transformation hgh^{-1}, where h is any element of H. The set of all conjugacy classes of H in G forms what is called the *coset space* G/H. We therefore arrive at the following formal definition: the order-parameter space R corresponding to a phase transition breaking the symmetry group G into the subgroup H is given by the coset space $R = G/H$. The usefulness of such a group-theoretic description of the order-parameter space will become more apparent in Chapter 3.

In the case of the Heisenberg ferromagnet, the unbroken symmetry group is $G =$

$SO(3)$, the "little group" is $H = SO(2)$, and therefore $R = SO(3)/SO(2)$. As we saw, this space R can be visualized as the surface of a three-dimensional sphere. Note that in this case R does not have a group structure. For example, attempting to define a group operation on R through simple algebraic addition of the azimuthal angles θ and polar angles ϕ of two points on the sphere fails, since the group addition of the North pole with any other point on the sphere (apart from the South pole) is then not uniquely defined: the North pole can be represented by $\theta = 0$ and *any* value of ϕ. In general, for any Lie group G and its subgroup $H \subset G$, the coset space $R = G/H$ is itself a Lie group only if H is a *normal* subgroup of G [3].

A more simple example is provided by the planar ferromagnet, where the magnetization vector is restricted to lie in a fixed plane. In this case we have $G = SO(2)$ [the group of rotations in two dimensions] and $H = \{I\}$ [i.e., the trivial subgroup consisting of only the identity element I], as no rotational symmetry remains after the magnetization is selected. Consequently, the order-parameter space is $R = SO(2)/\{I\} = SO(2)$. Note that in this case R does have a group structure. Geometrically, $R = SO(2)$ can be pictured as a unit circle in the plane in which the magnetization is restricted to lie. The group operation is defined by simply adding the polar angles characterizing two points on the circle. Further examples of order-parameter spaces are given in the following section.

2.2 Nematic order parameters

In this section, we describe the order-parameter spaces of uniaxial and biaxial nematic liquid crystals (which we refer to generically as nematic systems). A nematic system [5] consists of molecules that are anisotropic in shape. The centers of the molecules are randomly diffusing, and the state of the system is always fully translationally invariant, with no lattice order present. In the *isotropic* phase, the distribution of the *orientations* of the molecules is isotropic, and the state of the system possesses the full rotational symmetry in three-dimensional space. In the *nematic phase*, which

occurs for suitable values of temperature and / or pressure, the distribution of the orientations of the molecules is anisotropic, and the rotational symmetry of the isotropic phase is broken. Depending on the shape of the molecules and on the nature of interactions among them, two distinct nematic phases—the uniaxial nematic phase and the biaxial nematic phase—can occur.

We first describe the uniaxial nematic phase. In this phase, the distribution of the orientations of the molecules is anisotropic, but is still symmetric with respect to rotations about a specific axis. The symmetry axis of the orientation distribution defines the so-called *director* $\mathbf{n}$, which can be pictured as a "headless unit vector" ($\mathbf{n}$ and $-\mathbf{n}$ describe an identical physical state). The state of a nematic system in the uniaxial nematic phase is often pictorially described as consisting of molecules with the shape of a rod; the director is then given by the the statistically preferred orientation of the rods. It should be noted, however, that the constituent molecules of (uniaxial) nematic systems typically do not possess the full symmetry of a rod.

What is the order-parameter space characterizing the phase transition from the isotropic phase to the uniaxial nematic case? As in the case of the Heisenberg ferromagnet, discussed in the previous section, the unbroken rotational symmetry group G is the full group of rotations in three dimensions, $G = SO(3)$. The little group H, characterizing the remaining symmetry, is now larger than $SO(2)$: in addition to the rotations around the director $\mathbf{n}$, it includes the inversion operation $\mathbf{n} \to -\mathbf{n}$, or equivalently, 180° rotations about any axis perpendicular to $\mathbf{n}$. The corresponding group is denoted by D_∞ [4]; the order-parameter space for a uniaxial nematic is then given by $R = SO(3)/D_\infty$.

Directors $\mathbf{n}$ with all possible orientations trace the surface of a unit sphere in three dimensions. However, not all points on the sphere are distinct: any two points that are diametrically opposite (i.e., antipodal) correspond to physically equivalent directors, and must therefore be considered identical. The resulting object—a spherical surface with antipodal points identified—is usually denoted as RP_2 (the real projective plane).

We now turn to the description of the *biaxial* nematic order-parameter space. In

the biaxial nematic phase, the state of the system is characterized by a distribution of molecular orientations that does not have any axis or rotation. However, the distribution possesses three mutually perpendicular axes of spatial inversion symmetry (i.e., has the symmetry of the point group D_2). The state of the system can in this case be pictorially described as consisting of molecules with the symmetry of a cuboid (i.e., a rectangular box where all three sides of the box have different lengths); the three symmetry axes of the orientation distribution can then be identified with (i) the statistically preferred orientation $\mathbf{u}$ of the longest sides of the cuboids, (ii) the statistically preferred orientation $\mathbf{b}$ of the second longest sides of the cuboids, and (iii) the direction perpendicular to both $\mathbf{u}$ and $\mathbf{b}$. The directions $\mathbf{u}$ and $\mathbf{b}$ are referred to as the first and the second director of the biaxial nematic phase.

In the biaxial nematic phase, no continuous rotational symmetry remains. The only operations leaving the "cuboid orientational order" invariant are the four elements of the group D_2 (consisting of the three 180° rotations about the three symmetry axes of the cuboid, and of the identity operation). The order-parameter space R corresponding to the phase transition from the isotropic phase to the biaxial nematic phase is therefore given by the coset space $SO(3)/D_2$.

As three independent variables (given for example by the three Euler angles) are needed to describe the orientation of a cuboid, the order-parameter space $R = SO(3)/D_2$ cannot be represented by a two-dimensional surface (in contrast to the uniaxial nematic or Heisenberg ferromagnet case). The geometrical representation of $SO(3)/D_2$ is most naturally obtained from the parametrization of the Lie algebra $SU(2)$ of the Lie group $SO(3)$. Recall that any rotation of a general three-dimensional object can be represented by a unimodular unitary 2×2 matrix [i.e., an element of $SU(2)$]. Any unimodular unitary 2×2 matrix u can be expressed as $u = a_0 I + a_1 i\sigma_x + a_2 i\sigma_y + a_3 i\sigma_z$, where $I = \left(\begin{smallmatrix} 1 & 0 \\ 0 & 1 \end{smallmatrix}\right)$ is the unit matrix, $\sigma_x = \left(\begin{smallmatrix} 0 & 1 \\ 1 & 0 \end{smallmatrix}\right)$, $\sigma_y = \left(\begin{smallmatrix} 0 & -i \\ i & 0 \end{smallmatrix}\right)$, and $\sigma_z = \left(\begin{smallmatrix} 1 & 0 \\ 0 & -1 \end{smallmatrix}\right)$ are the Pauli matrices, and the coefficients a_i satisfy the condition $a_0^2 + a_1^2 + a_2^2 + a_3^2 = 1$. Pairs of matrices u differing only by an overall sign change—i.e., matrices with coefficients $[a_0, a_1, a_2, a_3]$ and $[-a_0, -a_1, -a_2, -a_3]$ in the

parametrization given above—represent the *same* three-dimensional rotation. The group $SO(3)$ can therefore be geometrically represented as the (three-dimensional) surface of a unit sphere in the four-dimensional space of parameters a_0, a_1, a_2, a_3, with antipodal points on the sphere identified (note the similarity in this respect to the two-dimensional surface RP_2). To represent the coset space $SO(3)/D_2$, we need to take into account that rotations by 180° about the three Cartesian coordinate axes x, y and z in the rotation space leave the cuboid-shaped object unchanged. The generators of such rotations are given directly by the three matrices $i\sigma_x$, $i\sigma_y$, and $i\sigma_z$; we therefore conclude that the four points $[1,0,0,0]$ (no rotation), $[0,1,0,0]$ (180° rotation about the x-axis), $[0,0,1,0]$ (180° rotation about the y-axis), and $[0,0,0,1]$ (180° rotation about the z-axis) on the spherical surface $a_0^2+a_1^2+a_2^2+a_3^2=1$ are equivalent to each other. Combined with the invariance under the simultaneous change of sign of all the parameters a_i, this means that each point on the three-dimensional spherical surface representing the space $SO(3)/D_2$ is equivalent to seven other points, equidistantly spaced from each other on the sphere. While this geometrical representation of the biaxial nematic order parameter space may seem complicated, it is useful to keep it in mind while using the homotopy theory formalism, described in the next chapter.

References

[1] N. D. Mermin, Rev. Mod. Phys. **51**, 591 (1979).

[2] Examples of phase transitions that are *not* associated with any symmetry breaking include the liquid-gas phase transition and the phase separation transition in binary mixtures. In these systems, the order parameter needs to be defined by means other than those described in this chapter.

[3] A subgroup H of a group G is called a *normal* subgroup if for all elements $h \in H$, the conjugacy class $\{ghg^{-1}; g \in G\}$ is a subset of H.

[4] See, e.g., B. G. Wybourne, *Classical Groups for Physicists* (New York, John Willey, 1974).

[5] P.-G. de Gennes and J. Prost, *The Physics of Liquid Crystals* (Oxford, Clarendon, 1993).

Chapter 3

Topological classification of defects and textures in ordered media

In this chapter, we present the basics of the topological classification of defects and (topological) textures in ordered systems, and discuss in more detail some mathematical results relevant to the later parts of this thesis. Our presentation is based mostly on Refs. [1] and [2]. The concepts described originated in the work of Volovik and Mineev [3] and of Toulouse, Kléman, and Michel [4]. In order to motivate the mathematical formalism used in the remainder of the chapter, we first discuss (in Sec. 3.1) the well-known examples of topological defects in planar and Heisenberg ferromagnets in two and three spatial dimensions. In Section 3.2, we introduce the concept of the fundamental homotopy group of the order parameter space, and discuss its use in the classification of topological defects. The specific case of the fundamental group of the biaxial nematic order parameter space and, in particular, the physical implications of its non-abelian character, are discussed in Sec. 3.3. In Sec. 3.4, we discuss the meaning of higher (specifically, the second and the third) homotopy groups of the order parameter space, and introduce the concept of topologically stable, but non-singular objects—topological textures.

3.1 Topological defects in planar and Heisenberg ferromagnets

Consider a continuum classical description of a ferromagnetic material, the magnetic ordering of which is locally described by the magnetization $\mathbf{m}(\mathbf{r})$. Here $\mathbf{m}$ is a two-

component vector for a planar ferromagnet, and a three-component vector for the Heisenberg ferromagnet. Although the magnitude $|\mathbf{m}(\mathbf{r})|$ of the vector $\mathbf{m}$ can vary throughout the system, if $|\mathbf{m}(\mathbf{r})| > 0$, we may always define the direction of the magnetization, which is given by the unit vector $\hat{\mathbf{m}}(\mathbf{r}) \equiv \mathbf{m}(\mathbf{r})/|\mathbf{m}(\mathbf{r})|$. The collection of possible directions of $\hat{\mathbf{m}}$ are elements of the ferromagnetic order parameter space, defined in the previous chapter. In general, the spatial variation of $\hat{\mathbf{m}}(\mathbf{r})$ in a three-dimensional system can be *singular* (i.e., the gradient of $\hat{\mathbf{m}}(\mathbf{r})$ can be divergent) on isolated points, lines or surfaces; such singular regions will be called point, linear, or surface *defects*. Not all defects, however, are *topological* defects. The basic question that needs to be answered to decide if a given singular defect configuration is topologically stable is the following: can the defect be removed from the system by making local changes in the order parameter field, without introducing additional singularities during the attempt to remove the defect? If the answer is positive, the defect may be removed from the system by overcoming at most a finite energy barrier associated with the continuous distortion of the magnetization gradients during the removal process in a spatially finite region. If the answer is negative, however, the defect may disappear from the system only by reacting with other defects or diffusing away through the system boundary, and is then called a *topologically stable defect*.

A more precise formulation of the basic question is as follows. Consider for simplicity the case of a point defect in a two-dimensional system. Surround the defect by a circle such that only the defect in question, and no other defects, lies within the circle. Is it possible to remove the singularity in the circle by *continuous* deformations [5] of the order parameter localized *within* the circle? (Such deformations will be termed "local surgery").

We first give an example of a defect that *is* removable by local surgery. Consider the configuration of a two-dimensional Heisenberg ferromagnet pictured in Fig. 3.1a, in which the magnetization rotates by 360° around the singular point. Keeping the configuration outside of the indicated circle fixed, we can gradually tilt the magnetization vectors out of the plane, starting from the center, until we arrive to the

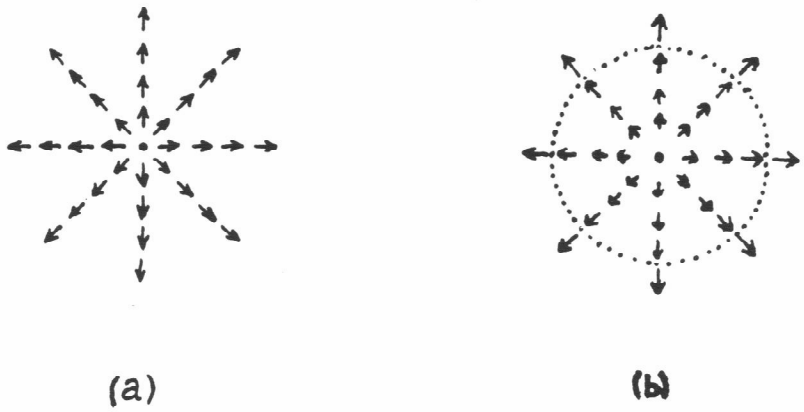

Figure 3.1: (a) The 360° defect configuration in the 2D Heisenberg ferromagnet. (b) Removal of the 360° defect through local surgery (see the main text).

non-singular configuration in Fig. (3.1b). We therefore successfully removed the vortex-like configuration in a Heisenberg ferromagnet by continuous local surgery. (The process described above is called "escape into the third dimension").

Such a removal is not possible for the same magnetization configuration in a *planar* ferromagnet, where the magnetization vector cannot be tilted out of the plane. Furthermore, it is easy to see that it is not possible to remove the defect by any in-plane distortion of the magnetization configuration: Consider a local surgery region delimited by a circle C of radius r surrounding the central singular point. The winding number $N \equiv (2\pi)^{-1} \int_C d\mathbf{l} \cdot \nabla\phi(\hat{\mathbf{m}})$ (where $\phi(\hat{\mathbf{m}})$ is the polar angle of $\hat{\mathbf{m}}$ in the magnetization plane) around the circle C by definition stays equal to 1 during the local surgery procedure. If the singularity at the central point is successfully removed, there must exist a circle (of radius $s < r$) surrounding it for which the circulation N is zero. Since N in a planar ferromagnet can take only integer values, we would then have a singular jump in the circulation N somewhere in between the circles of radii s and r; this is possible only if singularities of $\hat{\mathbf{m}}(\mathbf{r})$ exist outside of the central

point, which is contrary to the definition of local surgery. The vortex configuration Fig. 3.1a in a planar ferromagnet therefore constitutes a topologically stable defect. Likewise, it is evident that any configuration of a planar ferromagnet in which the magnetization vector rotates around a central singular point by an integer multiple of 360° is topologically stable [7], whereas the same configuration in a 2D Heisenberg ferromagnet is always topologically unstable.

How do the considerations presented above change for a (spatially) three-dimensional system? For a planar ferromagnet in 3D, we can extend the configuration pictured in Fig. 3.1a uniformly in the direction perpendicular to the plane of the picture, and obtain a vortex line. The topological stability of a vortex line follows from arguments similar to those given above for the point vortex in 2D; instead of a loop surrounding the point vortex, we may now use any loop that wraps around the vortex line. In a Heisenberg ferromagnet in 3D, the vortex line is again topologically unstable. There does, however, exist a topologically stable *point* defect in this system: the monopole configuration pictured in Fig. 3.2 is easily shown to be topologically stable by an argument similar to that given in the previous paragraph for the vortex in a planar ferromagnet in 2D. The only difference is that instead of the circulation of $\hat{\mathbf{m}}(\mathbf{r})$ around a circle surrounding the vortex, we now have to consider the winding number $M \equiv (8\pi)^{-1} \int_S dS_k \, \epsilon_{ijk} \, \hat{\mathbf{m}} \cdot (\partial_i \hat{\mathbf{m}} \times \partial_j \hat{\mathbf{m}})$ on a closed *surface* (having the topology of a sphere) surrounding the monopole in the 3D space. The integer M counts how many times the configuration of $\hat{\mathbf{m}}(\mathbf{r})$ on the (real space) surface S covers the (spherical) order-parameter space introduced in the previous chapter.

We have demonstrated the existence of the following topological defects: (a) point defects in the planar ferromagnet in 2D; (b) line defects in the planar ferromagnet in 3D; (c) point defects in the Heisenberg ferromagnet in 3D. In Secs. 3.2 and 3.4 of the present chapter we shall see how the existence of these topological defects (and the absence of other types of topological defects) in planar and Heisenberg ferromagnets naturally follows from the homotopy structure of the corresponding order parameter spaces.

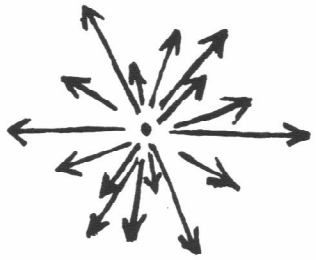

Figure 3.2: A monopole defect configuration in the 3D Heisenberg ferromagnet.

3.2 The fundamental homotopy group

We now discuss the concept of the fundamental (or first) homotopy group $\Pi_1(R)$ of a given order parameter space R. In order to motivate the definition of $\Pi_1(R)$, let us return to the example of the topologically unstable point defect configuration, shown in Fig. 3.1a, in the Heisenberg ferromagnet in 2D. The values of magnetization directions $\hat{\mathbf{m}}(\mathbf{r})$ on the circle shown in Fig. 3.1a (or in general, on any contour surrounding the point defect), traversed in the counter-clockwise direction, trace out an *oriented loop* in the order parameter space (given by the surface S_2 of a unit sphere in three dimensions) of the Heisenberg ferromagnet—see Fig. 3.3. The process of local surgery that converts Fig. 3.1a to Fig. 3.1b can now be pictured in the order parameter space as the gradual contraction of the loop in Fig. 3.3 to the north pole. The closer the contour corresponding to the loop in Fig. 3.1a is to the singular defect, the farther to the north the loop has to be contracted to achieve the configuration in Fig. 3.1b. For the defect in Fig. 3.1a to be removable, it must be possible to contract the loop all the way to a point (the north pole in the order parameter space). It is therefore seen that the possibility of removing the defect in Fig. 3.1a by local surgery is associated

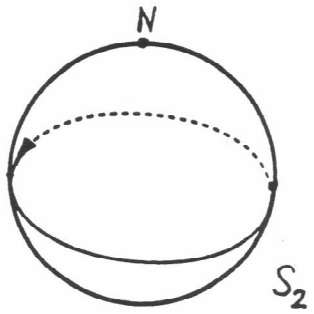

Figure 3.3: The contractible loop in the order parameter space S_2 corresponding to the topologically unstable configuration shown in Fig. 3.1a.

with the fact that the image of any (real space) contour surrounding the defect is a *contractible loop* in order parameter space.

Conversely, topologically stable defects correspond to *incontractible loops* in order parameter space. As an example, consider the vortex configuration Fig. 3.1a in a *planar* ferromagnet in 2D. The order parameter space of a planar ferromagnet, as we saw in Sec. 2.1, is the unit circle. The magnetization configuration on any contour surrounding the vortex winds around the order parameter circle S_1 exactly once; i.e., it maps onto an incontractible loop in S_1. Likewise, contours around vortex configurations with higher winding numbers N map into incontractible loops that wrap around S_1 N times.

The third example that we shall consider is that of a uniaxial nematic. As was shown in Sec. 2.2, the order parameter space is the projective plane RP_2. It is readily seen that the singular director configuration analogous to the magnetic vortex in Fig. 3.1a, in which the director rotates around the central point by 360°, is topologically unstable—the singularity can be removed by a local surgery process analogous

to the one described above for the Heisenberg ferromagnet. In contrast, the configuration pictured in Fig. 3.4a, in which the director rotates by only 180°, *is* topologically stable: a contour surrounding the central singularity maps onto the loop in RP_2 shown in Fig. 3.5a; this loop is incontractible as the antipodal points P and P' are identified. We therefore find that topological point defects exist in a uniaxial nematic in 2D. The failure of an attempt to remove the defect in Fig. 3.4a by local surgery using rotations of the director out of the plane can be seen explicitly in Fig. 3.4b. Specifically, let us start rotating the directors located just above the dotted line in Fig. 3.4b out of the page in such a way that the indicated "nail heads" of the directors point above the surface of the page, and continue this rotation moving clockwise on each contour surrounding the central singularity. It is evident that in this way, we arrive at a discontinuity in the order-parameter configuration everywhere along the dotted line, as the directors on the opposite sides of the line have to rotate in opposite senses. In general, any attempt to rotate all the directors in Fig. 3.4a out of the page generates a line singularity extending from the central point to infinity.

The example of a uniaxial nematic is also useful to clarify the meaning of continuous *deformations* of loops in order parameter space. Instead of the configuration in Fig. 3.4a, in which the director rotates around the central point uniformly and stays in a fixed plane, we may consider any continuous deformation [5] of such a configuration; any contour surrounding the singularity is then mapped again into a closed curve in the order parameter space RP_2, which is different from that shown in Fig. 3.5a, but can be continuously deformed into it in the order parameter space. Of special interest is the configuration shown in Fig. 3.6, in which the director rotates around the central point again by 180°, but in the direction opposite to that in Fig. 3.4a. The corresponding loop in the order parameter space is shown in Fig. 3.5b. Notice that the loop in Fig. 3.5b can be continuously deformed into the loop in Fig. 3.5a by sweeping the loop through the north pole while keeping the loop end-points fixed. The inverse image of this process in real space gives the prescription for a local surgery procedure converting the configuration in Fig. 3.6 into the configuration in Fig. 3.4a.

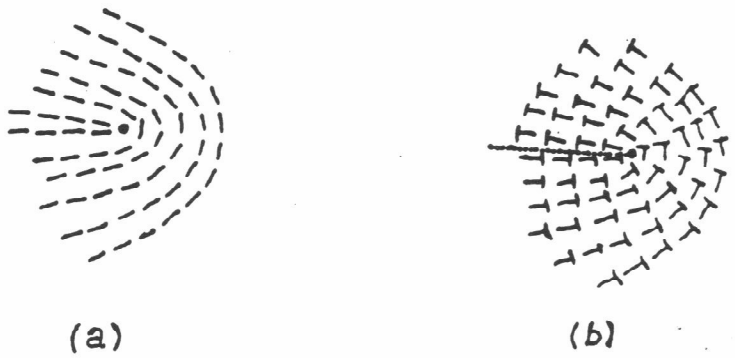

Figure 3.4: (a) The 180° defect configuration in a uniaxial nematic. (b) An attempt to remove the 180° defect by continuously rotating the "nail heads" given to the directors out of the plane fails: the directors on opposite sides of the dotted line would have to rotate in opposite senses, generating a line singularity. (For ease of visualization, the directors are given "nail heads" in the figure; however, the ends of each director should still be considered physically indistinguishable.)

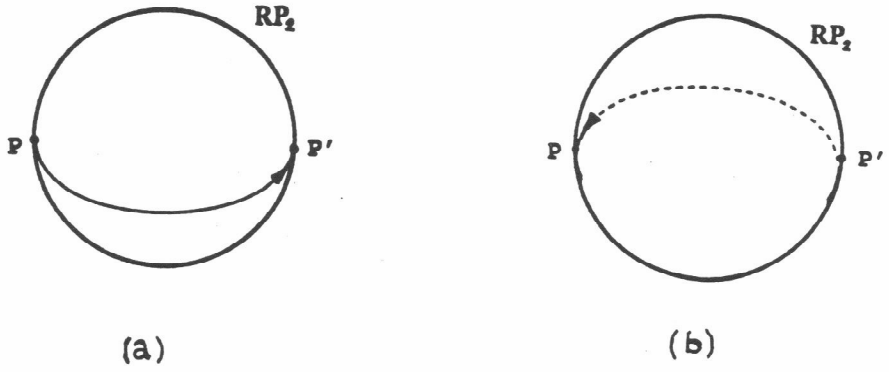

Figure 3.5: Incontractible loops in order parameter space RP_2 corresponding to the defect configurations in (a) Fig. 3.4a and (b) Fig. 3.6. Note that antipodal points on the sphere (for example, the points P and P') should be considered identical.

Figure 3.6: The $-180°$ defect configuration in the uniaxial nematic, topologically equivalent to the configuration in Fig. 3.4a.

The two configurations are therefore topologically equivalent, despite the opposite signs of the winding angles $180°$ and $-180°$ of the director. Also, it is evident that any loop corresponding to a director configuration rotating around the central point by an odd multiple of $\pm 180°$ can be continuously deformed into the loop shown in Fig. 3.5a, corresponding to the $180°$ defect, and that any loop corresponding to the winding by an even multiple of $\pm 180°$ can be shrunk to a point, corresponding to a homogeneous configuration. There is, therefore, only *one type* of topological defect in a uniaxial nematic in 2D, and it can be represented by the configuration in Fig. 3.4a. This is in contrast to the case of the planar ferromagnet in 2D, for which we saw that a whole family of topologically distinct point defect configurations, parametrized by the integer winding number N, exists; this is a consequence of the fact that oriented loops winding around the circle S_1 a different number of times cannot be continuously deformed into each other.

The discussion given above motivates us to define the *fundamental homotopy group* $\Pi_1(R)$ of the order parameter space R as the space of all classes of mutually deformable

loops in R (called the homotopy classes of R). The different types of topological point defects in a two-dimensional system with order parameter space R then correspond to the different homotopy classes [8].

To be more precise, consider an oriented loop in R that passes through a given point $x \in R$. The loop may be parametrized by a continuous map $f(s) : [0,1] \to R$ with $f(0) = f(1) = x$. Consider now another loop $g : [0,1] \to R$ passing through x. We say that the loops f and g are *homotopic* at x if there exists a family of loops $\{h_t(s) : [0,1] \to R, t \in [0,1]\}$, with every loop h_t passing through x, such that h_t is the loop (i.e,. map) f, h_1 is the loop g, and derivatives of $h_t(s)$ of all orders in t exist for all $t \in [0,1]$ and all $s \in [0,1]$. All loops passing through x that are mutually homotopic form a *homotopy class based at* x.

The collection of all homotopy classes based at x forms the *fundamental homotopy group of* R *at* x, $\Pi_1(R,x)$. Here the group operation (product) of two classes F and G from $\Pi_1(R,x)$ is defined as the class containing the loop obtained by combining any two loops $f \in F$ and $g \in G$ (here by combining we simply mean traversing the loop f first, returning to the point x, and then traversing the loop g; the resulting loop will be denoted by $f \circ g$). It can be readily shown (see, e.g., Ref. [1]) that with such a definition of the group operation, the set of classes $\Pi_1(R,x)$ indeed satisfies all the axioms of a group. The identity element is the class of contractible loops passing through x, which includes the trivial map $f(s) = x$ (i.e., the loop consisting solely of the point x). The inverse element F^{-1} for any class $F \in \Pi_1(R,x)$ is given by the collection of all loops from F traversed in the opposite direction (i.e., if the loop f belongs to F, the loop $\bar{f}$ parametrized as $\bar{f}(s) = f(1-s)$ belongs to F^{-1}).

From now on, we will restrict ourselves to order parameter spaces R that are *connected* (meaning that for any two elements $x, y \in R$, there exists a continuous map $c(s) : [0,1] \to R$ such that $c(0) = x$ and $c(1) = y$). All order parameter spaces that we have considered thus far are connected; the topological classification of defects for disconnected order parameter spaces R may be obtained by considering each connected component of R separately. It is readily seen that for any connected

space R, the two homotopy groups $\Pi_1(R,x)$ and $\Pi_1(R,y)$ based at any two points x and y in R are isomorphic: any loop f based at x can be converted to a loop g based at y by combining f with a loop passing through the points x and y (such a loop exists by the assumption of connectivity of R), and vice versa; this induces a one-to-one correspondence of the homotopy classes based at x and y that preserves the class combination laws. From now on, we shall therefore simply speak about the *fundamental homotopy group* $\Pi_1(R)$ *of* R, without reference to a particular base point.

We now give examples of fundamental homotopy groups for some simple order parameter spaces. A trivial example is provided by the Heisenberg ferromagnet, for which the order parameter space R is the surface S_2 of a unit sphere. Clearly, any loop starting at the north pole can be continuously shrunk (i.e., is homotopic to) the north pole point; that is, $\Pi_1(S_2)$ is the trivial group consisting solely of the unit element. More interesting is the example of the uniaxial nematic: any loop starting *and* terminating at the point P in the picture of the projective plane RP_2 in Fig. 3.5 can be shrunk to the point P; however, any loop starting at P and terminating at the antipodal point P' (such as the loop drawn in Fig. 3.5a) cannot be shrunk to a point. Therefore $\Pi_1(RP_2)$ is the two-element group Z_2. Our last example is that of the planar ferromagnet: here the order parameter space R is the unit circle S_1, and all loops in R divide into mutually undeformable classes characterized by how many times (and in what direction) the loop winds around the circle. Therefore $\Pi_1(S_1)$ is isomorphic to the group of integers Z.

What is the precise correspondence of the elements of $\Pi_1(R)$ and the topologically distinct classes of point defects in a two-dimensional system with order parameter space R? Earlier we saw that a point defect configuration may be removed by local surgery (i.e., is not topologically stable) if and only if the loop in R obtained as the image of any contour surrounding the defect is contractible to a point. Therefore the identity element of $\Pi_1(R)$ corresponds to topologically trivial configurations, and all other elements of $\Pi_1(R)$ correspond to topologically stable defects. Do all non-trivial

elements of $\Pi_1(R)$ correspond to *distinct* topological defect classes, i.e. to defects that cannot be deformed into each other by local surgery? To answer this question, we need to discuss the concept of *free homotopy*. Earlier, we saw that the process of local surgery on a given defect configuration can be viewed in the order-parameter space R as consisting of continuous deformations of loops in R that correspond to contours surrounding the defect in real space. These deformations do not have to keep any point of the loop in R fixed. Our definition of $\Pi_1(R)$, however, was founded on the relation of homotopy at x of two loops sharing a common starting point x ("based homotopy"). Such a restriction was necessary in order to obtain an object with group structure (as it is not clear how to combine two loops that do not share any common points). To relate directly to the physical process of local surgery, however, we now define two loops f and g in R to be *freely homotopic* if there is a family of loops h_t, continuous in t, such that $h_0 = f$ and $h_1 = g$; that is, we drop the requirement (defining *based* homotopy) that the family of loops h_t share a common point.

Any two loops sharing a common point x and corresponding to the same element of $\Pi_1(R)$ (meaning that they are homotopic at x) are, of course, also freely homotopic. In certain order parameter spaces R it is, furthermore, possible for two loops to be freely homotopic to each other, even if they correspond to *different* elements of $\Pi_1(R)$. A convenient, if somewhat artificial, example is that of the order parameter space R consisting of a plane with two holes (Fig. 3.7a). The loops f and g in Fig. 3.7a clearly cannot be deformed into each other while keeping their common point x fixed; they therefore correspond to different elements of $\Pi_1(R, x)$. Once we relax the requirement that the loops remain tied to x during the deformation process, however, we may for example start shrinking the loop f up from x, pass its bottom end above the lower hole in Fig. 3.7a, and then bring it down on the right-hand side back to the point x, thus continuously deforming f into the loop g; the two loops are therefore freely homotopic. We now note that the conversion of f to g can also be achieved by combining the loop f with the loop c shown in Fig. 3.7a and its inverse: by traversing first c, then f, and then c^{-1}, we obtain a loop $c \circ f \circ c^{-1}$ which is homotopic at x to

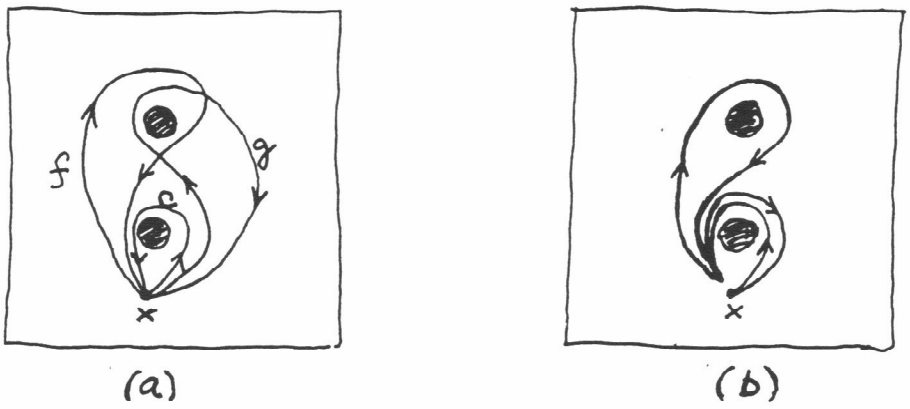

Figure 3.7: Free and based homotopy of loops in the order parameter space consisting of a plane with two holes. (a) The two loops f and g are not homotopic at x. (b) The loop $c \circ f \circ c^{-1}$ may be used to show that f and g are *freely* homotopic.

the loop g (see Fig. 3.7b). In terms of the based homotopy classes $F, G, C \in \Pi_1(R, x)$, corresponding to the loops f, g and c, this is expressed by the identity

$$CFC^{-1} = G \tag{3.1}$$

[where multiplication indicates the group operation in $\Pi_1(R)$].

The construction just given (and its analog for arbitrary order parameter spaces R) has an important implication: if F and C are two elements of $\Pi_1(R)$, the element CFC^{-1} corresponds to loops that are freely homotopic to loops from F; therefore, F and CFC^{-1} always represent *topologically equivalent* defects. For any group Π, the set of elements $\{CFC^{-1}; C \in \Pi\}$ is called the *conjugacy class* of the element F. It can be shown that each element of Π falls into exactly one conjugacy class in Π (note, however, that the set of all conjugacy classes of a group Π does not necessarily itself form a group). Our arguments lead us to conclude that topologically distinct classes of defects in a system with order parameter space R are classified by the *conjugacy classes of the fundamental homotopy group* $\Pi_1(R)$.

It is straightforward to see that for any *abelian* (i.e., commutative) group Π, each of the conjugacy classes contains just one element, and the set of conjugacy classes is therefore identical to the group Π itself (a consequence of the property $CFC^{-1} = CC^{-1}F = F$ for all $C, F \in \Pi$). The examples of fundamental homotopy groups that we gave earlier—namely, $\Pi_1(S_2) = I$, $\Pi_1(RP_2) = Z_2$, and $\Pi_1(S_1) = Z$—are all abelian. Consequently, the topologically distinct defect classes in the corresponding physical systems are classified simply by the elements of these groups. These results are in agreement with the discussion of topological defects for planar and Heisenberg ferromagnets in Sec. 3.1, and for uniaxial nematics earlier in this section.

If, however, the fundamental homotopy group $\Pi_1(R)$ is *non-abelian*, some of the distinct elements of $\Pi_1(R)$ correspond to topological defects that can be deformed into each other by local surgery. The physical consequences of such a situation will be examined in the next section in the context of defects in biaxial nematics.

We are now in a position to discuss the physical meaning of the group operation in $\Pi_1(R)$ in the context of the topological classification of defects. Consider two point defects, A and B, located next to each other in a 2D system; we may ask what is the result of the *combination* of the two defects—i.e., what type of defect results if the two singularities are brought together by a continuous process? This question can be answered by examining the loop h in R corresponding to any contour s_h surrounding both A and B in real space [see Fig. 3.8], and finding the conjugacy class H that represents s_h in the group $\Pi_1(R)$. The contour s_h can be continuously deformed into the contour s_g shown in Fig. 3.8, consisting of the combination of the contour s_a surrounding the defect A with the contour s_b surrounding the defect B. For the loops h, a, and b in the order parameter space R (traced by the order-parameter configurations on the contours s_h, s_a and s_b, respectively), this implies that the loop h is freely homotopic to the loop $a \circ b$. Therefore, the combination of defects A and B is classified by the conjugacy class of $\Pi_1(R)$ containing the element AB, where A and B are any elements of $\Pi_1(R)$ representing loops freely homotopic to a and b, respectively. In essence, the result of combining two defects is given simply by

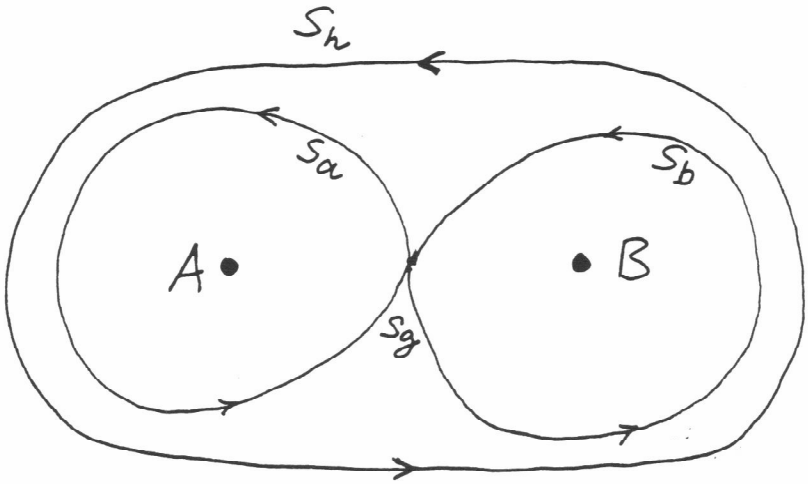

Figure 3.8: Combination of two topological defects. The contours s_a and s_b surround the defects A and B, respectively. The contour s_h surrounding both defects can be continuously deformed into the contour $s_g = s_a \circ s_b$.

the group operation in $\Pi_1(R)$, keeping in mind that the topological defect classes correspond to conjugacy classes, rather than elements, of $\Pi_1(R)$.

To conclude this section, let us briefly summarize its main points. For an arbitrary order parameter space R, the fundamental homotopy group $\Pi_1(R, x)$ of R at x is defined as the set of based homotopy classes of all loops in R passing through x, with the group operation induced by loop combination. If R is a connected topological space, the groups $\Pi_1(R, x)$ are isomorphic for all $x \in R$. Classes of *freely* homotopic loops in R correspond to topologically distinct point defects in a two-dimensional system with order parameter space R, and all possible deformations of them by local surgery. If $\Pi_1(R)$ is an abelian group, the freely homotopic loop classes are given simply by the elements of $\Pi_1(R)$. If $\Pi_1(R)$ is non-abelian, in general a number of elements of $\Pi_1(R)$ corresponds to the same free homotopy class of R, and topologically distinct point defects are classified by the *conjugacy classes* of $\Pi_1(R)$. The defect combination laws are determined by the group operation in $\Pi_1(R)$ and the corresponding multiplication table of the conjugacy classes in $\Pi_1(R)$.

3.3 Topological defects in biaxial nematics

3.3.1 Fundamental homotopy group of the biaxial nematic order parameter space

Recall that (see Sec. 2) the orientational order of molecules in a biaxial nematic can be characterized by two mutually perpendicular directors $\mathbf{u}$ and $\mathbf{b}$; here $\pm\mathbf{u}$ $\pm\mathbf{b}$, and $\pm\mathbf{u} \times \mathbf{b}$ are the three symmetry axes of the cuboid distribution of molecular orientations. In the *uniaxial* nematic case, where the orientational order is described by only one director $\mathbf{u}$, we saw in the previous section that there is only one class of topologically non-trivial point defect in 2D, which can be represented by the configuration in which $\mathbf{u}$ rotates around a central point by 180°. The more complicated character of the order parameter space in the *biaxial* nematic results in a richer structure of topological defects. There are now three topologically distinct classes of 180° defects: in defects from the C_x class, the principal director $\mathbf{u}$ rotates by ±180° and the second director $\mathbf{b}$ does not rotate; in C_y defects, $\mathbf{u}$ does not rotate and $\mathbf{b}$ rotates by ±180°; and in C_z defects, both $\mathbf{u}$ and $\mathbf{b}$ rotate by ±180° (see Figs. 3.9a-c). In addition, there is a 4th non-trivial defect class, $\overline{C}_0$, where either $\mathbf{u}$ or $\mathbf{b}$ (or both) rotate by 360° (Fig. 3.9d). In contrast to the uniaxial case, the 360° defect cannot be removed by local surgery—an attempt to remove the singularity in the $\mathbf{u}$ director in Fig. 3.9d by rotating $\mathbf{u}$ out of the plane merely converts the configuration in Fig. 3.9d to another singular configuration, where the $\mathbf{b}$ director rotates by 360°. (This is also the reason why there is only one topological class of 360° defects, as opposed to three 180° classes.)

To prove that the classification of point defects in the two-dimensional biaxial nematic given in the previous paragraph is complete, and to deduce the defect combination laws, we need to calculate the fundamental homotopy group $\Pi_1(R)$ of the biaxial nematic order parameter space R. In Sec. 2.2, we saw that R is given by the (three-dimensional) surface of a unit sphere in four dimensions, with each point on the sphere identified with seven other points related to the first point by ±90° and 180°

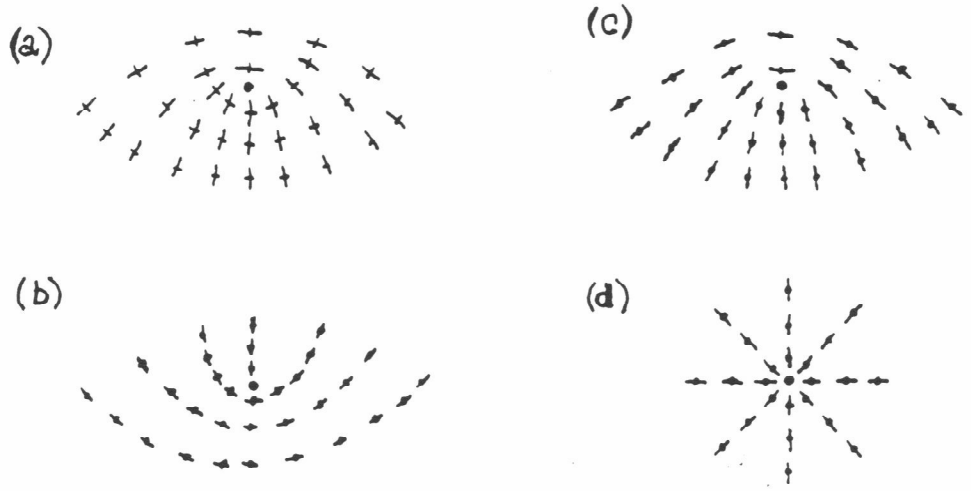

Figure 3.9: The 4 species of topological defects in biaxial nematics. The directors **u** and **b** are depicted as long and short rods, respectively. (a) The C_z defect, in which both **u** and **b** rotate by 180°; (b) The C_y defect, in which **b** rotates by 180°; (c) the C_x defect, in which **u** rotates by 180°; (d) an example of the $\overline{C}_0$ defect, in which **u** rotates by 360°.

rotations abound the coordinate axes of the four-dimensional space. In the uniaxial nematic case, for which R is the projective plane RP_2, we were able to obtain $\Pi_1(R)$ by simple inspection of the possible types of loops in R. For the biaxial order parameter space R, such an approach is less straightforward: we need to consider $\binom{8}{2} = 28$ incontractible loops connecting all pairs of the eight equivalent points, many of which turn out to be identical. Instead, we formulate below a general theorem that can be used to calculate $\Pi_1(R)$ for any order parameter space R.

In Chap. 2, we saw that the order parameter space R can in general be represented as the coset space G/H, where G is the symmetry group of the system before the phase transition, and H is the residual symmetry group after the phase transition. We are interested in systems with continuous symmetry, in which case the group G is a Lie group. Recall that G is called *connected* if for any two elements $x, y \in G$, there exists a continuous path connecting them (i.e., if there exists a continuous map

$c(s) : [0,1] \to G$ such that $c(0) = x$ and $c(1) = y$). A Lie group G is called *simply connected* if any loop in G can be continuously shrunk to a point (i.e., if the first homotopy group of G is trivial). The following theorem holds:

Theorem: Let G be a connected, simply connected Lie group. Let H be a subgroup of G, and let H_0 be the connected component of H (i.e., H_0 consists of elements of H that are connected to the identity element by continuous paths lying in H). Then the fundamental group $\Pi_1(G/H)$ of the coset space G/H is isomorphic to the coset space H/H_0.

The theorem given above can be proved by constructing an explicit relation between loops in the coset space G/H and continuous paths in G that connect elements in H to the identity element. A detailed description of the proof is given e.g. in Ref. [1].

In Sec. 2.2, we showed that the biaxial nematic order parameter space R is given by the coset space $SO(3)/D_2$, where D_2 is the 4-element symmetry group of a rectangular box. We are not able to directly use the theorem from the previous paragraph to calculate $\Pi_1(R)$, as the group $SO(3)$ is not simply connected [9]. We may, however, proceed as follows: We replace the group $SO(3)$ by the special unitary group $SU(2)$, which contains two copies of $SO(3)$ (more precisely, there exists a 2 to 1 homomorphism of $SU(2)$ onto $SO(3)$, given by exponentiating all pairs of matrices from $SU(2)$ related by an overall sign change). At the same time, we replace the little group D_2 by its inverse image ("lift") $\overline{D}_2$ in $SU(2)$ under this homomorphism. In this way, we have replaced the coset space $SO(3)/D_2$ by the equivalent coset space $SU(2)/\overline{D}_2$; as $SU(2)$ is simply connected, we can now use the theorem from the previous paragraph. As we already discussed in Sec. 2.2, the non-trivial symmetry operations of the group D_2—namely, the 180° rotations about the x, y, and z axes—are represented in $SU(2)$ by the Pauli matrices (with an additional factor of i) $i\sigma_x$, $i\sigma_y$, and $i\sigma_z$, respectively, and by their negatives. The fourth element of D_2—the identity operation—is represented in $SU(2)$ by the unit matrix I, as well as by $-I$. Therefore, $\overline{D}_2$ is given by

the eight-element group Q

$$Q = \{I, -I, i\sigma_x, -i\sigma_x, i\sigma_y, -i\sigma_y, i\sigma_z, -i\sigma_z\}\,, \tag{3.2}$$

which is isomorphic to the group of *quaternions*. Since Q is a discrete group, its connected component Q_0 is given simply by $\{I\}$, and the coset space Q/Q_0 is the group Q itself. We thus obtain the result $\Pi_1(SO(3)/D_2) = Q$.

Note that the quaternion group Q is non-abelian: for example, $(i\sigma_x)(i\sigma_y) \neq (i\sigma_y)(i\sigma_x)$. To complete the classification of topological defects described by $\Pi_1(SO(3)/D_2)$, we therefore must find the conjugacy classes of Q. It is straightforward to show that Q has *five* conjugacy classes, given by $\{I\}$, $\{-I\}$, $\{i\sigma_x, -i\sigma_x\}$, $\{i\sigma_y, -i\sigma_y\}$, and $\{i\sigma_z, -i\sigma_z\}$. (For example, the identity $(i\sigma_x)(i\sigma_y)(i\sigma_x)^{-1} = -(i\sigma_y)$ demonstrates that $(i\sigma_y)$ and $-(i\sigma_y)$ belong to the same conjugacy class.) We therefore conclude that there are four non-trivial topological defect classes in the biaxial nematic. The conjugacy classes $\{i\sigma_x, -i\sigma_x\}$, $\{i\sigma_y, -i\sigma_y\}$, and $\{i\sigma_z, -i\sigma_z\}$ correspond to the defect types shown in Figs. 3.9a-c, where the directors rotate by 180°; the class $\{-I\}$ corresponds to the 360° defect in Fig. 3.9d; the class $\{I\}$ corresponds to topologically trivial order parameter configurations.

3.3.2 Path-dependent defect combination laws

The combination laws for the four biaxial defect classes are determined by the multiplication rules for the conjugacy classes of the quaternion group Q (see the previous section). The results are given in Table I, and are easily understood. For example, combining a C_x defect with a C_y defect results in a configuration where **u** and **b** both rotate by $\pm 180°$, corresponding to the class C_z. The combination of two C_x defects can result in a configuration in which **u**, as well as **b**, rotate by either 0° or $\pm 360°$. If both rotate by 0°, the resulting configuration is topologically trivial; we denote the trivial class by C_0. All other possibilities give a configuration from the class $\overline{C}_0$.

We therefore reach the conclusion that the outcome of the combination of two C_x defects is not uniquely determined by the topological classification scheme (and simi-

Table 3.1: Combination laws for the 4 distinct classes (C_x, C_y, C_z and $\overline{C}_0$) of topological defects in the biaxial nematic. C_0 represents a topologically trivial configuration.

	C_0	$\overline{C}_0$	C_x	C_y	C_z
C_0	C_0	$\overline{C}_0$	C_x	C_y	C_z
$\overline{C}_0$	$\overline{C}_0$	C_0	C_x	C_y	C_z
C_x	C_x	C_x	C_0 *or* $\overline{C}_0$	C_z	C_y
C_y	C_y	C_y	C_z	C_0 *or* $\overline{C}_0$	C_x
C_z	C_z	C_z	C_y	C_x	C_0 *or* $\overline{C}_0$

larly for C_y and C_z defects). Such a property is characteristic of systems characterised by a *non-abelian* fundamental homotopy group Π_1. Both $i\sigma_x$ and $-i\sigma_x$ characterize defects from the class C_x (and can be pictured as defects in which **u** rotates by 180°, resp. −180°). When the defect configuration corresponding to the element $i\sigma_x$ is brought around a loop surrounding a C_y defect, it necessarily gets converted into a configuration of type $-i\sigma_x$: this is the meaning of the algebraic equality

$$(i\sigma_y)i\sigma_x(i\sigma_y)^{-1} = -i\sigma_x. \tag{3.3}$$

Two $i\sigma_x$ configurations combine to give a $\overline{C}_0$ defect $[(i\sigma_x)(i\sigma_x) = -1]$, whereas a $i\sigma_x$ and a $-i\sigma_x$ configuration combine to a topologically trivial configuration $[(-i\sigma_x)(i\sigma_x) = 1]$. It is therefore seen that the result of a combination of two C_x defects, which is indeterminate according to Table I, depends on *path of approach* of the two C_x defects among the C_y and C_z defects present in the system. Note that this feature is not present in systems described by an abelian fundamental homotopy group: in any abelian group G, $\alpha\beta\alpha^{-1} = \beta$ for any $\alpha, \beta \in G$, meaning that the topological character of the defect classified by β is not affected by other defects present in the system.

The four topologically stable defect types $\{C_x,\ C_y,\ C_z,\ \overline{C}_0\}$ are observed, and the predicted combination laws confirmed, in the computational investigation of

the phase-ordering process in two-dimensional biaxial nematic systems described in Chap. 5.

3.3.3 The non-crossing property of non-abelian disclination lines

So far, we have illustrated the concepts of the topological classification scheme on the case of point defects in two dimensional systems. In three spatial dimensions, the fundamental homotopy group classifies *linear* defects (which should be pictured as extending perpendicularly to the page in Figs. (3.9a-d)). Linear defects corresponding to the 4 distinct topological classes C_x, C_y, C_z and $\overline{C}_0$ were recently observed experimentally [10], and their combination laws were found to agree with those in Table I. For linear defects, there is (in addition to the property discussed in the previous paragraph) another significant consequence of the non-abelian nature of the homotopy group Q, first discussed in [11]. Imagine two line defects, corresponding to the elements α and β of Q, attempting to pass through each other (Fig. 3.10a). We can continuously deform the defect configuration in Fig. 3.10a to that in Fig. 3.10b. The defects now have passed though each other, except that they remain connected by an "umbilical cord", composed of a double segment of the β defect. We can tell if the connecting cord is topologically trivial or not by finding out if the order parameter values on a contour surrounding it (see Fig. 3.10b) map into a contractible or incontractible loop in the order parameter space. It turns out that the contour in Fig. 3.10b can be continuously deformed into the contour corresponding to the group element $\alpha\beta\alpha^{-1}\beta^{-1}$ (see Ref. [1] for detailed drawings of the deformation procedure). If α and β commute, the result is the identity element of Q, corresponding to a contractible loop, and there is no singular connecting cord. In the case $\alpha = i\sigma_x$ and $\beta = i\sigma_y$, however, the result is $\alpha\beta\alpha^{-1}\beta^{-1} = -I$, and the defects α and β will remain connected by a type $\overline{C}_0$ string. In general, whenever two line defects from two different 180° classes (i.e., C_x, C_y, or C_z) in the biaxial nematic attempt to pass through each other, the described property of "topological obstruction to defect crossing" should be manifested. A computational investigation of the physical consequences of this property

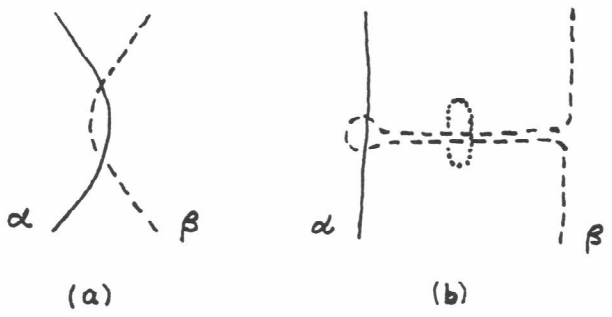

Figure 3.10: (a) Two linear defects attempting to pass through each other. (b) A continuous deformation of the configuration in (a), showing the possible presence of a singular string connecting the defects α and β. See the main text for the meaning of the dotted contour line.

in quenched three-dimensional biaxial nematic systems is currently in progress.

3.4 Higher homotopy groups

In Sec. 3.2, we saw that the conjugacy classes of the fundamental homotopy group $\Pi_1(R)$ classify topologically distinct point defects in 2D, as well as topologically distinct line defects in 3D (with cross-sections—i.e., order parameter configurations in any plane perpendicular to the defect line—corresponding to the point defects in a 2D system with the same order parameter space R).

There exist, however, topologically stable objects (order parameter configurations) other than point defects in 2D and line defects in 3D. One example—the monopole defect in the Heisenberg ferromagnet in 3D—was already discussed in Sec. 3.1. The topological stability of the configuration in Fig. 3.2 follows from the fact that the order parameter configuration on any closed surface surrounding the central singular point covers the whole order parameter space $R = S_2$ of the Heisenberg ferromagnet

exactly once. Clearly, the image of such a configuration in R cannot be continuously deformed (contracted) into a point in R. In analogy with the fundamental (or first) homotopy group $\Pi_1(R,x)$, we define the *second homotopy group* $\Pi_2(R,x)$ of R at $x \in R$ as the set of classes of maps of closed 2-dimensional surfaces into R that are homotopic at x (i.e., are continuously deformable into each other via a family of maps passing through x). The groups $\Pi_2(R,x)$ are isomorphic for all $x \in R$, and we consequently drop x from the notation.

In the case of the Heisenberg ferromagnet, the based homotopy classes of closed 2-surfaces in $R = S_2$ can be labeled by the integer giving the number of coverings, and the second homotopy group is therefore given by the group of integers: $\Pi_2(S_2) = Z$. The same is true for the uniaxial nematic, where the order parameter space is the projective plane RP_2: the analog of Fig. 3.2 with the magnetization arrows replaced by (headless) directors represents a topologically stable configuration, called the "nematic hedgehog", and the number of coverings of the order parameter space $R = RP_2$ (determining the "topological charge" M of the hedgehog) again classifies the based homotopy classes of maps of closed 2-surfaces into R, giving $\Pi_2(RP_2) = Z$.

It can be shown [1, 2] that unlike $\Pi_1(R)$, the group $\Pi_2(R)$ is abelian for all R. Topologically distinct point defects in 3D systems are therefore classified by the elements of $\Pi_2(R)$. An interesting complication, however, ensues when topologically stable *line* defects are present in the system simultaneously with point defects. For example, if a radial hedgehog (characterized by topological charge $M = 1$) in a 3D uniaxial nematic is brought around a closed path surrounding a topologically stable disclination line, a hyperbolic hedgehog (characterized by topological charge $M = -1$) results. This leads to path-dependent combination laws for point defects in the system. This situation is somewhat analogous to that described in the previous section for defects characterized by a non-abelian homotopy group, and is the consequence of the *action of* $\Pi_1(R)$ *on* $\Pi_2(R)$ (see, e.g., Ref. [1]). For systems (such as Heisenberg ferromagnets) in which the fundamental homotopy group Π_1 is trivial, no such complication occurs, and the combination laws for point defects in 3D are path

independent.

Of major interest to us will be the application of the second homotopy group to the classification of *topological textures* in 2D systems. Consider a 2D system with *homogeneous* boundary conditions for the order parameter (i.e., the order parameter field is uniform at the system boundary or at infinity). The order parameter configuration can then be viewed as a mapping of a closed two-dimensional surface into the order parameter space R (the whole boundary of the system is mapped onto one point in R). Mutually undeformable order parameter configurations in such a system are therefore classified by the second homotopy group $\Pi_2(R)$. In the case of the Heisenberg ferromagnet, the topologically distinct configurations classified by $\Pi_2(S_2) = Z$ (i.e., by an integral topological charge) may be pictured as follows. Restrict the magnetization to point "up" (i.e., in the z direction in spin space) on the boundary of the system. The homogeneous configuration of the system has a topological charge of 0. The configuration in which the magnetization at the center of the system points "down" (i.e., opposite to the magnetization direction at the boundary), and interpolates smoothly in between the center and the boundary in the way shown in Fig. 3.11, covers the order parameter sphere S_2 exactly once, and thus has a topological charge of 1. This order parameter configuration is non-singular at all points, and cannot (in a continuum system) be continuously deformed into the homogeneous configuration if the boundary condition is kept fixed.

We shall see in Chap. 6 that during the phase-ordering process in Heisenberg-type systems, numerous localized order parameter configurations of the type shown in Fig. 3.11 are spontaneously generated in the system, and determine its properties during the late stages of phase ordering.

It remains to discuss the third homotopy group of the order parameter space, $\Pi_3(R)$, defined as the set of homotopy classes of maps of closed 3-dimensional surfaces into R. In systems with spatial dimension d of physical interest (i.e., $d = 1$, 2 or 3), the third homotopy group does not classify any topologically stable singular objects (i.e., defects). However, in analogy with the case of $\Pi_2(R)$ in 2D, discussed in

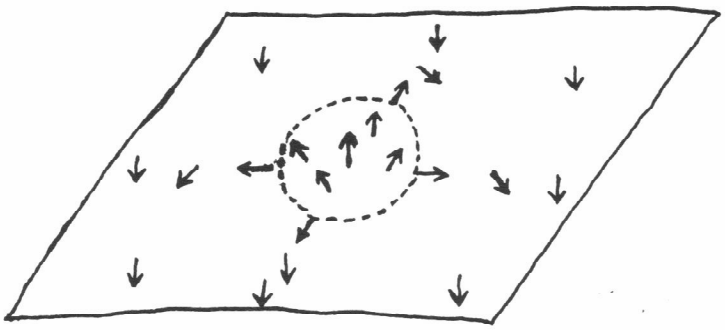

Figure 3.11: An example of a topological texture of charge 1 in the Heisenberg system in 2D.

the previous two paragraphs, $\Pi_3(R)$ classifies classifies topologically stable, but non-singular, order-parameter configurations (topological textures) in 3D systems with homogeneous boundary conditions. While it is possible to define homotopy groups $\Pi_n(R)$ with $n > 3$ for any order parameter space R, their physical meaning in ordered systems of dimension $d \leq 3$ has not been, to our knowledge, discussed in the literature.

To conclude this chapter, and for further reference, we summarize the results for the first, second and third homotopy groups for ferromagnetic and nematic systems in Table 3.2.

Table 3.2: The homotopy groups $\Pi_1(R)$, $\Pi_2(R)$, and $\Pi_3(R)$ of order parameter spaces R in planar ferromagnets, Heisenberg ferromagnets, uniaxial nematics, and biaxial nematics. Here Z is the group of integers; Z_2 is the two-element group $\{I, -I\}$; Q is the quaternion group; $\{I\}$ denotes the trivial one-element group.

system	o.p. space R	$\Pi_1(R)$	$\Pi_2(R)$	$\Pi_3(R)$
planar ferromagnet	$SO(2)$	Z	$\{I\}$	$\{I\}$
Heisenberg ferromagnet	$SO(3)/SO(2)$	$\{I\}$	Z	Z
uniaxial nematic	$SO(3)/D_\infty$	Z_2	Z	Z
biaxial nematic	$SO(3)/D_2$	Q	$\{I\}$	

References

[1] N. D. Mermin, Rev. Mod. Phys. **51**, 591 (1979).

[2] C. Nash and S. Sen, *Topology and Geometry for Physicists* (London, Academic Press, 1983).

[3] G. E. Volovik and V. P. Mineev, Pis'ma Zh. Eksp. Teor. Fiz. **24**, 605 (1976) [JETP Lett. **24**, 561 (1976)]; Zh. Eksp. Teor. Fiz. **72**, 2256 (1977) [Sov. Phys. JETP **45**, 1186 (1977)]; ibid. **73**, 767 (1977) [Sov. Phys. JETP **46**, 401 (1977)].

[4] G. Toulouse and M. Kléman, J. Phys. Lett. (Paris) **37**, 149 (1976); M. Kléman, L. Michel, and G. Toulouse, ibid. **38**, 195 (1977); M. Kléman, ibid. **38**, 199 (1977).

[5] A continuous deformation of the order parameter configuration is defined as follows. Let $\mathbf{m_A}(\mathbf{r})$ and $\mathbf{m_B}(\mathbf{r})$ be two different order parameter configurations. We say that $\mathbf{m_A}(\mathbf{r})$ is continuously deformable into $\mathbf{m_B}(\mathbf{r})$ if there exists a family of order parameter configurations $\{\mathbf{m}(\mathbf{r},t), t \in [0,1]\}$ such that $\mathbf{m}(\mathbf{r},t=0) = \mathbf{m_A}(\mathbf{r})$, $\mathbf{m}(\mathbf{r},t=1) = \mathbf{m_B}(\mathbf{r})$, and such that $\mathbf{m}(\mathbf{r},t)$ is a continuous function of t for all $t \in [0,1]$.

[6] P.-G. de Gennes and J. Prost, *The Physics of Liquid Crystals* (Oxford, Clarendon, 1993).

[7] A multiply-charged vortex in the planar ferromagnet can dissociate into a number of lower-charged vortices; it cannot, however, be converted into a topologically trivial configuration.

[8] We shall see later in this section, however, that in some cases this correspondence is not one-to-one.

[9] Recall (from Sec. 2.2) that $SO(3)$ is represented geometrically by the surface of a unit sphere in four dimensions with antipodal points identified. Any loop in $SO(3)$ connecting two antipodal points is incontractible, and $SO(3)$ is therefore not simply connected. (Notice the analogy with our discussion of loops in the projective plane RP_2.)

[10] T. De'Neve, M. Kleman, and P. Navard, J. Phys. II (France) **2**, 187 (1992).

[11] V. Poénaru and G. Toulouse, J. Phys. (Paris) **8**, 887 (1977)

[12] The conditions of the experiments of De'Neve et al. [10] did not permit the observation of the topological obstructions to the crossing of defects.

Chapter 4

Dynamical scaling in phase-ordering kinetics

Several excellent general reviews (e.g. [1, 2, 3]) of the theory of phase-ordering kinetics are available. The purpose of this chapter is more restricted in scope: primarily, it serves to review the current status of the issue of validity of *dynamical scaling* during phase ordering, and thus prepare the reader for the detailed discussion of violations of dynamical scaling that will be given for specific systems in Chapters 5–7. In Sec. 4.1, we give a brief, general introduction to the subject of phase-ordering kinetics using the example of systems with Ising-like (scalar) order parameters, concentrating in particular on the well-studied case of spinodal decomposition in binary alloys. In Sec. 4.2, we summarize which systems in spatial dimension two and higher (and without long-range interactions) are currently believed to satisfy or violate the property of dynamical scaling.

4.1 Introduction to phase-ordering kinetics: Spinodal decomposition and phase separation in binary alloys

Consider a binary atomic mixture (such as the Fe-Cr alloy) comprising of two components A and B. At high temperatures (above a certain critical temperature T_c), the thermodynamically stable phase of the system consists of the components A and B mixed at the microscopic level. If the temperature is brought below T_c, the homogeneous mixture of the two components is no longer thermodynamically stable, and the system separates into A-rich and B-rich regions. One needs to distinguish

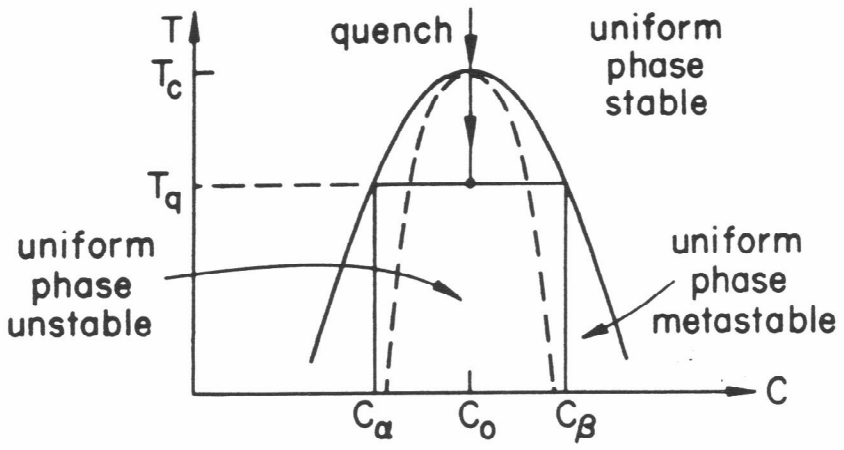

Figure 4.1: Schematic phase diagram of a binary alloy. The spinodal line is represented by the dashed curve.

two regions within the coexistence region of the phase diagram (see Fig. 4.1): the metastable region, in which the homogeneous phase still constitutes a *local* minimum of the free energy, and the system must overcome finite energy barriers in order for the phase separation process to begin; and the unstable region, in which such energy barriers are absent.

The crossover between the two regions is delineated in the phase diagram by the *spinodal line*. In the metastable region, the phase separation process begins by the nucleation of droplets of A-rich and B-rich regions driven by thermal fluctuations that are large enough to overcome the local free energy barriers, and by the subsequent growth of droplets of super-critical size. In contrast, phase separation in the unstable region begins by the development of small-amplitude, long-wavelength fluctuations in the relative concentration of A and B. See Ref. [3] for a more detailed discussion of the phase diagram.

The phase separation process following a rapid quench from the stable (high-temperature) region to the unstable region of the phase diagram is called *spinodal*

decomposition. Spinodal decomposition in binary alloys has been intensively studied both experimentally and theoretically since the 1950s, initially due to its technological importance in metallurgy, and later as a process of fundamental interest in the general context of non-equilibrium statistical physics. The experimental probes used include neutron and X-ray scattering, as well as electron microscopy. The probe of primary interest to us will be neutron scattering, which couples to the spatial variations in the local magnetic moment that are induced by the phase separation process. The measured scattering intensity at momentum transfer $\hbar k$ and at time t is proportional to the *structure factor* $S(k,t)$, defined as the (spherically averaged) Fourier transform of the real-space correlation function $C(\mathbf{r},t)$ of the order parameter $\psi(\mathbf{r},t)$; here $\psi(\mathbf{r})$is given by the difference in the local concentrations of the A-rich and B-rich phases (that is, $\psi = 0$ for the homogeneous A–B mixture).

For our purposes, it is crucial to distinguish between the early and the late stages of the spinodal decomposition process. In Fig. 4.2, we show the neutron scattering data of Katano and Izumi [6] for a wide range of times t after a quench to the unstable region region of the $Fe_{0.66}Cr_{0.44}$ alloy phase diagram. The scattering background corresponding to the homogeneous phase is subtracted (i.e., $S(k) = 0$ at $t = 0$). The development of the peak in $S(k)$ for $t > 0$ indicates the presence of structure in the system characterized by a length scale given by $2\pi/k_{\rm m}$, where $k_{\rm m}$ is the position of the maximum. It is seen that, at the earliest times, the growth of $S(k)$ is accompanied only by weak changes in $k_{\rm m}$. This indicates the amplitude growth of the initial fluctuations of the concentration difference ψ of fixed wave-length $2\pi/k_{\rm m}$, and corresponds to the initial stages of spinodal decomposition. At later times, $k_{\rm m}$ starts shifting to smaller values, indicating the presence of a *growing length-scale* in the system. This corresponds to a crossover to the regime in which the amplitude of ψ has locally achieved its full equilibrium value, and the system is divided into *domains* consisting of the stable A-rich ($\psi \simeq 1$) or B-rich ($\psi \simeq -1$) phase, separated by sharp *domain walls* at which the order parameter ψ changes from 1 to -1. The peak position $k_{\rm m}$ now corresponds to the typical inverse size of the domain, and the decrease of $k_{\rm m}$

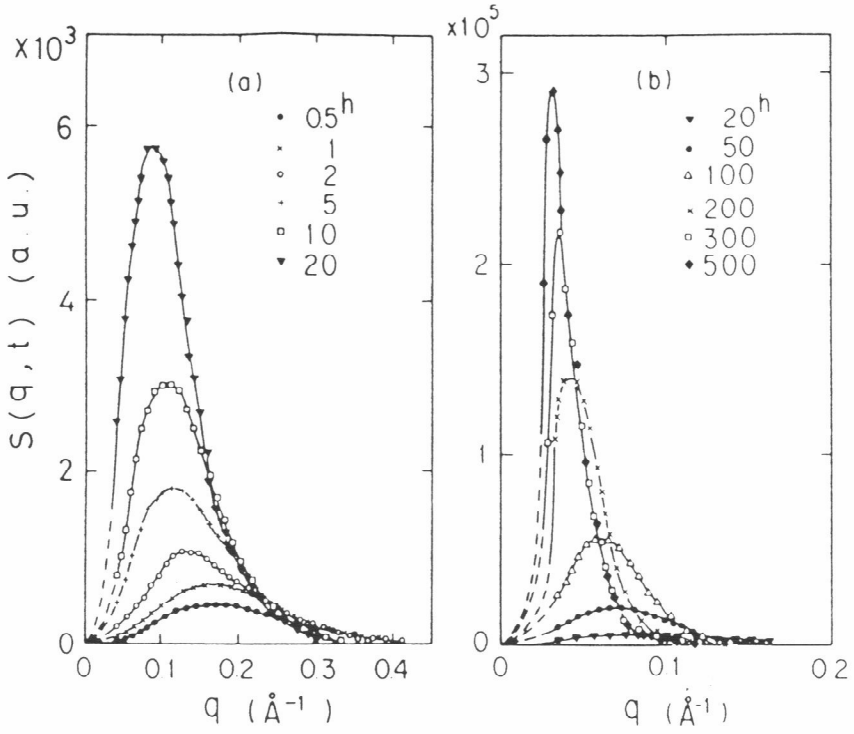

Figure 4.2: The structure factor of the binary alloy $Fe_{0.66}Cr_{0.44}$ at indicated times after the quench. Figure taken from Ref. [5].

with time corresponds to the gradual coarsening of the domain pattern.

The dynamics of the spinodal decomposition process may be described theoretically through a suitable equation of motion for the order parameter $\psi(\mathbf{r}, t)$. It is crucial that the equation of motion takes into account the fact that the order parameter is *conserved*: as the total number of atoms of each species is fixed, changes in the local composition of the alloy occur only through atomic diffusion, and the integral of $\psi(\mathbf{r}, t)$ over the system is independent of time. The appropriate dynamical model for the (coarse-grained) description of the system is the well-known model B (in the classification of Ref. [4]): The equation of continuity expressing the conservation law is

$$\frac{\partial}{\partial t}\psi + \nabla \cdot \mathbf{j} = 0\,, \tag{4.1}$$

where the current density $\mathbf{j}$ is proportional to the gradient of the chemical potential

$$\mathbf{j} = -\gamma \nabla \frac{\delta F}{\delta \psi(\mathbf{r})}\,. \tag{4.2}$$

Here, F is the appropriate (coarse-grained) free energy of the system, expressed as a functional of the order parameter field $\psi(\mathbf{r})$. A simple standard form of F that

captures the existence of the phase transition is

$$F\{\psi(\mathbf{r})\} = \int d^3r \left(\frac{\kappa}{2}(\nabla\psi)^2 + \frac{a}{2}\psi^2 + \frac{b}{4}\psi^4\right), \tag{4.3}$$

where a is proportional to $T_c - T$, and κ and b are (essentially) temperature-independent coefficients. A thermal noise term of appropriate strength would be added to the right side of Eq. (4.1) if one wishes to address situations at non-zero temperature; the $T = 0$ limit of the model will be of primary interest to us [5], and we shall therefore omit the noise term from our formulae. Substituting Eqs. (4.3) and (4.2) into Eq. (4.1), we obtain

$$\frac{1}{\gamma}\frac{\partial}{\partial t}\psi(\mathbf{r},t) = \kappa\nabla^2\psi(\mathbf{r},t) - a\psi(\mathbf{r},t) - b\psi^3(\mathbf{r},t)\,. \tag{4.4}$$

Equation (4.4) was first formulated in the context of spinodal decomposition by Cahn [7], and is usually called the Cahn-Hilliard equation. Note that the kinetic coefficient γ and the order-parameter rigidity coefficient κ in Eq. (4.4) may be set to 1 by re-defining the units of time and length, respectively.

The nonlinear character of the Cahn-Hilliard equation makes any analytical treatment very difficult. An explicit solution may be obtained only for the very early stages of spinodal decomposition, where the magnitude of the order parameter ψ is small throughout the whole system. In this case, the right-hand side of Eq. (4.4) may be linearized, and the equation is solved by a function that grows *exponentially* in time. Except perhaps at the earliest times after the quench, such exponential growth of the order parameter, and consequently of the structure factor, is not observed in experiments. To treat the late stages of the phase-ordering process successfully, the non-linearity in Eq. (4.4) must be taken into account. Furthermore, there are no small parameters in the theory that would permit a perturbative treatment. This becomes evident once we re-scale Eq. (4.4) using $\psi \to \psi\sqrt{-a/b}$, $r \to r\sqrt{\kappa/(-a)}$, and $t \to tb^{1/2}/(\gamma(-a)^{3/2})$ (recall that a is negative for temperatures below T_c) to obtain the dimensionless equation of motion

$$\frac{\partial}{\partial t}\psi(\mathbf{r},t) = \nabla^2\psi(\mathbf{r},t) + \psi(\mathbf{r},t) - \psi^3(\mathbf{r},t)\,. \tag{4.5}$$

In Ref. [8], Langer, Bar-on and Miller attempted to take into account the non-linear term in Eq. (4.5) through a closure-type approximation. Specifically, they used Eq. (4.5) to derive an equation of motion for the structure factor $S(k,t)$ that involves higher-order (Fourier-transformed) two-point correlation functions, and then closed this equation by assuming that the spatial dependence of the higher order correlations is identical to that of the lowest-order correlation. While this theory results in improved agreement with experiment in the early-time regime, it does not capture correctly the features of the asymptotic late-time regime of the phase-ordering process.

Progress in the analytical treatment of the late-stage ordering has been made possible by concentrating on the property of dynamical scaling. *The dynamical scaling hypothesis*, introduced independently by several groups (see Refs. [9, 10, 11]), states that at times long after the quench, there is a single time-dependent characteristic length-scale $L(t)$ that controls the statistical properties of the system. Stated another way, the system is statistically self-similar at successive times, up to a rescaling determined by $L(t)$. This implies that the correlation function $C(\mathbf{r},t)$ at different times t can be collapsed on to a single curve by using the characteristic length-scale:

$$C(\mathbf{r},t) = \Gamma(r/L(t))\,. \tag{4.6}$$

Consequently, the structure factor $S(k,t)$ has the scaling form

$$S(k,t) = L^d(t)g\big(kL(t)\big)\,, \tag{4.7}$$

where d is the spatial dimensionality of the system.

In Fig. 4.3, we show neutron scattering data of Gaulin et al. [12] that demonstrate the validity of the dynamical scaling form Eq. (4.7) at the late stages of phase separation in the binary alloy $Cu_{0.33}Mn_{0.67}$. The time evolution of the position k_m of the peak of the structure factor in the same data is shown in Fig. 4.4; it is seen that $k_m \sim t^{1/3}$ at late times, implying that the characteristic length scale $L(t) \sim k_m(t)^{-1} \sim t^{1/3}$ grows as a *power law in the time elapsed since the quench*, with exponent 1/3. The

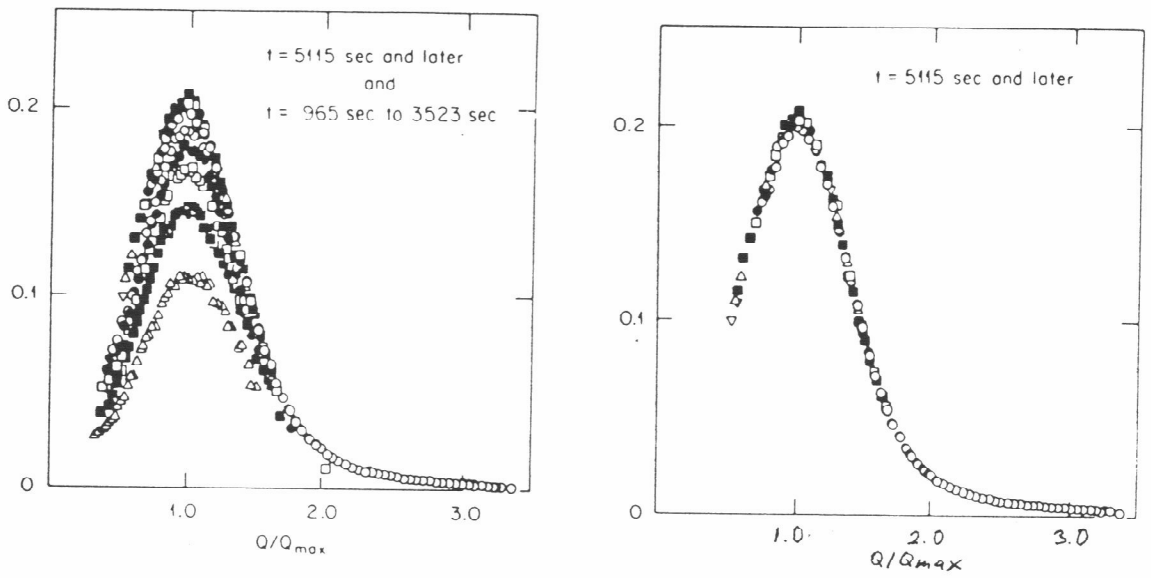

Figure 4.3: Left: The structure factor of the binary alloy $Cu_{0.33}Mn_{0.67}$, with horizontal axis re-scaled by the position k_m of the structure factor peak. Right: Collapse of the the structure factor for times after the quench exceeding 5000 sec., achieved by rescaling the vertical axis using the length scale k_m^{-1}. Figure taken from Ref. [11].

characteristic length scale is, in the present case, given simply by the typical domain size in the sample at time t. A derivation of the power law $L(t) \sim t^{1/3}$ based on the equation of motion for the interface between two domains was given first by Lifshitz and Slyozov [12] for the situation when one of the two components of the binary alloy is dominant. An argument based on scaling considerations and valid for arbitrary concentrations was later given by Huse [13]. The validity of the dynamical scaling hypothesis and the power-law growth of the characteristic length scale has also been confirmed by numerical simulations (see Ref. [14]).

Recent analytical theories, based on the introduction of auxiliary gaussian fields (see Refs. [15, 16, 17]), on a renormalization-group-type analysis (see Refs. [18]), and on energy-scaling arguments (see Refs. [19]), have been successful in predicting a number of features of the late stages of the phase-ordering process. These theories, however, *assume* the validity of dynamical scaling, rather than attempt to derive it. A systematic treatment of the property of dynamical scaling in the late stages of

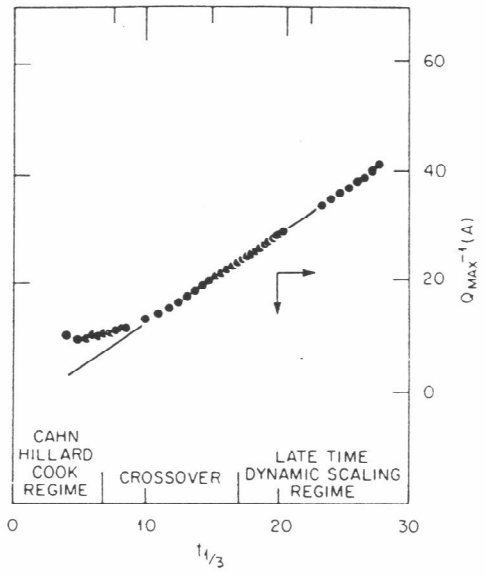

Figure 4.4: Time dependence of the length scale k_m^{-1} in the data of Gaulin et al. Figure taken from Ref. [11].

phase ordering remains an open theoretical challenge.

4.2 Inventory of dynamical scaling in phase-ordering systems in spatial dimension two and higher

In the previous section, we introduced the subject of phase-ordering kinetics with the example of binary alloys. The equation of motion, Eq. (4.4), is also valid for a number of other systems that are described by a scalar conserved order parameter, such as Ising ferromagnets, and various binary mixtures. (A notable exception is provided by the binary fluid system, for which hydrodynamic effects must be taken into account, so that the simplest equation of motion that can describe the late stages of phase separation is considerably more complicated). A second important class of systems is that described by a scalar but *non-conserved* order parameter (examples include antiferromagnets and superfluid He^4). For these systems, the equation of motion is given by

$$\frac{\partial}{\partial t}\psi = -\gamma \frac{\delta F}{\delta \psi(\mathbf{r})} \tag{4.8}$$

(i.e., model-A dynamics with the noise term omitted), where F is again the coarse-grained free energy, which is commonly taken to have the form of Eq. (4.3). A number of numerical simulations have demonstrated the validity of dynamical scaling in the late stages of phase ordering governed by this model.

In recent years, systems described by more complex (i.e., non-scalar) order parameters have been studied extensively. Depending on the presence or absence of the conservation law, these systems are again described by Eq. (4.1) or Eq. (4.8), where the order parameter ψ has now a more complicated character: for example, the scalar ψ is replaced by a vector in the case of planar or Heisenberg ferromagnets, and by a tensor in the case of nematic liquid crystals.

It was found that, as a general rule, the dynamical scaling hypothesis holds for these more complicated systems. There are, however, notable exceptions to this rule. In the remainder of this section, we list the systems for which the validity of the dynamical scaling property has been disproved or questioned. Naturally, the list is not complete—a number of systems for which violations of dynamical scaling may be expected to occur have not yet been extensively studied. We restrict our attention to systems in spatial dimension two and higher, without long-range interactions, and undergoing a quench that results in a random initial order parameter configuration with no bias (i.e., a "critical" quench).

The only two systems (in dimension two or higher) for which an exact late-time analytical solution to the equation of motion has been found are the conserved and non-conserved *spherical models*, i.e., models described by the $O(N)$ symmetric vector order parameter in the limit $N \to \infty$. It has been shown [21] that dynamical scaling does not hold in the conserved case, but does hold in the non-conserved case. The violation of scaling in the conserved case is related to the occurrence, in the result for the structure factor $S(k,t)$, of two length scales with different growth laws: whereas the height of the peak of $S(k,t)$ has a time dependence that implies a $t^{1/4}$ growth law, the position of the peak is inversely proportional to $(t/\ln(t))^{1/4}$. Recall (from Chapter 3) that no topologically stable defects occur in the spherical model in any

spatial dimension; it is therefore not possible to give an intuitive explanation of the origins of the scaling violations in terms of the behavior of topological objects.

The situation is different in the case of the non-conserved $O(3)$ symmetric (i.e., Heisenberg-type) vector model in two spatial dimensions. It has been shown [22, 23] that strong violations of dynamical scaling occur in the numerical implementation of phase ordering in this model. These violations are related to the occurrence of numerous topological textures—topologically stable, but non-singular objects of variable size. A detailed discussion of the phase-ordering process in this system will be given in Chapters 6 and 7.

For the last case that we shall discuss in this section, the question of whether dynamical scaling is violated is still open. In the numerical investigations of two systems supporting topologically stable point defects in two spatial dimensions—namely, in the non-conserved $O(2)$ vector model in 2d (Ref. [24]) and in the 2D liquid crystal system (Ref. [25])—*weak* violations of dynamical scaling have been observed. By "weak", we mean that the structure factor appears to satisfy the scaling form Eq. (4.7), but the growth law of the length scale $L(t)$ (the correlation length of the order parameter) is found to differ from the growth law for the average separation of topological defects in the system. A more detailed discussion of this behavior in terms of general properties of point defects in two dimensions will be given in Sec. 5.5.1 of the following chapter.

References

[1] A. J. Bray, Adv. Phys. **43**, 357 (1994).

[2] G. F. Mazenko, in *Formation and Interactions of Topological Defects*, edited by A.-C. Davis and R. Brandenberger (Plenum Press, New York, 1995), p. 63.

[3] J. D. Gunton, M. San Miguel and P. S. Sahni, in *Phase Transitions and Critical Phenomena*, edited by C. Domb and J. L. Lebowitz (Academic Press, New York, 1983), Vol. 8.

[4] P. C. Hohenberg and B. I. Halperin, Rev. Mod. Phys. **49**, 435 (1977).

[5] The form of the structure factor $S(k,t)$ during the late stages of phase ordering in generic systems is believed not to depend of the strength of thermal noise (see Ref. [1]).

[6] S. Katano and M. Iizumi, Phys. Rev. Lett. **52**, 835 (1984).

[7] J. W. Cahn, Acta Metall. **14**, 1685 (1966); J. W. Cahn and J. E. Hilliard, J. Chem. Phys. **28**, 258 (1958).

[8] J. S. Langer, M. Bar-on, and H. D. Miller, Phys. Rev. A **11**, 1417 (1975).

[9] K. Binder and D. Stauffer, Phys. Rev. Lett. **33**, 1006 (1974).

[10] J. Marro, J. L. Lebowitz, and M. H. Kalos, Phys. Rev. Lett. **43**, 282 (1979).

[11] H. Furukawa, Phys. Rev. Lett. **43**, 136 (1979).

[12] B. D. Gaulin, S. Spooner and Y. Morii, Phys. Rev. Lett. **59**, 668 (1987).

[13] I. M. Lifshitz and V. V. Slyozov, J. Phys. Chem. Solids **19**, 35 (1961).

[14] D. A. Huse, Phys. Rev. B **74**, 7845 (1986). In fact, Huse argued for a more precise form of the growth law, $L(t) = At^{1/3} + R_0$. The straight line in Fig. 4.4 is a fit to this form.

[15] A. Shinozaki and Y. Oono, Phys. Rev. E **48**, 2622 (1993), and references therein.

[16] T. Ohta, D. Jasnow and K. Kawasaki, Phys. Rev. Lett. **49**, 1223 (1982).

[17] G. F. Mazenko, Phys. Rev. Lett. **63**, 1605 (1989); Phys. Rev. B **42**, 4487 (1990); ibid. B **43**, 5747 (1991).

[18] A. J. Bray and K. Humayun, Phys. Rev. E **48**, 1609 (1993).

[19] A. J. Bray, Phys. Rev. Lett. **62**, 2841 (1989); Phys. Rev. B **41**, 6724 (1990).

[20] A. D. Rutenberg and A. J. Bray, Phys. Rev. E **49**, 27 (1994); ibid. E **51**, 5499 (1995).

[21] A. Coniglio and M. Zannetti, Europhys. Lett. **10**, 575 (1989).

[22] M. Zapotocky and W. J. Zakrzewski, Phys. Rev. E **51**, R5189 (1995).

[23] A. D. Rutenberg, Phys. Rev. E **51**, R2715 (1995).

[24] R. E. Blundell and A. J. Bray, Phys. Rev. E **49**, 4925 (1994).

[25] M. Zapotocky, P. M. Goldbart and N. Goldenfeld, Phys. Rev. E **51**, 1216 (1995).

Chapter 5

Phase ordering in uniaxial and biaxial nematic films

5.1 Introduction

When a system is quenched from a high-temperature equilibrium phase, it undergoes a phase ordering process in which the highly nonequilibrium state, generated during the quench, slowly evolves towards the low-temperature phase. The process of phase ordering following the quench has been extensively studied for systems described by a scalar order parameter (see the discussion in the previous chapter) and, more recently, also for systems with continuous symmetries. Much of the analytical [1] and numerical [2, 3] investigations of the continuous-symmetry cases have concentrated on phase ordering in the $O(N)$-symmetric *vector* model. Very recently, nematic liquid crystals have proven to be useful for experimental investigations of phase ordering [7, 8, 9], triggering several theoretical investigations [4, 5, 6].

In many experimental and numerical studies it has been observed that *dynamical scaling* holds for the static correlation function at late stages of phase ordering in a variety of systems (see the previous chapter for a more detailed discussion). The validity of dynamical scaling, however, has repeatedly been questioned [10, 2] for the case of the 2D $O(2)$ vector model (i.e., the $O(2)$ vector model in 2 spatial dimensions). In particular, it has been observed that the correlation length (i.e., the length-scale required to cause the collapse the static correlation function) and the defect separation length appear to grow in time with distinct power-laws.

In systems where topologically stable defects exist, many of the universal char-

acteristics of the late stages of phase ordering can be obtained by considering the properties of the defects and their interactions alone. In $O(N)$ vector systems, uniaxial nematics, and biaxial nematics, these properties are distinct from one another [13], and thus one might anticipate differences between the phase ordering of such systems. The study of ordering in systems described by a nematic order parameter is therefore of considerable theoretical interest, and should provide insight into the dependence of the ordering process on the details of order parameter symmetry.

The purpose of this chapter is to report results from a cell-dynamical scheme (CDS) simulation of phase ordering in two-dimensional samples of uniaxial and biaxial nematic liquid crystals. By a two-dimensional sample, we mean a film with thickness that is smaller than the equilibrium correlation length prior to the quench. We emphasize that while the system has two spatial dimensions, the molecules are allowed to point in any direction in three-dimensional space and, correspondingly, the order parameter is a three-dimensional (rank-two symmetric traceless) tensor. We compute the time-dependence of the correlation function, structure factor, energy density, and number densities of the topologically distinct defect species. In common with the 2D $O(2)$ vector model, the system supports point defects, and thus the question of the validity of dynamical scaling is also expected to be relevant here. In the case of a biaxial nematic, we also study the additional features arising from the fact that the system supports four topologically non-equivalent defect species, and make predictions that should be verifiable experimentally by direct optical visualization of the defects.

This chapter is organized as follows. Following the Introduction, we present, in Sec. 5.2, the details of our CDS approach. In Sec. 5.3, we give results for the evolution of the static nematic correlation function, the correlation length and the energy density, and discuss their implications. In Sec. 5.4, we review the topological classification of defects in uniaxial and biaxial nematics, give algorithms for finding and identifying defects, and illustrate the combination laws among defects using events from our simulation. In Sec. 5.5.1, we present results for the time-dependence of the

density of defects after quenching to the uniaxial nematic phase, and give a detailed discussion of the effective growth-exponent for the average defect-separation. Defects in biaxial nematics have properties qualitatively different from those of uniaxial nematics: there are four topologically distinct species of defects, and their combination laws are non-Abelian. In Sec. 5.5.2, we present results for the time-dependence of the populations of the four topologically-stable species, and discuss the physical mechanism that causes certain species to dominate at late times. In Sec. 5.6, we make some concluding remarks.

We end this Introduction with a summary of our results. We find that the static correlation function and structure factor *appear* to collapse to scaling curves over a wide range of times. In the uniaxial quench case, the correlation length $L_{\rm cor}(t)$ required to achieve collapse grows approximately as a power-law in time, $L_{\rm cor}(t) \sim t^{\phi_{\rm cor}}$, with an exponent $\phi_{\rm cor} = 0.407 \pm 0.005$. The average separation between defects, $L_{\rm def}(t)$, also grows as a power-law, $L_{\rm def}(t) \sim t^{\phi_{\rm def}}$, with an exponent $\phi_{\rm def} = 0.374 \pm 0.007$, distinctly lower than $\phi_{\rm cor}$. As we discuss in Sec. 5.5.1, the discrepancy between $\phi_{\rm cor}$ and $\phi_{\rm def}$ is *inconsistent* with the strict collapse of the correlation function, and thus indicates a violation of dynamical scaling — a violation that is not apparent from our results for the correlation function alone. The length characterizing the decay of the energy density, $L_{\rm en}(t) \sim t^{\phi_{\rm en}}$, has the effective growth exponent $\phi_{\rm en} = 0.320 \pm 0.007$. As we show in Sec. 5.3.4, the discrepancy between $\phi_{\rm en}$ and $\phi_{\rm cor}$ does not, in fact, indicate the violation of dynamical scaling. The effective growth exponents, $\phi_{\rm cor}$, $\phi_{\rm def}$ and $\phi_{\rm en}$, are significantly smaller than the value of 0.5, suggested by naive scaling arguments [19]. A similar reduction of $\phi_{\rm def}$ has been observed in simulations of the 2D $O(2)$ vector model [2, 10]. This has been attributed to logarithmic corrections to the true asymptotic power-law growth of the separation of defects, which was motivated by an analysis of the mutual annihilation of an isolated defect-antidefect pair [12]. In order to check the relevance of the two-defect problem for scaling properties in ordering of large nematic systems, we have performed simulations of the annihilation process of an isolated pair of uniaxial nematic defects. We find that the distance

between the defects decays as a power-law in the time remaining until annihilation with the growth exponent of 0.375 ± 0.007, consistent with the value of ϕ_{def} given above. The reduced value of the growth exponent in the two-defect problem can be explained by arguments analogous to those used in the treatment of the defect-antidefect annihilation process in Ref. [12].

For the case of biaxial nematics, of the four topologically-distinct species of defects only two are present in large numbers at late times, giving growth laws with powers of 0.391 ± 0.007 and 0.366 ± 0.007. We characterize the different stages of ordering in the biaxial system in terms of the dominant defect-defect reactions. As in the uniaxial case, we observe a discrepancy between ϕ_{cor} and the growth exponents of the defect separations for each species, indicating a violation of dynamical scaling.

Biaxial nematic media provide perhaps the simplest example of an ordered medium with a non-Abelian fundamental homotopy group [13]. To the best of our knowledge, phase ordering in such systems has not been previously studied. While the physical effects of the non-commutative nature of the fundamental homotopy group are expected to be more profound in three spatial dimensions[14], some consequences are already apparent in the present work.

The results described in this chapter where obtained in collaboration with Paul M. Goldbart and Nigel Goldenfeld.

5.2 Cell dynamical scheme for the entire nematic order parameter

We adopt the standard characterization [17] of the nematic order in the vicinity of the position $\mathbf{r}$ at time t in terms of the order parameter field $Q_{\alpha\beta}(\mathbf{r}, t)$. This order parameter is a traceless symmetric second rank tensor, with Cartesian indices (with $\alpha, \beta, \ldots = 1, 2, 3$). The eigenvalue of $Q_{\alpha\beta}$ largest in absolute magnitude gives the degree of orientation in the preferred direction, the corresponding eigenvector identifying the preferred direction $\mathbf{u}$ (i.e., the so-called director, in the uniaxial nematic case). The difference between the remaining two eigenvalues characterizes the degree

of biaxiality, with the biaxiality axis **b** specified by the eigenvector corresponding to the eigenvalue having the second largest magnitude [15].

Before the quench, the local value of the order parameter (coarse-grained on the scale of the equilibrium correlation length prior to the quench) is zero. After the quench, the eigenvalues of $Q_{\alpha\beta}$ start to grow locally, and the eigenvectors start to become correlated spatially. We describe the time-evolution of the order parameter using the time-dependent Ginzburg-Landau equation appropriate for a non-conserved order parameter:

$$\frac{\partial}{\partial t}Q_{\alpha\beta}(\mathbf{r},t) = -\frac{\delta}{\delta Q_{\alpha\beta}(\mathbf{r},t)}F[Q] \tag{5.1}$$

(in which it is understood that only the traceless symmetric part of the right-hand side is retained), where $F[Q] = \int d^2x\mathcal{F}(Q)$ and $\mathcal{F}(Q)$ is the appropriate free energy density.

A homogeneous part of $\mathcal{F}(Q)$ adequate for the description of the isotropic-nematic phase transition can be taken to be [16]

$$\mathcal{F}_h(Q) = A\,\mathrm{Tr}\,Q^2 + B\,\mathrm{Tr}\,Q^3 + C\left(\mathrm{Tr}\,Q^2\right)^2 + E\left(\mathrm{Tr}\,Q^3\right)^2, \tag{5.2}$$

with $C > 0$, and the quench corresponds to a change in A, from large and positive in the isotropic phase to negative in the nematic phase. For $E = 0$, Eq. (5.2) describes a uniaxial nematic; for $E > 0$, it describes a biaxial nematic. To construct an effective numerical scheme for the evolution governed by Eq. (5.1), we use the CDS approach (see below), in which one must find the fixed points of Eq. (5.1) and Eq. (5.2) must be ascertained. When diagonalized, $Q_{\alpha\beta}$ can be parametrized (up to a relabeling of axes) as

$$Q = \begin{pmatrix} 2x & 0 & 0 \\ 0 & -x-y & 0 \\ 0 & 0 & -x+y \end{pmatrix}, \tag{5.3}$$

with $x \geq 0$ and $0 \leq y < 3x$. (Then $2x$ is the leading eigenvalue if $x < y$, $\frac{3}{2}x$ corresponds to the "degree of ordering" S, as usually defined for uniaxial nematics [17], and y characterizes the degree of biaxiality). The scalar density $\mathcal{F}_h(Q)$ can be expressed as a function of x and y.

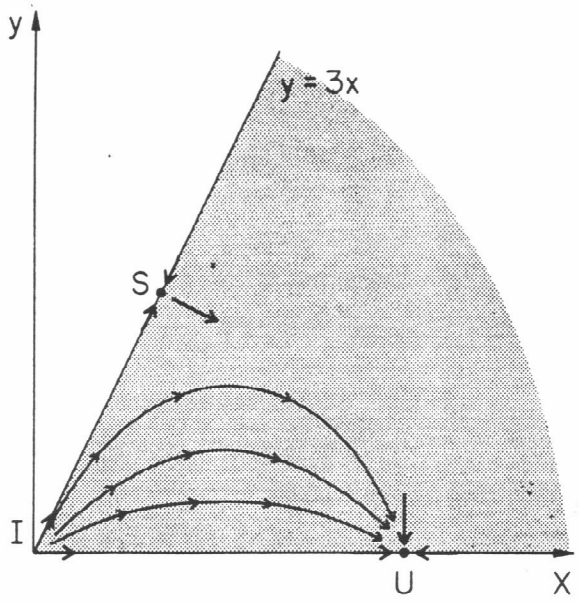

Figure 5.1: fixed point diagram for the evolution of the order-parameter magnitudes x and y following a uniaxial quench. Here I is the unstable fixed point corresponding to the isotropic phase, S is the saddle fixed point on the "discotic" uniaxial axis $y = 3x$, and U is the fixed point corresponding to the stable uniaxial phase.

Finding and characterizing the stationary points of $\mathcal{F}_h(x, y)$ yields the fixed point diagrams shown in Fig. 5.1 and Fig. 5.2. For a uniaxial quench ($E = 0$), one finds an unstable fixed point at the origin ($x = 0$, $y = 0$), corresponding to the unstable isotropic phase, and a stable fixed point on the uniaxial line $y = 0$, corresponding to the stable uniaxial nematic phase. Furthermore, one finds a saddle fixed point on the line $y = 3x$. The line $y = 3x$ corresponds to a uniaxial phase [two of the eigenvalues in Eq. (5.3) being equal]; however, the eigenvalue largest in absolute value is $-4x$, and is therefore negative. This indicates "discotic" nematic ordering — for needle-like molecules, it would mean that the long axis of each molecule lies, on average, perpendicular to the "director " (see Fig. 5.3). Analysis of $\mathcal{F}_h(x, y)$ shows that the fixed point on the $y = 3x$ axis is always present, being stable in the discotic uniaxial direction (along $y = 3x$), and unstable in the biaxial direction (perpendicular to $y = 3x$). The implication of this fixed point structure is that the time evolution, determined by Eqs. (5.1) and (5.2), of the order parameter magnitudes x and y is as

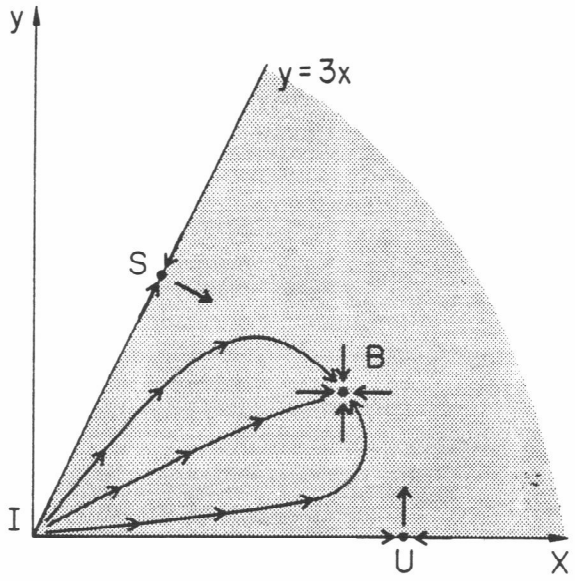

Figure 5.2: fixed point diagram for the evolution of the order-parameter magnitudes x and y following a biaxial quench. The flow is directed towards the stable biaxial fixed point B with the help of the two uniaxial saddle fixed points U and S.

schematically indicated in Fig. 5.1. Similar conclusions were reached in Ref. [6].

For the biaxial quench ($E > 0$), the stable fixed point on the uniaxial $y = 0$ axis changes to a saddle fixed point, and redirects the flow towards the stable biaxial fixed point, which is located at $x > 0$ and $0 < y < 3x$ (see Fig. 5.2). The primary difference between the uniaxial quench and the biaxial quench thus lies in the different structure of the fixed points.

In addition to the homogeneous contribution to the free energy, there is also a contribution that couples the value of the order parameter in different spatial regions. In a nematic system, this elastic energy has three independent contributions, one each from splay, bend, and twist [17]. To simplify calculations, the three corresponding independent elastic constants are commonly taken to be equal (i.e., the so-called one-constant approximation is often made). In this case, the free energy of a nematic takes the form

$$\mathcal{F}(Q) = \mathcal{F}_h(Q) + M(\partial_\alpha Q_{\beta\gamma})(\partial_\alpha Q_{\beta\gamma}) \,, \tag{5.4}$$

in which $\mathcal{F}_h$ is given by Eq. (5.2) and M is the (single) elastic constant. The functional

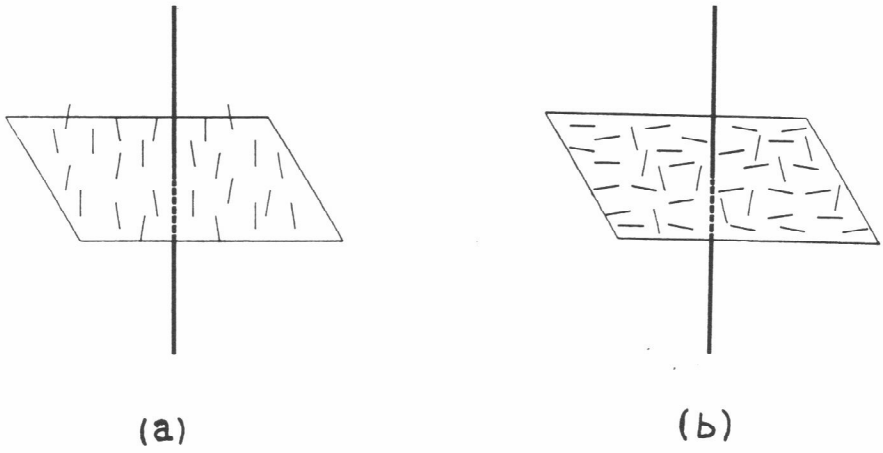

Figure 5.3: Two types of uniaxial nematic ordering resulting in the same overall preferred direction of orientation (the "director"): (a) In "elongated" ordering, the long axis of each molecule lies, on average, parallel to the "director". (b) In "discotic" ordering, the long axes of the molecules lie, on average, in the plane perpendicular to the "director", with random orientations within the plane.

derivative $\delta F/\delta Q$ then yields a term $\nabla^2 Q_{\alpha\beta}$ in the equation of motion, Eq. (5.1), and thus the intercell coupling has a purely diffusive character.

We simulate the dynamics of the order parameter $Q_{\alpha\beta}(\mathbf{r}, t)$ using the CDS technique [18]. The CDS method has proven effective for simulating phase ordering in systems with $O(N)$ vector order parameters (both nonconserved and conserved; see Refs. [2, 3]). Recently, ordering of uniaxial nematics in 2 and 3 spatial dimensions has been studied using CDS techniques [4, 5]. In the case of biaxial nematics, we encounter a situation in which more then one scalar (i.e., the 2 independent eigenvalues of the tensor $Q_{\alpha\beta}$) can be constructed from the order parameter (an additional complication is that a linear constraint, $\mathrm{Tr}\, Q = 0$, is imposed on the order parameter components). We shall see below that the CDS approach can be straightforwardly generalized to the present case.

In the CDS approach, the system is divided into cells of the size of the equilibrium

correlation length before the quench, and each cell is characterized by a value of the order parameter $Q_{\alpha\beta}$. As we are concerned with a quench from a high temperature, immediately after the quench the values of $Q_{\alpha\beta}$ in each cell are independent (i.e, spatially uncorrelated), identically distributed random variables. Each time step of the evolution of the $Q_{\alpha\beta}$ field is divided into two sub-steps: single-cell evolution, and intercell coupling.

In the single-cell evolution step, which reflects the homogeneous contribution to the free energy, we must assign a new value $Q_{\rm new}$ to the order parameter in a given cell as a function of the old value in that cell $Q_{\rm old}$. By using symmetry arguments one can show that the most general symmetric traceless function $Q_{\rm new}$ of a symmetric traceless tensor $Q_{\rm old}$ can be written as

$$Q_{\rm new} = f\left(\mathrm{Tr}\, Q^2_{\rm old}, \mathrm{Tr}\, Q^3_{\rm old}\right) Q_{\rm old} + g\left(\mathrm{Tr}\, Q^2_{\rm old}, \mathrm{Tr}\, Q^3_{\rm old}\right) Q^2_{\rm old}\big|_{\rm dt}\,, \tag{5.5}$$

where f and g are arbitrary (scalar) functions of the two independent scalars $\mathrm{Tr}\, Q^2_{\rm old}$ and $\mathrm{Tr}\, Q^3_{\rm old}$, and $Q^2|_{\rm dt} \equiv Q^2 - \frac{1}{3} I\, \mathrm{Tr}\, Q^2$ (where I is the unit matrix) is the traceless part of Q^2.

The choice of the functions f and g is motivated by the form of the homogeneous free energy, Eq. (5.2). As the asymptotic dynamics of the order parameter is governed by the fixed point structure of Eqs. (5.1) and (5.2), we are free to choose f and g in any (computationally efficient) way, as long as the map, Eq. (5.5), has the fixed point structure of Fig. 5.1 or Fig. 5.2. [One can pass from the independent scalars $\mathrm{Tr}\, Q^2$ and $\mathrm{Tr}\, Q^3$ to x and y, as defined above, by using the identities $x = \sqrt{\frac{1}{6}\mathrm{Tr}\, Q^2}\cos\left(\frac{1}{3}\arccos(\sqrt{6}\mathrm{Tr}\, Q^3/(\mathrm{Tr}\, Q^2)^{3/2})\right)$ and $y = \sqrt{\frac{1}{2}\mathrm{Tr}\, Q^2 - 3x^2}$]. The numerical results in the remainder of this chapter have been obtained using the choice

$$f(x,y) = 1.3\tanh(x)/x - x\, g(x,y) \tag{5.6}$$

$$g(x,y) = 1/4 \tag{5.7}$$

in the case of a uniaxial quench, and

$$f(x,y) = 1.3\tanh(x)/x - x\, g(x,y) \tag{5.8}$$

$$g(x,y) \;=\; -1/4 + b\,y \tag{5.9}$$

in the case of the biaxial quench. The parameter b controls the strength of biaxiality. It is straightforward to check that the choices reflected in Eqs. (5.2) and (5.2) give the fixed point structure of Fig. 5.1 and Fig. 5.2, respectively, with fixed point locations (x, y) at (0, 0), (0.977, 0), (0.337, 1.011) [in the biaxial case, the location of the third fixed point depends on the parameter b], and (for the biaxial quench only) at (0.977, $1/4b$). The results presented in the remainder of this chapter where obtained using the choice $b = 1$, with the exception of the data in Fig. 5.6b, where the value $b = 0.5$ was used.

Note that Eqs. (5.3) and (5.5) imply that $x' = x\Big(f(x,y) + xg(x,y)\Big) - \frac{1}{3}y^2 g(x,y)$, where x and y are calculated from $Q_{\rm old}$, and x' is calculated from $Q_{\rm new}$. Our choices of f and g [for both the uniaxial (Eqs. /5.2/) and biaxial (Eqs. /5.2/) quench) therefore ensure that $x' = 1.3\tanh(x)$ for $y = 0$ — that is, the evolution of the degree x of uniaxial ordering is (in the absence of biaxiality) given by the standard CDS choice (see, e.g., Ref. [18]) for the evolution of the order-parameter magnitude. We find Eqs. (5.2b) and (5.2b) to be the simplest computationally-efficient choices for $g(x, y)$ ensuring the correct properties of the flow in the biaxiality-strength (y) direction.

The intercell coupling contribution to the CDS evolution resulting from the elastic contribution to the free energy in Eq. (5.4) can be expressed as

$$Q_{\rm new} = Q_{\rm old} + D\left(Q_{\rm old} - \langle\langle Q\rangle\rangle\right). \tag{5.10}$$

Here, $Q_{\rm new}$ is the value of Q in a certain cell after the update, D is a parameter reflecting the elastic coupling, and the term $\langle\langle Q\rangle\rangle$, defined by

$$\langle\langle Q\rangle\rangle \equiv \frac{1}{6}\sum_{\rm nn} Q + \frac{1}{12}\sum_{\rm nnn} Q\,, \tag{5.11}$$

arises from a discretization of the Laplacian that retains nearest (nn) and next nearest (nnn) neighbor terms [18].

The quenches that we are considering are envisaged to start at high temperatures, at which the equilibrium phase is the disordered, isotropic phase. We take as the

initial condition for our CDS simulation a configuration representative of this phase, in which Q is zero in each cell, apart from small, uncorrelated, isotropically distributed, random fluctuations. Specifically, the random initial order parameter in each cell was obtained by generating 3 random numbers that add to zero (i.e., 3 eigenvalues of Q) from a uniform distribution of width 0.2, and then rotating the resulting diagonal matrix using random Euler angles. To summarize the scheme, we start with a random initial configuration (satisfying periodic boundary conditions), and then repeatedly apply the steps specified in Eqs. (5.5) and (5.10), using the appropriate map, i.e., Eq. (5.2) or (5.2).

The results presented in the remainder of this chapter were obtained in runs using a variety of choices of the diffusion constant D (in the range $D = 0.1$ to 0.5). Higher values of D were found to be more advantageous for accessing the asymptotic regime in a given number of time steps. It was, however, necessary to use lower values of D in the detailed investigation of the evolution of the populations of the topological defects because, at the early stages of ordering, values of $D \simeq 0.5$ lead to the presence of a number of cells where the eigenvalue largest in absolute value is negative (that is, the corresponding points in Fig. 5.1 and 5.2 lie above the line $y = x$), which invalidates the notion of a topologically stable defect (see Section 5.4.1). We found that by "hardening" the random initial configuration (i.e., allowing it to evolve for a small number of time steps with D set to zero, so that the order parameter magnitudes x and y approach the fixed point without affecting the *orientation* of the order parameter), and subsequently using the value $D = 0.1$ to evolve the system, we were able both to ensure that thesis3.texthe topological defects are well-defined even at the earliest stages of ordering and to access the asymptotic late time regime.

We are concerned with quenches to zero temperature, so that thermal fluctuations play no role in the dynamics. It was, however, commonly observed in previous numerical investigations of zero-temperature quenches that freezing into metastable configurations can occur (e.g., Ref. [12]). Therefore, to test whether freezing effects were influencing our simulation, we performed a limited number of runs in the pres-

ence of *noise* (i.e., a small-amplitude random configuration was added to the order parameter at each time step). The results were observed to be insensitive to noise, up to noise strengths capable of spontaneously generating numerous defect pairs. All results in the asymptotic regime were observed to be independent of the chosen value of D and the system size (with the exception of the transition in the rate of change of the effective growth exponents, mentioned in the following Section).

5.3 Correlation function, structure factor and energy density.

5.3.1 Collapse of the correlation function and the structure factor.

In its usual formulation, the dynamical scaling hypothesis [1, 11] states that at late times of phase ordering, there is a single time-dependent characteristic length-scale $L(t)$ that controls the statistical properties of the system. Stated another way, the system is statistically self-similar at successive times, up to a rescaling determined by $L(t)$. It will be crucial in the detailed analysis of the data from our simulation to distinguish two statements which are often taken to be consequences of dynamical scaling:

(a) The correlation function $C(\mathbf{r}, t)$ at different times t can be collapsed on to a single curve by using the characteristic length-scale $L_{\rm cor}(t)$:

$$C(\mathbf{r}, t) = \Gamma(r/L_{\rm cor}(t)) \tag{5.12}$$

where $\Gamma(y)$ is a scaling function.

(b) The length scale $L_{\rm cor}(t)$ used to obtain the collapse of the correlation function determines the characteristic length-scale of all time-dependent macroscopic quantities in the system. Thus, the energy density of the system as well as the number density of point defects present decay as $L_{\rm cor}(t)^{-d}$, where d is the spatial dimensionality of the system.

We shall see in our simulations of the 2D nematic system that statement (a) is apparently very well satisfied over a wide range of times, but that statement (b) is

rather strongly violated. A detailed discussion of whether this indicates a breakdown of dynamical scaling will be given in Secs. 5.3.4 and 5.5.1.

The characteristic length scale $L_{\rm cor}(t)$ is usually assumed to grow asymptotically as a power law of time, $L_{\rm cor}(t) \sim t^{\phi_{\rm cor}}$ for t large. It should be noted that such an assumption does not, in principle, follow from the dynamical scaling hypothesis. The length-scales investigated in our simulation grow as approximate power-laws at late times. However, the growth exponents for these length-scales differ and, moreover, are significantly lower than the value $\phi_{\rm cor} = 0.5$, which is usually observed in experiments on phase ordering in systems with nonconserved order parameters. The latter issue is discussed in detail in Sec. 5.5.1.

We now present the results for the correlation function and the structure factor from our simulation. For the tensorial nematic order parameter $Q_{\alpha\beta}(\mathbf{r}, \mathbf{t})$, a scalar correlation function can be defined by

$$C(r,t) = \frac{\left\langle \mathrm{Tr}\left[Q(\mathbf{0},t)\, Q(\mathbf{r},t)\right]\right\rangle}{\left\langle \mathrm{Tr}\, Q(\mathbf{0},t)^2\right\rangle}\,, \tag{5.13}$$

where $\langle\cdots\rangle$ denotes averaging over the positions (i.e., $\mathbf{0}$), and over the orientations of $\mathbf{r}$. The correlation function is normalized so that $C(0,t) = 1$. We define the correlation length $L_{\rm cor}(t)$ at time t through

$$C(r,t)\Big|_{r=L_{\rm cor}(t)} = 1/2\,. \tag{5.14}$$

Figure 5.4 shows the correlation functions $C(r,t)$ obtained from our simulation of ordering in a biaxial system at a sequence of times. In Fig. 5.5, data from Fig. 5.4 are rescaled using the correlation length defined by Eq. (5.14). We see that a good collapse of the correlation function is obtained in the range of times $200 < t < 5000$. A collapse of similar quality is also obtained for the correlation function in the uniaxial system. We have, in addition, calculated the structure factor $S(k,t)$ [i.e., the spatial Fourier transform of $C(r,t)$], and used the correlation length defined by Eq. (5.14) to check the validity of the scaling form

$$S(k,t) = L_{\rm cor}^2(t)\, g\Big(k L_{\rm cor}(t)\Big)\,. \tag{5.15}$$

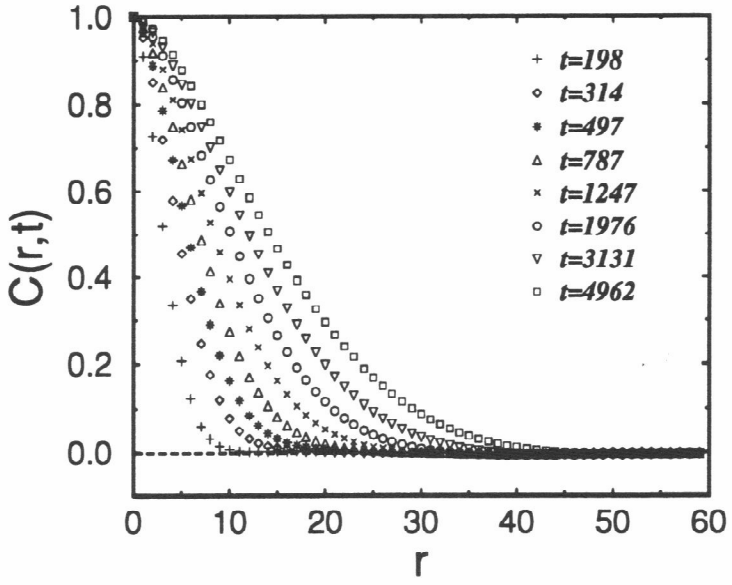

Figure 5.4: Correlation function $C(r,t)$ at specified values of time t following the biaxial quench. The data were obtained by averaging over 68 configurations of a 256×256 system, with diffusion constant D=0.1.

The resulting scaling functions $g(kL_{\rm cor}(t))$ for the uniaxial and biaxial quenches are plotted in Figs. 5.6a and 5.6b. (The "tail" of $g(y)$ (i.e., the asymptotic behavior of $g(y)$ in the $y \gg 1$ region) will be discussed in more detail in Sec. 5.3.4). The quality of the collapse of our data for both the correlation function and the structure factor is entirely comparable to the quality of collapse obtained in simulations of ordering in systems where the validity of dynamical scaling has not been questioned (see, e.g., Ref. [18] for the Ising system in 2 spatial dimensions, or Ref. [10] for the $O(3)$ vector model in 3 dimensions). In this sense, our data are consistent with the validity of the statement (a), given above.

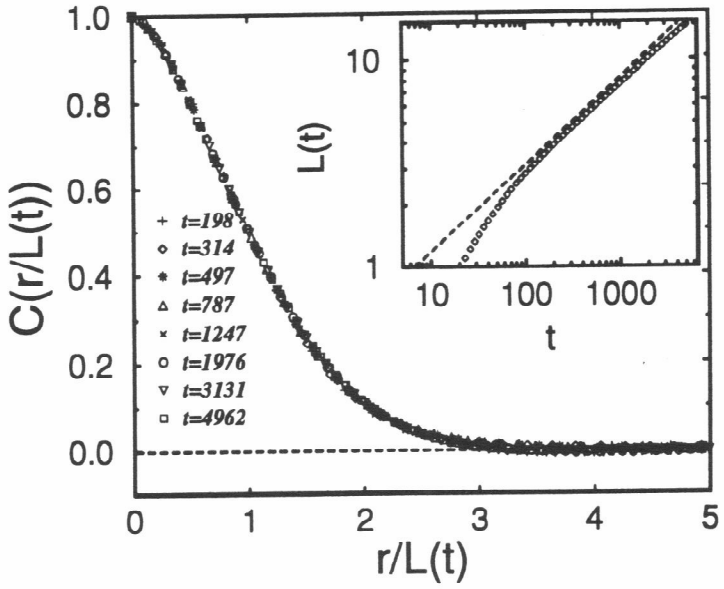

Figure 5.5: Collapse of the data for $C(r,t)$ from Fig. 5.4. Inset: time-dependence of the correlation length $L_{\rm cor}$, defined by $C(r,t)\Big|_{r=L_{\rm cor}(t)} = 1/2$.

5.3.2 Effective growth exponents for the correlation length and energy length.

We now consider the time-dependence of the correlation length and the energy density. The inset in Fig. 5.5 shows the growth of the correlation length $L_{\rm cor}(t)$. This log-log plot indicates a crossover from a non-power law growth of $L_{\rm cor}(t)$ at small t to an approximate power-law growth at $t \geq 200$, the later range of times corresponding to times where the good collapse of the correlation function is observed. The slope of the best-fitting straight line, giving the growth exponent, is $\phi_{\rm cor} = 0.41$. In Fig. 5.7, we plot the elastic free energy of the system, $\int (\partial_\alpha Q_{\beta\gamma})(\partial_\alpha Q_{\beta\gamma})\ d^2x$, as a function of time. Asymptotically, the elastic free energy decays approximately as $t^{-0.64}$, giving power-law growth for the energy length-scale $L_{\rm en}(t)$ [defined as the inverse square root of the elastic free energy] with exponent $\phi_{\rm en} = 0.32$.

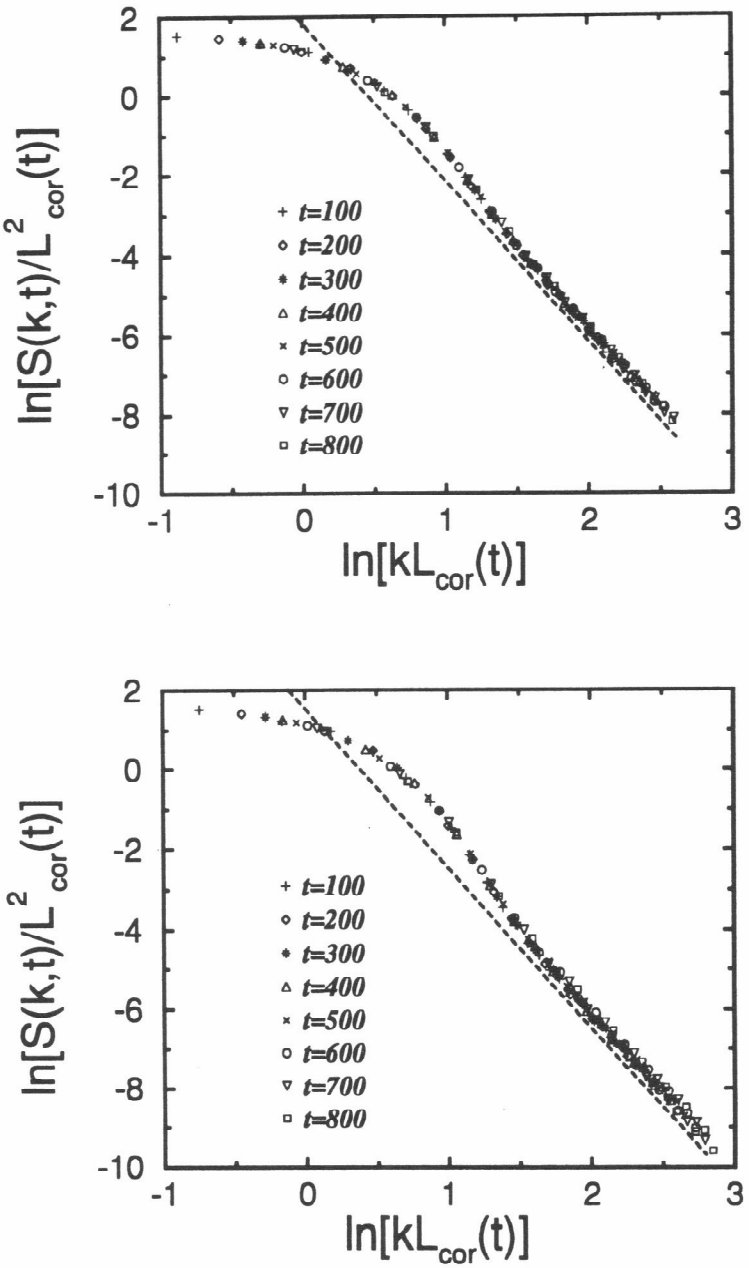

Figure 5.6: The collapsed structure factor scaling function $g(kL_{\rm cor}) = S(k,t)/L^2_{\rm cor}(t)$ for (a) uniaxial and (b) biaxial quenches. In both cases, the average was performed over 100 configurations of a 100 × 100 system, with the diffusion constant D=0.1. A straight line with slope -4 is plotted in both Fig. 5.6a and Fig. 5.6b to demonstrate the validity of the Porod law, $g(y) \sim y^{-4}$ for y large (see section III.C).

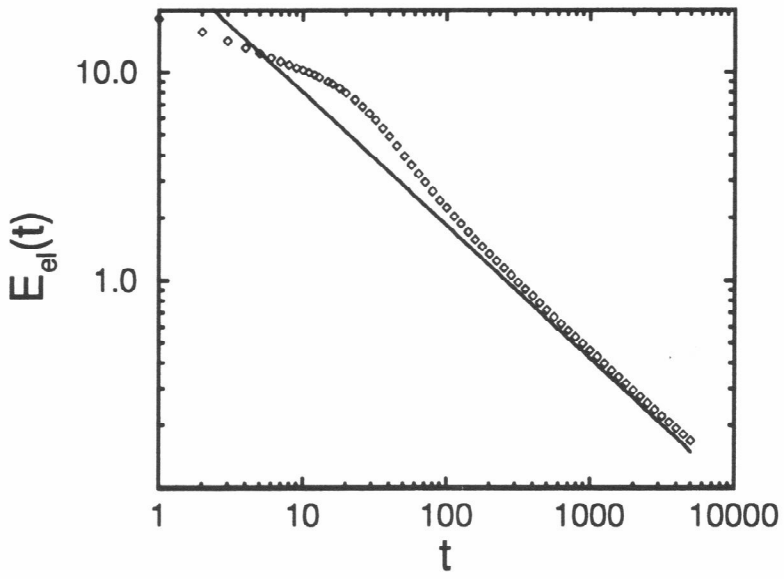

Figure 5.7: Log-log plot of the elastic free energy per cell $F(t)$ versus time t. (Averaged over 68 configurations of a 256×256 system).

To determine the value of the growth exponent for both cases in a more reliable way, we calculate the *effective growth exponent* $\hat{\phi}(t)$, defined as

$$\hat{\phi}(t) \equiv \frac{d \ln L(t)}{d \ln(t)}, \tag{5.16}$$

in the considered time range [with $L(t)$ taken to be either $L_{\rm cor}(t)$ or $L_{\rm en}(t)$]. The true (asymptotic) power-law exponent ϕ is obtained by extrapolating the effective exponent $\hat{\phi}(t)$ to very large values of t or, equivalently, to very large values of $L(t)$. We have attempted to match our data for $\hat{\phi}(t)$ on to two candidate extrapolation formulas:

$$\hat{\phi}(t) = \phi + \frac{a}{L(t)}, \tag{5.17}$$

$$\hat{\phi}(t) = \phi + \frac{A}{t}, \tag{5.18}$$

with ϕ, a and A constant. The validity of relation (5.17) would imply that

$$L(t) = -\frac{a}{\phi} + bt^{\phi} \tag{5.19}$$

throughout the considered time range, while the relation (5.18) would imply that

$$L(t) = c\,t^{\phi} \exp\,(\,-A/t) \tag{5.20}$$

(where b and c are arbitrary constants).

We find that our data for the effective growth exponents of both the correlation length and the energy length fit Eq. (5.18) significantly better than Eq. (5.17) [see Figs. 5.8 and 5.9]. As $t \gg 1$ in the considered time range, we can rewrite Eq. (5.20) as

$$L(t) \approx c\,t^{\phi}\left(1 - \frac{A}{t}\right) = c\,t^{\phi} - cAt^{\phi-1} \tag{5.21}$$

which (by analogy with critical phenomena having a "critical point" at $t = \infty$) corresponds to a power-law behavior together with the leading *analytic correction*. The extrapolation formula (5.18) is thus perhaps more natural than (5.17).

The effective exponents $\hat{\phi}_{\rm cor}(t)$ and $\hat{\phi}_{\rm en}(t)$ are plotted as a function of $1/t$ in Fig. 5.8 (for the biaxial quench case) and in Fig. 5.10 (for the uniaxial quench case). The figures show a sharp transition in the rate of change of both effective exponents at the time $t \simeq 2000$. (The transition is less sharp in the uniaxial quench data, because the average was performed over a smaller number of configurations than for the biaxial case). We found that in a system of smaller size, i.e. 100×100, a similar transition occurred at a lower value of t [and therefore $L(t)$], indicating a connection between this transition and finite-size effects. At the same time, increasing the diffusion constant D in the CDS scheme to values larger then $D = 0.1$ seemed partially to suppress the transition, indicating that the rapid lowering of the growth exponents may be due to the onset of freezing. [The likelihood of freezing at late times was observed to depend on the value of the diffusion constant in CDS simulations for scalar systems [18])]. To determine the asymptotic growth exponents we therefore used data only from the time range $200 < t < 2000$.

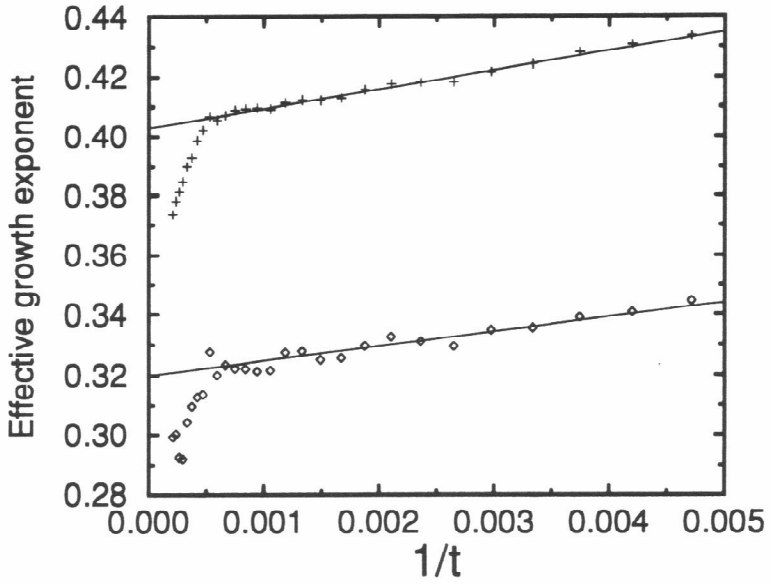

Figure 5.8: Effective growth exponents for the correlation length (upper curve) and the energy length (lower curve) in the biaxial quench case, plotted to fit the extrapolation formula (15b).

In the biaxial-quench case, the extrapolation formula (5.18) yields (see Fig. 5.8) the asymptotic exponent values $\phi_{\rm cor} = 0.403 \pm 0.003$ for the correlation length, and $\phi_{\rm en} = 0.320 \pm 0.005$ for the energy length. A similar analysis for the uniaxial quench (see Fig. 5.10) gives $\phi_{\rm cor} = 0.407 \pm 0.005$ and $\phi_{\rm en} = 0.325 \pm 0.007$, consistent with the biaxial values. Statement (b) in Sec. 5.3.1 (i.e., the presence of a *single* characteristic length scale) is therefore violated in the considered time range. We are thus confronted with two questions: (i) why is $\phi_{\rm en}$ significantly lower than $\phi_{\rm cor}$; and (ii) why are both $\phi_{\rm cor}$ and $\phi_{\rm en}$ different from the value 0.5, suggested by the diffusive character of the equation of motion (5.1) and by scaling arguments [19]? The second question can be most naturally addressed by investigating in detail the process of annihilation of a pair of defects, as will be discussed in Sec. 5.5.1. The first question is addressed below. First, however, we need to discuss in some detail the form of the structure

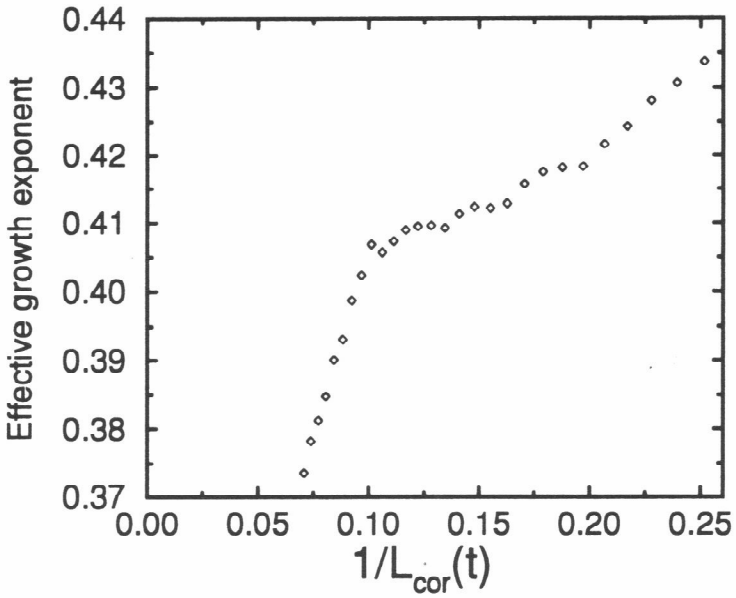

Figure 5.9: Effective growth exponent $\hat{\phi}_{\rm cor}(t)$ for the correlation length in the biaxial case, plotted to fit the extrapolation formula (15a).

factor scaling function $g(y)$.

5.3.3 The "tail" of the structure factor

We see in Figs. 5.6a and 5.6b that the function $g(y)$, obtained by collapsing the structure factor using the correlation length [see Eq. (5.15)], decays asymptotically as y^{-4} at large y. This is readily understood by generalizing the arguments leading to the "Porod law tail," i.e., $g(y) \sim y^{-(N+d)}$ in the case of the $O(N)$ vector model in d dimensions [20, 21]. For $y = kL_{\rm cor}(t) \gg 1$, the structure factor $S(k,t)$ probes the order-parameter configurations at length-scale $1/k = L_{\rm cor}(t)/y$ much smaller than the separation between defects, which is of the order of $L_{\rm cor}(t)$ (see the note [28]). Substantial variations of the order parameter over length-scale $= L_{\rm cor}(t)/y$ occur only in the vicinity of the defect cores, and are not related to inter-defect correlations. It is therefore possible to calculate the value of $S(k,t)$ for $kL(t) \gg 1$ from the order-

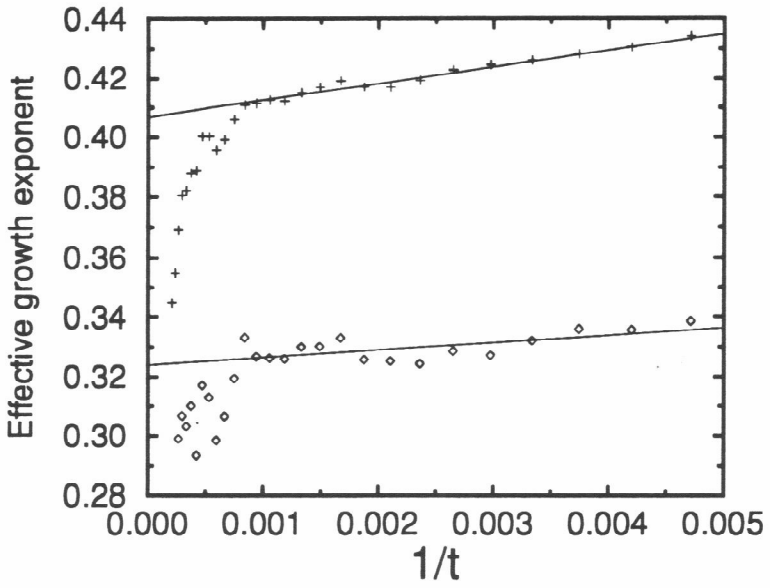

Figure 5.10: Effective growth exponents for the correlation length (upper curve) and energy length (lower curve) in the uniaxial quench case, plotted to fit the extrapolation formula (15b). The system size is 256×256, and averaging was performed over 35 configurations.

parameter configuration close to the core of an isolated defect. This implies that

$$S(k,t) = \rho_{\rm def}(t)\, u(k) \qquad (\text{for } kL_{\rm cor}(t) \gg 1), \tag{5.22}$$

where $\rho_{\rm def}$ is the density of defects in the system, and $u(k)$ is a function of k only. Let us assume for now [22] that the separation between defects scales as the correlation length $L_{\rm cor}(t)$, so that $\rho_{\rm def} \propto L_{\rm cor}(t)^{-(d-s)}$, where s is the dimensionality of the defect. Then the validity of the scaling form (5.15) implies that

$$g(y) = A\, y^{-(d+(d-s))}, \tag{5.23}$$

i.e. the scaling function $g(y)$ decays asymptotically as a power law, with the exponent given by the sum of the dimension of space d and the *co-dimension* of the defect $(d-s)$. In the case of the d-dimensional $O(N)$ vector model, the dimensionality of the defects

is $s = d - N$, and we recover the result $g(y) \propto y^{-(d+N)}$ of [20, 21]. In our $2D$ nematic system, which has point defects, the co-dimension is $2 - 0 = 2$, yielding $g(y) \sim y^{-4}$, in agreement with the results of our simulations (see Figs. 5.6a and 5.6b).

It is of interest to note that at lower values of y (i.e., values less than $y = kL_{\rm cor}(t) \simeq 5$), the scaling functions in Figs. 5.6 deviate from the y^{-4} law, seeming instead to decay with a *higher* power of y. Similar behavior was observed in simulations [4] and experiments [9] (see also Ref. [6]) of phase ordering in 3-*dimensional* uniaxial nematics, where a final Porod-law decay-exponent of 5 (corresponding to *line* defects in 3 dimensions) was approached *from above*. It was speculated that the transient value higher than 5 was due to the influence of point defects (which in 3 dimensions give a Porod-law exponent of 6); in our *2-dimensional* simulation, however, no defects (even transient) that would contribute a Porod-law exponent higher then 4 occur, and it must therefore be concluded that the faster decay of $g(y)$ at intermediate values of y is associated with inter-defect correlations. This is further indicated by the fact that deviations from the asymptotic Porod law start to occur at values of $y \simeq 5$ (see Figs. 5.6), corresponding to correlations probed on the scale of $\frac{2\pi}{y} L_{\rm cor}(t) \simeq L_{\rm cor}(t)$, i.e., the order of the inter-defect distance.

5.3.4 The energy-length growth exponent

We are now in a position to discuss why it is that the growth exponent $\phi_{\rm en}$ was found to be significantly lower than $\phi_{\rm cor}$ in our numerical results. To do this, we derive a formula relating the instantaneous exponents $\hat{\phi}_{\rm en}(t)$ and $\hat{\phi}_{\rm cor}(t)$. A similar argument was given in a qualitative form for the $O(2)$ vector order parameter case in Ref. [21].

We start by noting that

$$E_{\rm el} = \int d^2x \Big(\partial_\alpha Q_{\beta\gamma}\Big)\Big(\partial_\alpha Q_{\beta\gamma}\Big) = \int d^2k\, k^2 S(k,t) = \int d^2k \left(kL_{\rm cor}(t)\right)^2 g\Big(kL_{\rm cor}(t)\Big)\,, \tag{5.24}$$

were we used Statement (a) of the scaling hypothesis in the form of Eq. (5.15). Next, we use the Porod law form, Eq. (5.23), for $g(y)$ in the range of distances

$L_{\rm cor}(t) \geq r \geq \xi$, where ξ is the core size of the defects. In the range of distances between $L_{\rm cor}(t)$ and the system size, $g(y)$ has a weaker dependence on y (except for a narrow range, discussed in the previous subsection), and its contribution is not important for large $L_{\rm cor}(t)$. By integrating Eq. (5.24) from ξ to $L(t)$, we obtain the asymptotic [large $L_{\rm cor}(t)$] expression for the free energy

$$E_{\rm el} \propto L_{\rm cor}(t)^{-2} \ln \left(L_{\rm cor}(t)/\xi \right) . \tag{5.25}$$

This implies that

$$\frac{d(\ln E_{\rm el})}{d(\ln t)} = \frac{d(\ln L_{\rm cor}(t))}{d(\ln t)} \frac{d(\ln E_{\rm el})}{d(\ln L_{\rm cor})} = \hat{\phi}_{\rm cor}(t) \Big(-2 + \frac{1}{\ln(L_{\rm cor}/\xi)} \Big) . \tag{5.26}$$

Therefore, the effective growth exponent $\hat{\phi}_{\rm en}(t)$ for the characteristic energy length is depressed with respect to the correlation length exponent $\hat{\phi}_{\rm cor}(t)$, according to

$$\hat{\phi}_{\rm en}(t) \simeq \hat{\phi}_{\rm cor}(t) - \frac{\hat{\phi}_{\rm cor}(t)}{2 \ln \left(L_{\rm cor}(t)/\xi \right)} . \tag{5.27}$$

In Fig. 5.11 we compare the prediction of Eq. (5.27) to the measured value (see Fig. 4) of the effective exponent $\hat{\phi}_{\rm en}(t)$, for the plausible value of the core size $\xi = 0.5$ lattice spacings (direct inspection of the order parameter magnitudes in the vicinity of defect locations in our simulation shows that the core size is less than, but of the order of, one lattice spacing). Considering the crudeness of the argument leading to (5.27), the agreement of Eq. 5.27 with our data is quite satisfactory.

5.4 Properties of topological defects in uniaxial and biaxial nematics

5.4.1 Topological classification of nematic defects

Certain features of the late stages of phase ordering may be understood in terms of the properties of topological defects present in the system [25]: the exponent and amplitude of the asymptotic power-law decay of the structure factor can be calculated from the configuration of the order parameter around a single defect [20]; in

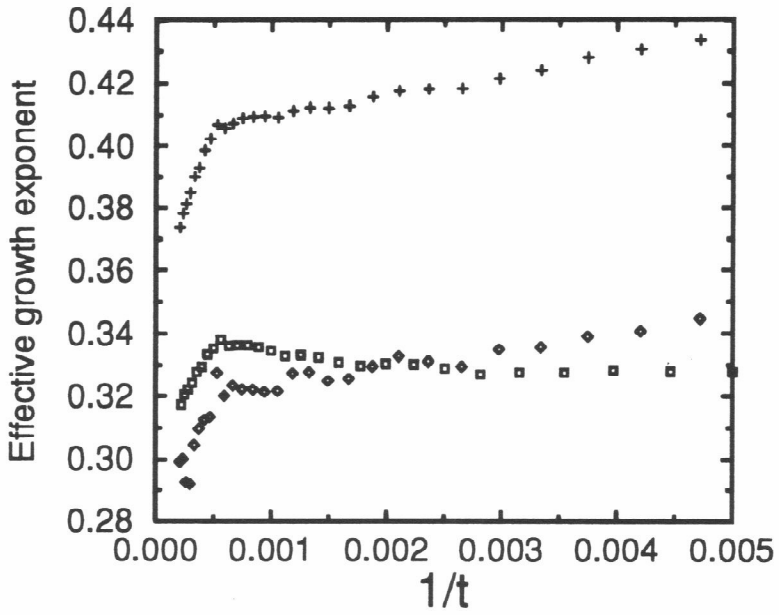

Figure 5.11: Comparison of the measured values of the energy length growth exponent $\hat{\phi}_{\rm en}(t)$ (shown as $\diamond$) to the values predicted by formula (23) (shown as squares); the measured values of the correlation length growth exponent $\hat{\phi}_{\rm cor}(t)$, used in formula (23), are shown as crosses (+, upper curve).

systems for which dynamical scaling holds, the time-dependent characteristic length-scale is given by the separation of defects; and logarithmic corrections to power-law scaling of the average defect-separation can be attributed to the form of the inter-defect forces [12]. It is therefore important to understand in detail the properties of topological defects in the system at hand. In this subsection, we briefly review the main consequences of the classification of topologically stable defects in uniaxial and biaxial nematics [13] (see Chapter 3 for a more complete discussion). In SubSec. 5.4.3 we illustrate these consequences with data from our simulation. The time evolution of the number densities of defects during phase ordering in our system will be analyzed in detail in Sec. 5.5.

For the unambiguous topological classification of order-parameter configuration,

it is necessary that the invariants constructed from the order parameter avoid certain values. In the $O(N)$ vector model, this amounts to avoiding zeros in the magnitude of the vector. In the context of the nematic order parameter, it is furthermore necessary that the order parameter magnitudes x and y (defined in Sec. 5.2) are restricted to lie either in the region $x > y$ ["needle-like" ordering, Fig. (5.3a] or in the region $x < y$ ["discotic" ordering, Fig. (5.3]. In order to develop the topological classification, it is sufficient to impose the condition that throughout the system the values of the order parameter magnitudes x and y are appropriate constants. What remain are orientational degrees of freedom, two for the uniaxial case (as specified by a 3-dimensional "headless" unit vector, i.e., the director) and three for the biaxial case. In our simulations, we ensure the applicability of the topological classification, even at the earliest stages after the quench, as discussed at the end of Sec. 5.2.

We first discuss defects in the uniaxial nematic. Consider the order-parameter configuration in a 2D system in which the director rotates by 360° around a central point (Fig. 5.12a). Such a configuration is singular (in the sense that the free energy density diverges at its center), but it is not *topologically stable*: by continuously rotating the director out of the plane (i.e., by "escaping into the third dimension") we can arrive at the nonsingular (i.e., finite free energy density) configuration, as shown in Fig. 5.12b. The singular configuration in Fig. 5.13 (in which the director rotates by 180°) is, however, topologically stable: in the process of attempting to escape into the third dimension, an even more singular configuration with a (semi)infinite line defect would be generated. More generally, any configuration in which the director rotates by an even multiple of 180° can be continuously deformed into the trivial configuration, shown in Fig. 5.12b, in contrast with configurations having a rotation of an odd multiple of 180°, which can be deformed into the configuration in Fig. 5.13. Note, in particular, that configurations with rotations of $+180°$ (clockwise) and $-180°$ (counterclockwise) can be deformed into each other. Thus, for the 2D uniaxial nematic system there exists only one class of topologically stable point defect, exemplified by the order parameter configuration shown in Fig. 5.13. (This class contains all defects

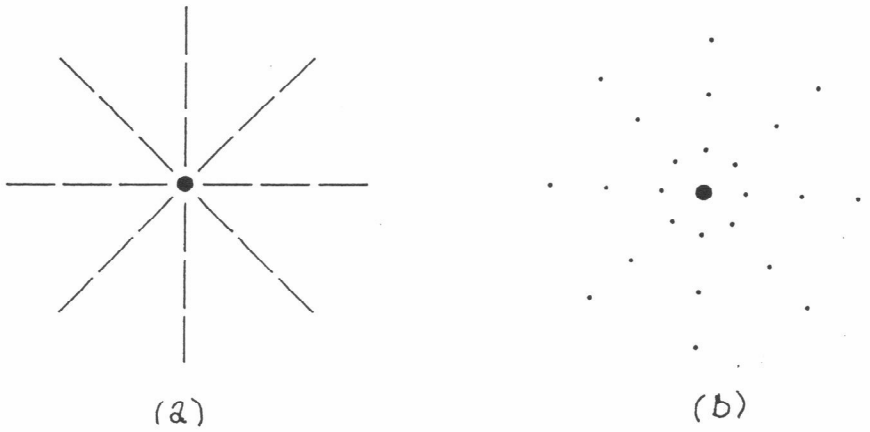

Figure 5.12: (a) A configuration of the director corresponding to the 360° defect in a uniaxial nematic. (b) By rotating the director at each location out of the page, one can smoothly deform the configuration in Fig. 11a to the defect-free configuration in Fig. 11b, with the director everywhere perpendicular to the page.

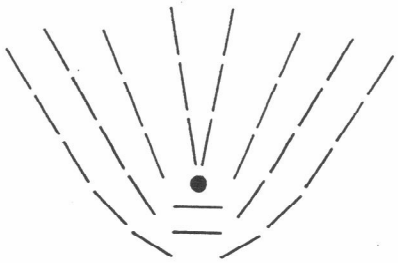

Figure 5.13: A configuration of the director corresponding to the 180° defect in a uniaxial nematic. An attempt to escape from such a configuration by rotating the director at each location out of the page inevitably results in a singular line extending from the defect center to infinity, separating regions where the director rotates out of the page in opposing directions.

obtainable by continuous distortions, including those in which the director is rotated out of the plane.)

The combination law for two stable defects is also readily obtained: colliding two $\pm 180°$ configurations results in a configuration with either 360° or 0° rotation, both of which are topologically trivial. Therefore, any two stable defects can mutually annihilate upon colliding. In more formal language, the properties discussed above are a consequence of the fact that the first homotopy group of the uniaxial nematic order-parameter space is the 2-element group $Z_2 = \left[\{0,1\} \text{ under addition modulo } 2\right]$. The elements 0 and 1 correspond to the topologically trivial class of configurations, and to the stable defect class, respectively. The defects combine according to a law given by the group operation $1 + 1 = 0$.

Next, we discuss defects in *biaxial* nematics, for which the situation is more complicated. Here, the first homotopy group of the order-parameter space Π_1 (giving the classification of point defects in a 2D system) is the non-Abelian 8 element group of quaternions, which can be represented as

$$\Pi_1 = \{1, -1, i\sigma_x, -i\sigma_x, i\sigma_y, -i\sigma_y, i\sigma_z, -i\sigma_z\}\ , \tag{5.28}$$

where σ_k are the Pauli matrices, and the group operation corresponds to matrix multiplication. For a non-Abelian Π_1, the classes of topologically nonequivalent defects are given by the *conjugacy classes* of Π_1 (see, e.g., [13] for a detailed discussion). The quaternion group Eq. (5.28) has 5 conjugacy classes:

$$C_0 = \{1\}, \tag{5.29}$$

$$\overline{C}_0 = \{-1\}, \tag{5.30}$$

$$C_x = \{i\sigma_x, -i\sigma_x\}, \tag{5.31}$$

$$C_y = \{i\sigma_y, -i\sigma_y\}, \tag{5.32}$$

$$C_z = \{i\sigma_z, -i\sigma_z\}. \tag{5.33}$$

Thus there is a topologically trivial defect class (C_0), and 4 nontrivial defect classes ($\overline{C}_0$,C_x,C_y,C_z). These are characterized by the winding numbers of the uniaxial axis

classes in Eq. (5.4.1), were observed experimentally in a biaxial nematic; their combination laws were found to be in agreement with those in Table I. We are not aware of any published experimental work on defects in effectively two-dimensional biaxial nematics.

5.4.2 Defect-finding algorithms

To keep track of the evolution of the large populations of defects present during phase ordering (and to distinguish the 4 species of defect in biaxial nematics), an effective defect-finding algorithm based on the topological properties of the defects is needed. Before illustrating the defect properties discussed above (as we do in SubSec. 5.4.3) , we present the defect-finding algorithms used in our simulation. This can also serve to illuminate further the topological classification scheme. The present subsection may be skipped by the reader interested primarily in the results without impairing the understanding of the remainder of the chapter.

Consider first the case of the uniaxial nematic. The order-parameter coset space is a sphere with antipodal points identified (reflecting the inversion symmetry of the director), i.e., the projective plane RP_2. If we trace a loop around the center of any topologically unstable singular configuration (eg., as in Fig. 5.12a), we generate a *contractible* loop in the order parameter space (Fig. 5.14a). In the case of a topologically stable configuration (eg., Fig. 5.13), we generate a *non-contractible* loop in the projective plane (Fig. 5.14b), connecting two antipodal points on the sphere. Thus, we arrive at the following algorithm for deciding whether a (uniaxial) stable defect is located inside the region spanned by the cells with coordinates (x, y), $(x + 1, y)$, $(x+1, y+1)$, $(x, y+1)$: we find the uniaxial direction in the cell (x, y) and choose as our starting point one of its intersections with the order-parameter sphere (Fig. 5.15). The uniaxial direction in the cell $(x+1, y)$ has two intersections with the-order parameter sphere; we choose the point that is *closer* to the starting point as the next point of the loop in the order-parameter space. This amounts to assuming that the new uniaxial direction was reached by rotating through the smallest possible angle, so as

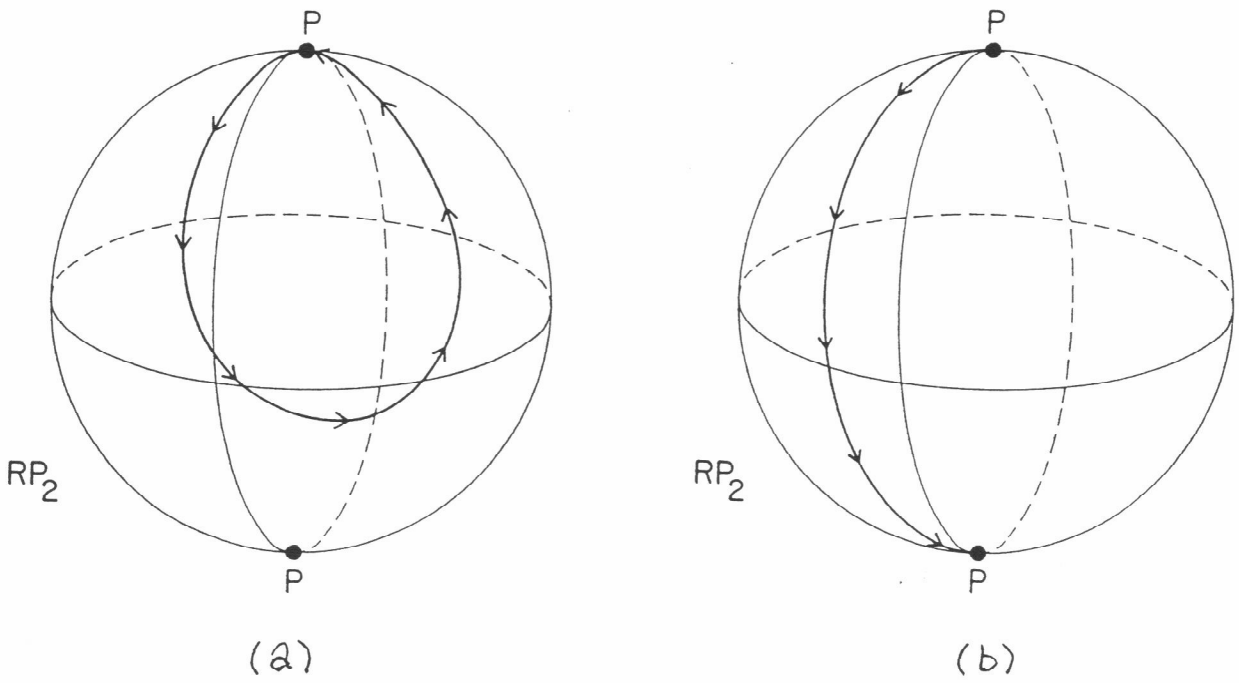

Figure 5.14: Contractible (a) and non-contractible (b) loops connecting two identical points (P and P') in the uniaxial nematic order parameter space RP_2.

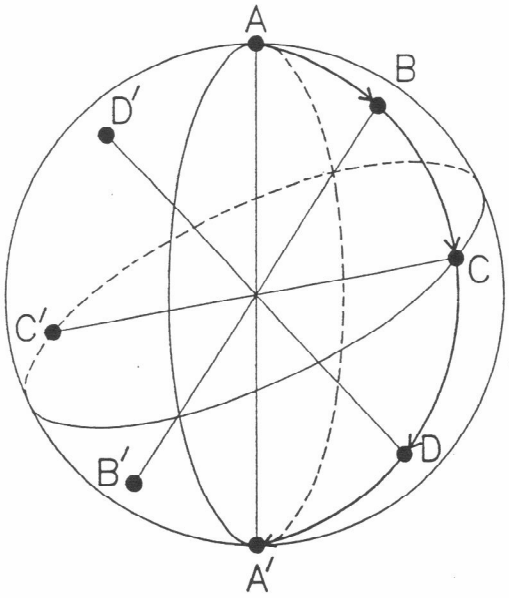

Figure 5.15: The algorithm for finding defects in a uniaxial nematic (see Sec. 5.4.2 details). The diameters AA', BB', CC', DD' correspond to the uniaxial directions of the order parameter in cells $(x, y), (x+1, y), (x+1, y+1), (x, y+1)$, respectively.

to minimize the cost in free energy. We continue with the cells $(x+1, y+1)$, $(x, y+1)$, again choosing the point on the order-parameter sphere closer to the previous point. We close the path by again looking at the two intersection points in the cell (x, y): if the original starting point is closer to the point assigned to the cell $(x, y+1)$ then we classify the configuration as not topologically stable; if the antipodal point is closer then we classify the configuration as having a stable defect located at the intersection of the cell boundaries. In a previous work on phase ordering in uniaxial nematics [5], vortices were sought by considering whether the total angle of rotation of the uniaxial direction projected on to one of the three perpendicular planes was 180°. For a configuration in which the director in all cells lies in one plane, as in the case of an isolated defect (as in Fig. 5.12), the two algorithms are equivalent; for other configurations, however, the "projection" algorithm can be unreliable. We find that our "topological" algorithm can consistently identify all defects, even when the the interdefect separation is of the order of one lattice spacing.

For biaxial nematics, we can distinguish the three 180° defect classes by applying the uniaxial algorithm twice, once to the uniaxial direction $\mathbf{u}$ and once to the biaxial direction $\mathbf{b}$: e.g., the C_y defect will give a $\mathbf{u}$-loop that returns to the starting point, and a $\mathbf{b}$-loop that ends at the antipodal point. The 360° defect (class $\overline{C}_0$) cannot be found using this algorithm. This is a consequence of the fact that the biaxial nematic order parameter coset space is not simply a direct product of two projective planes. Thus, for this case, we use the "projection" algorithm on a 4×4 array of cells: if the total rotation of the projection (on at least *two* planes) of two of the $\mathbf{u}$, $\mathbf{b}$, and $\mathbf{u} \times \mathbf{b}$ directions in the 12 boundary cells is $\pm 360°$, *and* if no 180° defects are found inside the 4×4 array, then we identify the center of the array as a $\overline{C}_0$ defect (see Fig. 5.16). Note that to consider a 2×2 array would be inadequate because the total rotation in a 4-cell path is, by definition, at most 180°; a 3×3 array cannot be used, because the 360° rotation is in that case tied to the existence of two 180° defects inside the array. The algorithm that we use for finding the $\overline{C}_0$ defect is thus less robust than that which we use for finding the other defect types. As we shall see in the next

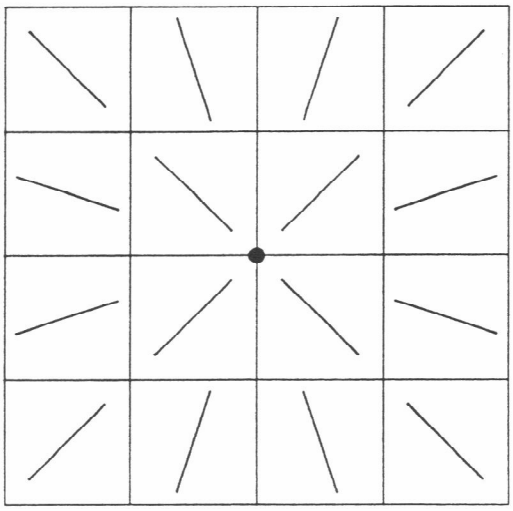

Figure 5.16: A typical configuration of the uniaxial or biaxial direction of the order parameter in the 4×4 array with a $\overline{C}_0$ defect in the center. Notice that no C_x, C_y, or C_z defects are presents in the array.

section, however, the $\overline{C}_0$ defect is present at late times only in very small numbers, and its influence is not important for our primary conclusions.

5.4.3 Results illustrating the topological classification scheme

We now illustrate the properties of defects in uniaxial and biaxial nematics that we discussed in SubSec. 5.4.1 using results from our simulation. Defects in nematic films can be observed experimentally via birefringence patterns in light transmitted through films situated between crossed polarizers (i.e., Schlieren patterns). The intensity of transmitted light is minimal when the projection of the director on to the polarization plane is parallel to the transmission axis of either polarizer; the 180° (resp. 360°) defects are therefore identified as intersections of two (resp. four) dark brushes in the transmitted pattern [23]. In Figs. 5.17a-c, we show the Schlieren patterns obtained for configurations generated in our simulations at a sequence of times after a uniaxial quench [24]. As these figures show, the process of ordering occurs through the mutual annihilation of the numerous 180° defects.

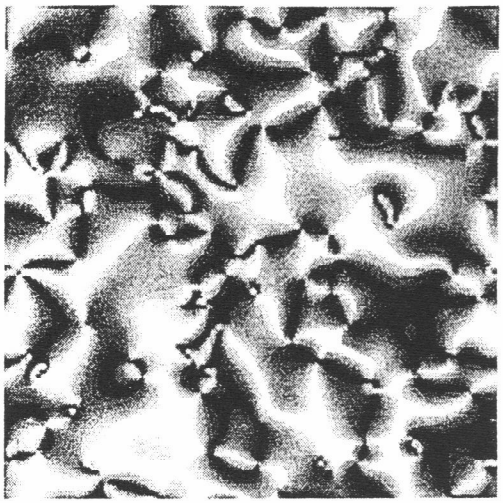

a) $t = 500$

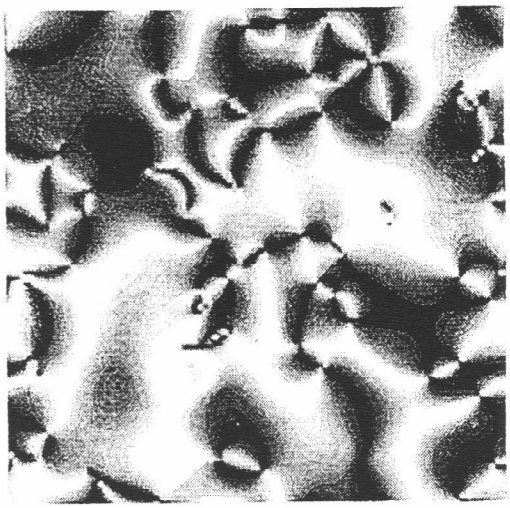

b) $t = 1000$

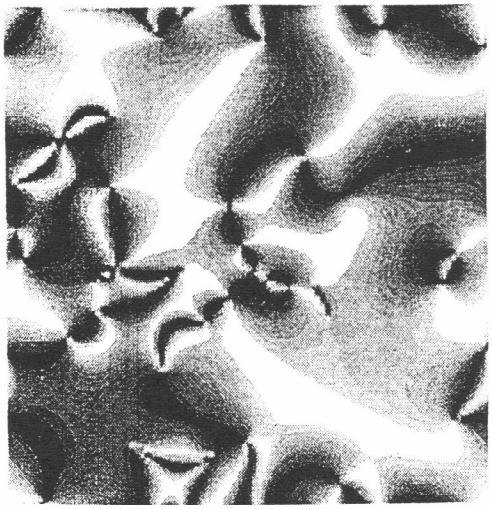

c) $t = 2000$

Figure 5.17: Intensity of light transmitted through a uniaxial nematic film situated between crossed polarizers (the Schlieren pattern). We show a system of size 100×100 at times $t = 500$, $t = 1000$, and $t = 2000$ after the quench. The defects appear in the pictures as the intersections of two bright and two dark lines.

In Figs. 5.18a-e, we exhibit the locations of defects, found using the defect-finding algorithms discussed above, in a typical sequence of configurations following a biaxial quench in a small system. Defects from each of the four topologically stable classes are present in the system. The observed two-defect events confirm the topological combination laws given in Table I (as described in the captions to Figs. 5.18). Occasionally, "many-defect" events, where a number of neighboring defects interact in a way not uniquely separable into two-defect events, are observed; the frequency of these events can be decreased by reducing the diffusion constant in the CDS map to values below $D = 0.1$.

It can be seen from Table I that the *defect number parities* p_1, p_2 and p_3, defined by

$$p_1 = (n_x + n_y) \bmod 2, \tag{5.34}$$

$$p_2 = (n_y + n_z) \bmod 2, \tag{5.35}$$

$$p_3 = (n_x + n_z) \bmod 2 \tag{5.36}$$

are conserved during all reactions amongst defects. Here n_x, n_y and n_z respectively denote the number of defects from classes C_x, C_y and C_z; as $(p_1 + p_2 + p_3) \bmod 2 = 0$, only two of the 3 parities are independent. In our simulations the parities, Eqs. (5.4.3), were observed to be conserved in all reactions, regardless of the number of participating defects. In addition, the parities obtained from the *total* numbers of defects present in the whole system must be *even*, as we have adopted periodic boundary conditions. The reason for this is that opposite edges of the boundary of the system map on to identical (closed) curves in the order parameter coset space, but are traversed in opposite senses; the loop consisting of the boundary of the system therefore maps into a contractible loop in the coset space. Thus, the configuration of the system, as a whole, is topologically trivial, which for the nematic implies that the parities, Eqs. (5.4.3), are even. This property of the global parities is confirmed in Table II, which gives the numbers of C_x ,C_y and C_z defects founds during a typical run in a system of size 256×256.

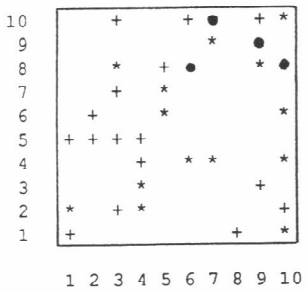

a) $t = 17$

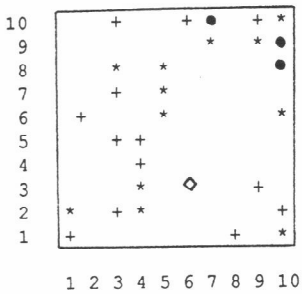

b) $t = 18$

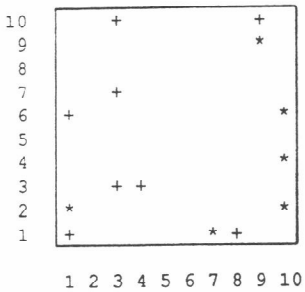

c) $t = 44$

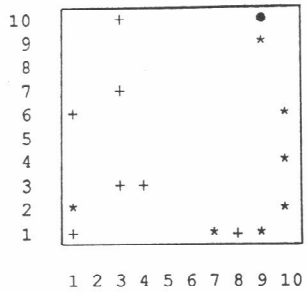

d) $t = 45$

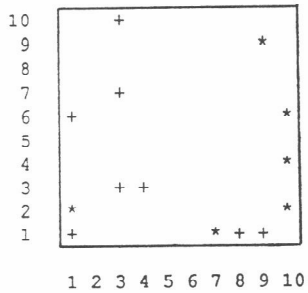

e) $t = 46$

Figure 5.18: Defect configurations in a biaxial system of size 10×10 at specified times since the quench. The symbols $\bullet$, *, + and $\diamond$ correspond to defects from classes C_x, C_y, C_z and $\overline{C}_0$, respectively. In the following description of the figures, we refer to the horizontal coordinate as x, and to the vertical coordinate as y, both starting from the left bottom corner of each figure (thus x,$y = 1, ..., 10$). Note that the boundary conditions are periodic. The diffusion constant value of D=0.1 was used in this simulation. (a) The configuration at t=17 time steps since the quench. The system contains 4 type C_x defects, 16 type C_y defects, and 14 type C_z defects. (b) The configuration at the next time step (t=18). The C_z defect at $(x, y) = (1, 5)$ annihilated with the neighboring C_z defect. Two C_y defects in the center region combined to produce a $\overline{C}_0$ defect. The C_z defect at $(x, y) = (5, 8)$ and the C_x defect at $(x, y) = (6, 8)$ combined to a C_y defect. (c) The configuration at t=44. All the C_x defects have decayed from the system. (d) At the next time step (t=45), the C_z defect at $(x, y) = (9, 10)$ disintegrates into the C_x defect and the C_y defect at the neighboring site $(x, y) = (9, 1)$. (e) Configuration at the next time step (t=46). The C_x defect immediately re-combines with the C_y defect at $(x, y) = (9, 1)$. The net result of the last two reactions is a C_x — mediated jump of the C_z defect from the site $(x, y) = (9, 10)$ to the neighboring site $(x, y) = (9, 1)$. The C_z defect at $(x, y) = (9, 1)$ undergoes annihilation with the C_z defect at $(x, y) = (8, 1)$ at a later time.

Table 5.2: Numbers of defects in the C_x, C_y, C_z and $\overline{C}_0$ classes at time t after the quench to the biaxial nematic phase in a 256×256 system (the value of $D = 0.1$ was used in the simulation).

t	$n(C_x)$	$n(C_y)$	$n(C_z)$	$n(\overline{C}_0)$[1]
0	14925	11503	15039	0
5	10093	12787	14577	1
10	6393	12949	12141	5
20	2758	10542	8866	13
40	589	6157	5357	14
100	25	2495	2359	24
200	1	1439	1235	9
399	2	840	676	3
795	0	514	394	7
1585	0	326	244	5
2819	2	200	146	1
5012	0	130	116	6

5.5 Evolution of the defect populations

In this section, we present results for the time evolution of the total number of defects in each of the topologically inequivalent defect classes.

5.5.1 Results for the uniaxial quench; growth law for the separation between defects.

In uniaxial nematics there is only one class of stable defects. In Fig. 5.19 we show the number of such defects as a function of time since the uniaxial quench, in a system of size 256×256, averaged over 35 sets of initial configurations. In the inset we

[1]The number of $\overline{C}_0$ defects which can be found at early times is reduced due to the high density of the 180° defects—see Section 5.4.3.

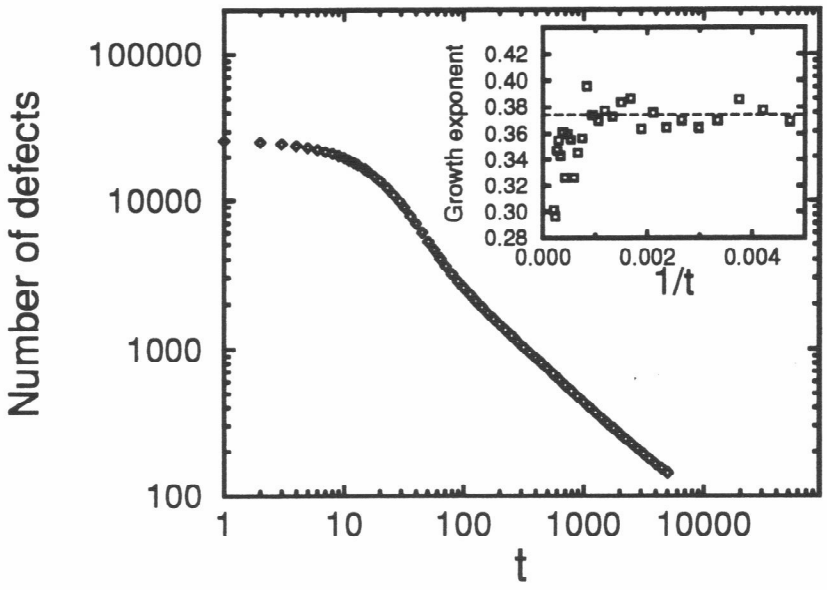

Figure 5.19: Log-log plot of the number of defects in a uniaxial system (size 256×256, averaged over 35 configurations) as a function of time t since the quench. Inset: the effective growth exponent $\hat{\phi}_{\rm def}(t)$ of the average separation between the defects, plotted to fit the extrapolation formula (15b).

plot the effective growth exponent $\phi_{\rm def}(t)$ for the average inter-defect distance $L_{\rm def}(t)$ versus $1/t$, in the interval where the correlation function collapses. The intercept with the $\hat{\phi}_{\rm def}$–axis gives the asymptotic growth exponent $\phi_{\rm def} = 0.374 \pm 0.005$ (see formula (5.18) and the discussion in Sec. 5.3.2). The growth exponent obtained from the number of defects differs from the exponents obtained from the correlation function and the energy density (see Sec. 5.3.1), giving another indication of the violation of Statement (b) of the dynamical scaling hypothesis, at least over the range of times studied.

It has been found in all published numerical studies of phase ordering in 2D systems with point defects (e.g., Refs. [2, 4, 5, 10]) that both the correlation length and (where studied) the separation of defects grow *more slowly* than the $t^{1/2}$ power growth law that is suggested by dimensional analysis [19]. This issue was addressed

theoretically for the $O(2)$ vector model in Ref. [12], by starting from the equation of motion for an isolated defect-antidefect pair, which follows from equating the attractive and frictional forces acting on each defect. The elastic attractive force was taken to be $F_{\rm at} \propto -1/\mathcal{D}$, where $\mathcal{D}$ is the separation of the defect pair. The frictional force was taken to be $F_{\rm fr} \propto v \ln(R/\xi)$, where R is the size of a defect, ξ is the size of its core, and $v = \frac{1}{2}\frac{d\mathcal{D}}{dt}$ is its velocity. For an isolated defect-antidefect pair, $R \sim \mathcal{D}$. By equating $F_{\rm at}$ and $F_{\rm fr}$ Yurke et al. obtained an implicit formula for the dependence of the separation $\mathcal{D}$ on the time remaining before annihilation τ:

$$\mathcal{D}(\tau) = \text{const} \times \left[\frac{\tau}{\ln\left(\mathcal{D}(\tau)/\xi\right) - 1/2}\right]^{1/2}. \tag{5.37}$$

Yurke et al. then argued that the same expressions for the elastic and frictional forces acting in an isolated defect-antidefect pair may be used in a modification of the arguments in Ref. [19] to obtain an expression, identical to Eq. (5.37), for the growth of the average separation between defects in a system undergoing phase ordering. In this scenario, τ is (up to an undetermined, but small, additive constant) the time elapsed since the quench, and $\mathcal{D}$ is the average separation of defects, $L_{\rm def}$, so that one obtains

$$L_{\rm def}(t) = \text{const} \times \left[\frac{t}{\ln\left(L_{\rm def}(t)/\xi\right) - 1/2}\right]^{1/2}. \tag{5.38}$$

Equation (5.38) implies that $L_{\rm def}$ grows asymptotically as $t^{1/2}$, but that the effective growth exponent $\hat{\phi}_{\rm def} = d\ln L_{\rm def}/d\ln t$ approaches the value $1/2$ only slowly and from below, due to the logarithmic term. It was indeed observed in the numerical simulations reported in Ref. [12] that, for both the annihilation of an isolated defect-antidefect pair and for phase ordering of a large system after a quench, $\hat{\phi}_{\rm def}(t)$ was significantly smaller than $1/2$, and tended to increase with increasing separation of defects.

It is important to recall that in the system investigated in our simulations, the 2D (uniaxial) nematic, the director can point in any direction in the 3-dimensional space, in contrast to the restriction on the order parameter of the 2D $O(2)$ vector

model to lie in the plane. The late-time features of phase ordering, however, are governed primarily by the point defects moving in 2-dimensional space, which are present in both models. For this reason, it is appropriate to compare our results to the conclusions of Ref. [12]. (We note, parenthetically, that the 2D $O(3)$ vector model does not support any topologically stable singular configurations, and it's phase ordering exhibits features [27] strongly different from the phase ordering in the 2D nematic).

Equation (5.38) implies that the effective growth exponent for the average defect separation is given by

$$\frac{d \ln L_{\rm def}(t)}{d \ln t} = \frac{t}{L_{\rm def}(t)^2} \frac{\rm const}{2 \ln \left(L_{\rm def}(t)/\xi \right)} . \tag{5.39}$$

Due to the unknown constant in Eq. (5.39), it is not possible (even with the knowledge of the core size, $\xi \simeq 0.5$ lattice spacings, from Sec. 5.3) to compare the numerical value of the effective growth exponent $\phi_{\rm def} \simeq 0.374$ in our simulation to the expression (5.39). Although Eq. (5.38) predicts an increasing effective exponent $\phi_{\rm def}(t)$, the value obtained from our data is essentially constant over the interval during which collapse of the correlation function occurs (Fig. 5.19).

A crucial assumption made in deriving Eq. (5.38) is that the average separation of the numerous defects during the phase ordering of a large system is determined solely by the forces acting in the two-defect problem. In order to address the validity of this assumption, we simulated the annihilation process of two isolated uniaxial nematic defects (see Fig. 5.20). During this simulation, we found it advantageous (in order to be able to reduce the influence of the discrete character of the lattice by averaging over multiple runs) to add a random order parameter configuration of reduced amplitude (up to 10% of the full order parameter magnitude) at each time step. We stress that this noise was added solely to obtain a meaningful averaging procedure; no pinning effects were observed in the studied time range upon eliminating the noise. The measured distance between the two defects $\mathcal{D}$ is shown in Fig. 5.21 as a function of time remaining to annihilation τ. The power law $\mathcal{D} \propto t^{0.375}$ is observed over the range

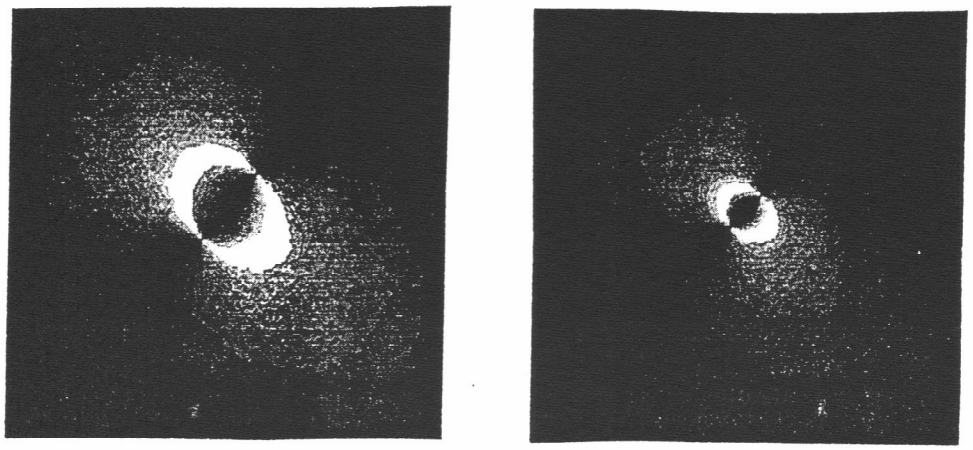

a) $\tau = 3265$ b) $\tau = 465$

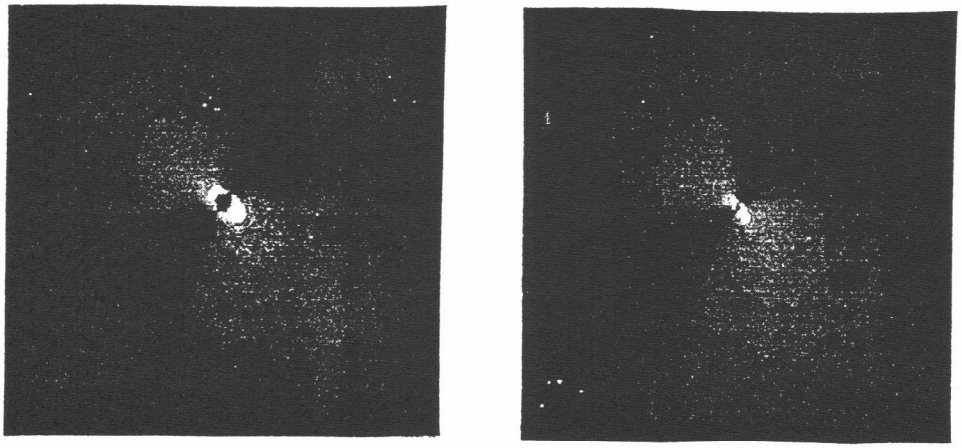

c) $\tau = 30$ d) $\tau = 0$

Figure 5.20: Schlieren patterns showing two approaching uniaxial defects at times t=3265, t=465, t=30 before annihilation, and one time step after annihilation. The system size was 100 × 100; the value of the diffusion constant was D=0.3; weak noise (10% of the order parameter magnitude) was added at each time step.

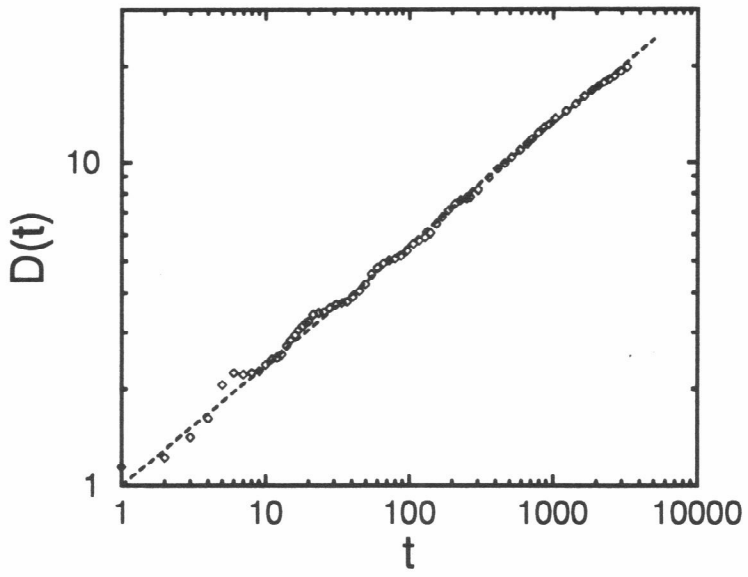

Figure 5.21: The distance $\mathcal{D}(t)$ between two annihilating uniaxial defects as a function of time t remaining till annihilation. A weak value of noise (10% of the order parameter magnitude) was used to permit averaging over 20 events. The value of the diffusion constant was D=0.3.

of distances $2 \leq \mathcal{D} \leq 10$, corresponding to the range in which the effective exponent $\phi_{\rm def} \simeq 0.375$ was observed in the phase ordering simulation (Fig. 5.19). We therefore reach the conclusion that the time-dependence of the distance between two isolated annihilating defects does indeed determine the growth-rate of the average separation between defects during phase ordering.

Around an isolated pair of uniaxial nematic defects, it is energetically advantageous for the director to lie in a single plane. The treatment of the annihilation process of two defects is then identical to the treatment for the 2D XY model case in Ref. [12](with the constant in Eq. (5.37) divided by 4, due to the change in the winding number of the defects). Our data (Fig. 5.21) do not, however, show the increase of the effective exponent $\phi_{\rm def}(t)$, with increasing $\mathcal{D}$, predicted by Eq. (5.37). This increase should be visible even in the comparatively narrow range of $\mathcal{D}$ covered in our

simulation. This we take as an indication that the forces acting on the defects in our simulation are not completely described by the forces $F_{\rm fr} \propto v \ln(\mathcal{D}/\xi)$ and $F_{\rm at} \propto 1/\mathcal{D}$, assumed in the derivation of (5.37). In particular, the influence of a weak pinning potential at the centers of the cells would become more pronounced with increasing $\mathcal{D}$, since the interaction energy of two vortices decreases with increasing distance. The presence of a pinning force would therefore tend to decrease the effective growth exponent $\phi_{\rm def}$ with increasing $\mathcal{D}$, possibly offsetting the increase of $\phi_{\rm def}$ predicted by Eq. (5.37).

It should be noted that the arguments leading to Eq. (5.39) do not make any assumptions about the correlation function – in particular, our finding that the correlation length (as defined in Sec. 5.3.1) and the average separation of defects scale in a different way ($\phi_{\rm cor} = 0.407 \pm 0.005$ versus $\phi_{\rm def} = 0.374 \pm 0.007$) does not invalidate Eq. (5.39).

We now discuss the implications of the observed inequality: $\phi_{\rm cor} > \phi_{\rm def}$. This inequality is, strictly speaking, incompatible with the collapse of the correlation function and structure factor [i.e., Statement (a) in Sec. 5.3.1]. The reason is that the *number density of defects* $\rho_{\rm def}$ appears in Porod's law, Eq. (5.22), which is valid independently of the collapse of the structure factor. The density $\rho_{\rm def}$ must decay as the (square of the) separation between defects (and not any other length, such as $L_{\rm cor}$). In order that Eq. (5.15), expressing the collapse of the structure factor, be compatible with Eq. (5.22) it is therefore necessary that the lengths $L_{\rm cor}$ and $L_{\rm def}$ have a common time-dependence. We have not been able to identify why $L_{\rm cor}$ and $L_{\rm def}$ differ. However, it is plausible that the origin of the discrepancy lies in the relevance of additional degrees of freedom beyond the defect positions.

Recall that earlier, in Sec. 5.3, we exhibited the good collapse of the correlation function and structure factor in our simulation. It is thus seen that the direct comparison of the effective growth-exponents $\phi_{\rm def}$ and $\phi_{\rm cor}$ presents a more sensitive diagnostic of the validity of dynamical scaling than do the apparent collapse of the correlation function and structure factor.

We remind the reader that the discrepancy between ϕ_{cor} and the energy length growth-exponent ϕ_{en} does *not* necessarily indicate the breakdown dynamical scaling, as we have explained in in Sec. 5.3. On the other hand, the expression for the difference between ϕ_{cor} and ϕ_{en}, Eq. (5.27), was derived in Sec. 5.3.4 under the assumption that the structure factor collapses. Given the quality of the apparent collapse and the smallness of the difference between ϕ_{cor} and ϕ_{def} we anticipate only small corrections to Eq. (5.27).

The discrepancy between the growth exponents of the correlation length and of the defect separation was recently observed (Ref. [10]) also in the the 2-dimensional $O(2)$ vector model. It is interesting to note that the results obtained in Ref. [10], $\phi_{\text{cor}} = 0.42$ and $\phi_{\text{def}} = 0.37$, are numerically very close to the results obtained by us in the nematic order parameter case.

5.5.2 Results for the biaxial quench; selection of the prevailing defect species.

In the biaxial nematic case, we monitor separately the populations of the 4 inequivalent defect classes introduced in Sec. 5.4.1 Figure 5.22 shows the results averaged over 68 initial configurations of a 256 × 256 system. Immediately following the quench, defects from the classes C_x, C_y and C_z are present in large numbers. We find that the C_x defect population decays rapidly in the initial stages of ordering, and disappears from the system at the time approximately corresponding to the onset of the regime in which there is apparent collapse of the correlation function. The C_y and C_z defects subsequently remain in the system in roughly equal numbers, and determine the properties of the asymptotic regime. The effective growth-exponent for the C_y and C_z defect separation is analyzed in Fig. 5.23 using the method described in Sec. 5.3.1; we obtain $\phi_{\text{def}} = 0.366 \pm 0.005$ and $\phi_{\text{def}} = 0.391 \pm 0.005$, respectively.

The evolution of the $\overline{C}_0$ (i.e., 360°) defect population requires further clarification. Our defect-finding algorithm (see Sec. 5.4.2) is able to identify a $\overline{C}_0$ defect within any given 4 × 4 array of cells only if there are no 180° defects within the array; at the

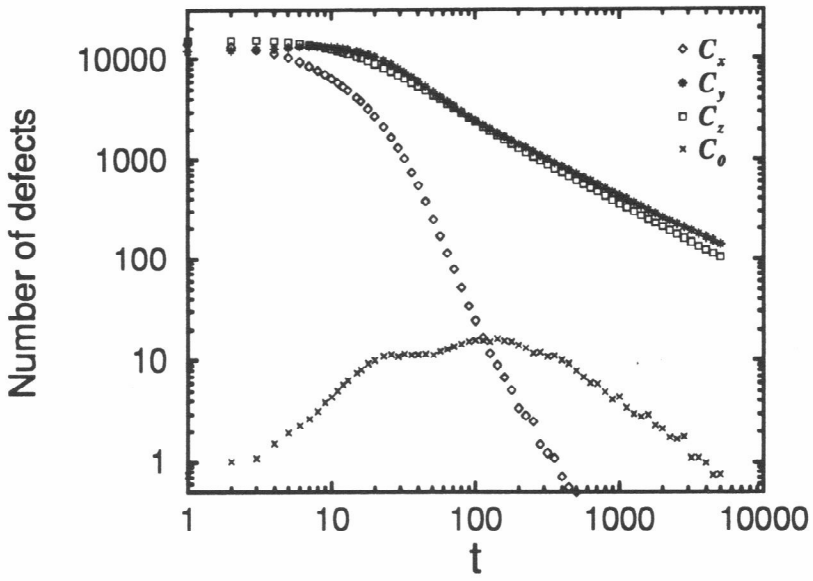

Figure 5.22: Log-log plot of the numbers of the C_x, C_y, C_z and $\overline{C}_0$ defects as a function of time since the biaxial quench. (Averaged over 68 configurations of a 256×256 system)

initial stages of ordering, however, very few such arrays exist in the system, due to the high density of C_x, C_y and C_z defects. Accordingly, the detected number of $\overline{C}_0$ is very small at early times after the quench (see Fig. 5.22), and becomes a reliable measure of the proportion of 360° defects in a real system only at late times, when the separation between 180° defects is much larger then the lattice spacing. A more meaningful quantity, perhaps, is the ratio of the number of $\overline{C}_0$ defects to the number of the "available" 4×4 arrays; this ratio is plotted in Fig. 5.24. The population of $\overline{C}_0$ defects appears to decay slightly faster then both the C_y and C_z defect populations at the late times; note, however, that our statistics for the $\overline{C}_0$ defects are rather poor.

We now explain the reasons for the observed rapid decay of the C_x population, and the presence, in comparable numbers, of the C_y and C_z defects in the late-time

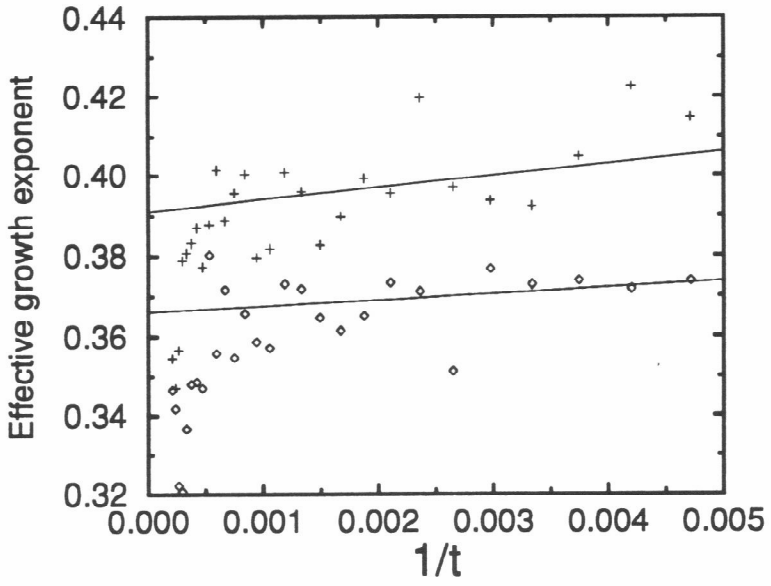

Figure 5.23: Effective growth exponents for the separation between C_y defects (shown as $\diamond$), and between C_z defects (shown as $+$), analyzed using the extrapolation formula (15b).

regime. According to Table I, a pair of C_x, C_y, or C_z defects can annihilate to give a topologically trivial configuration. These processes indeed occur frequently in the simulation (see Fig. 5.18). After the system takes advantage of these "decay channels", however, two nearby defects of the same species are frequently "screened" by a defect of a different species located between them. The system can then reduce the number of defects through the reactions

$$C_x + C_y \rightarrow C_z \tag{5.40}$$

$$C_x + C_z \rightarrow C_y \tag{5.41}$$

$$C_y + C_z \rightarrow C_x\,. \tag{5.42}$$

Reactions (5.40) and (5.41) were observed frequently in the simulation; the inverse reactions $C_z \rightarrow C_x + C_y$ and $C_y \rightarrow C_x + C_z$ were observed only occasionally, and were

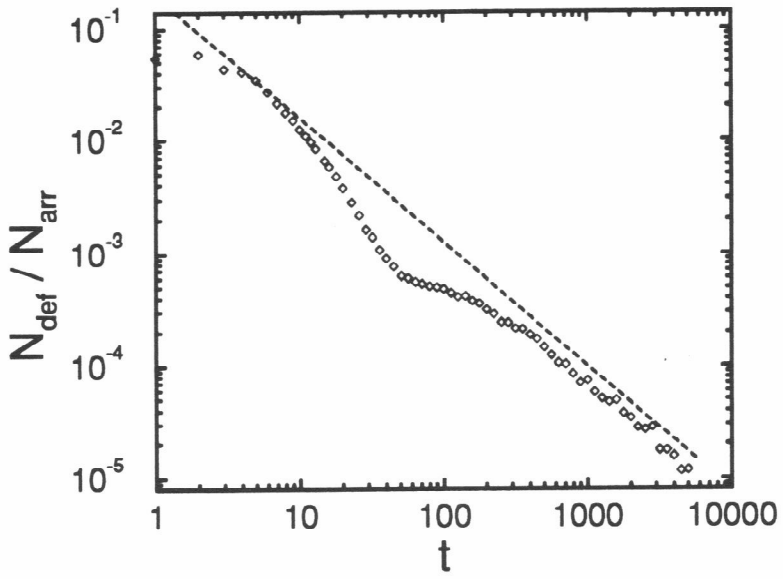

Figure 5.24: The ratio of the number of $\overline{C}_0$ defects to the number of 4×4 arrays of cells with no 180° defects, plotted as a function of time. The slope of the straight line is -1.10.

always followed by the annihilation of the generated C_x defect, through reactions (5.41), (5.40), or the *inverse* of the reaction (5.42), i.e., $C_x \rightarrow C_y + C_z$. This leads us to conclude that the reactions $C_x + C_y \rightarrow C_z$ and $C_x + C_z \rightarrow C_y$ are exoergic, whilst the reaction $C_y + C_z \rightarrow C_x$ is endoergic. The system therefore tends to annihilate the C_x defect whenever another defect (of type C_y or C_z) is found in its vicinity, while the production of the C_x defect is always energetically disadvantageous, which explains the rapid annihilation of the C_x population. It is interesting to note that the C_x defects appear in the system in small numbers even at very late times (see Table II); the apparent reason is that a C_y or C_z defect can use a short-lived creation of the C_x defect to move through the system (see Figs. 5.18c-e) in order to take part in the $C_y + C_y \rightarrow C_0$ and $C_z + C_z \rightarrow C_0$ reactions, which are the dominant decay channels in the late time regime.

No decay channel in which the number of C_y defects is reduced without producing a C_z defect (or vice versa) is available, except for the mutual annihilations of two C_y or C_z defects; these occur with a probability proportional to the square of number density of the C_y or C_z species, which remain approximately equal, because the two species were present at roughly equal numbers when the C_x defects disappeared from the system. The numbers of C_y and C_z defects are thus *locked* at late times; the explanation of the slight difference in the effective exponents describing their decay with time would require a more detailed knowledge of the energetics of the processes involved, including the reactions involving the catalyst C_x. Thus far, we have not included in our discussion the influence of the $\overline{C}_0$ (360°) defects. These were present only in small numbers, even at the later times, when the $\overline{C}_0$ defect-counting algorithm overcomes the problem discussed earlier in this section. It is also clear from Table I that the events involving the $\overline{C}_0$ defects cannot change the mechanism of the C_y and C_z species selection, discussed above. The tendency of the $\overline{C}_0$ defect population to decay at a rate faster than the decay rate of the C_y and C_z defect populations at late times is readily understood: in addition to the decay channels $\overline{C}_0 + C_y \rightarrow C_y$ and $\overline{C}_0 + C_z \rightarrow C_z$, occurring at rates tied to the number densities of the C_y and C_z defects, $\overline{C}_0$ can decay through the exoergic processes $\overline{C}_0 \rightarrow C_i + C_i$ (where $i = x, y, z$) and the (very rare) process $\overline{C}_0 + \overline{C}_0 \rightarrow C_0$.

In recent work Kobdaj and Thomas [29] investigated the energies and interactions of non-abelian point defects topologically equivalent to the C_x, C_y, and C_z defects in biaxial nematics. The gradient part of the energy density used in [29] is equivalent to the one-constant elastic free energy adopted in our simulations. Kobdaj and Thomas show that if one neglects the core energies (which depend on the homogeneous part of energy), the energy of the C_x defect exceeds the sum of energies of a C_y defect and a C_z defect. This is consistent with the mechanism for the selection of defect species presented in the previous paragraphs.

5.6 Summary and conclusions

Detailed analysis of our results showed that dynamical scaling is violated throughout the studied time range. To reach this conclusion, we had to compare the growth laws for the correlation length and for the average separation between topological defects. Studying the correlation function alone does not indicate the violation of dynamical scaling. We also showed that the observed discrepancy between the growth exponents of the correlation length and of the characteristic length determined from the energy density does not necessarily indicate a violation of dynamical scaling.

In order to explain why the growth exponents observed in our simulations were significantly lower than 0.5, we studied the annihilation process of an isolated pair of uniaxial nematic defects. Our results show that the lowered value of the effective growth exponent $\phi_{\rm def}$ for the average separation of defects may be understood by analyzing the forces acting on the point defects, similarly to the treatment of phase ordering in the $O(2)$ vector XY model in [12].

The analysis discussed in the preceding paragraph suggests that the effective growth exponent $\phi_{\rm def}$ should approach the value of 0.5 in the regime where the average separation between defects becomes much larger than the size of the defect cores. In this regime we expect that the growth exponent for the correlation length, $\phi_{\rm cor}$, also reaches the value of 0.5, and the correlation function truly collapses. The difference between $\phi_{\rm cor}$ and the growth exponent for the energy length ($\phi_{\rm en}$), analyzed in Sec. 5.3.4, is predicted to vanish in this regime [see Eq. (5.27)]. We therefore expect that in the late stages of the phase ordering of a sufficiently large nematic system, dynamical scaling will hold, and that all characteristic length-scales in the system will grow as a power law of time with the growth exponent equal to 0.5. Due to the logarithmic corrections to the true asymptotic values of the growth exponents, studied in Secs. 5.3.4 and 5.5.1, however, it is not presently possible to access the true scaling regime in computer simulations.

An important ingredient missing from the analysis of the behavior of the growth

exponents is an explanation of the discrepancy between the growth exponents for the average separation of defects and for the correlation length. An analytical and numerical analysis of the role of degrees of freedom other than the defect coordinates in the phase ordering process is currently in progress [14].

In Secs. 5.4 and 5.5.2, we studied the properties of the 4 topologically distinct species of defects present in a biaxial nematic during the phase ordering process. The topological character of the defects and the defect interactions observed in our simulations agree with the predictions of the topological classification scheme. Of the 4 allowed defect species, only 2 were observed in large numbers at late stages of the ordering process. We proposed a mechanism for the selection of the prevailing defect species, based on the combination laws following from the topological classification scheme. It would be interesting to test these predictions experimentally.

References

[1] Recent results in phase ordering of systems with continuous symmetry are reviewed in A. J. Bray, Physica A **194**, 41(1993).

[2] M. Mondello and N. Goldenfeld, Phys. Rev. A **42**, 5865 (1990).

[3] M. Mondello and N. Goldenfeld, Phys. Rev. A **45**, 657 (1992).

[4] R. E. Blundell and A. J. Bray, Phys. Rev. A **46**, 6154 (1992).

[5] H. Toyoki, Phys. Rev. E **47**, 2558 (1993).

[6] A. J. Bray, S. Puri, R. E. Blundell and A. M. Somoza, Phys. Rev. E **47**, 2261 (1993).

[7] I. Chuang, R. Durrer, N. Turok and B. Yurke, Science **251**, 1336 (1991).

[8] I. Chuang, B. Yurke, A. N. Pargelis and N. Turok, Phys. Rev. E **47**, 3343 (1993).

[9] A. P. Y. Wong, P. Wiltzius and B. Yurke, Phys. Rev. Lett. **69**, 3583 (1992); A. P. Y. Wong, P. Wiltzius, R. G. Larson and B. Yurke, Phys. Rev. E **47**, 2683 (1993)

[10] R. E. Blundell and A. J. Bray, preprint (1993).

[11] A. J. Bray and A. D. Rutenberg, Phys. Rev. E **49**, 27(1994).

[12] B. Yurke, A. N. Pargelis, T. Kovacs and D. A. Huse, Phys. Rev. E **47**, 1525 (1993).

[13] N. D. Mermin, Rev. Mod. Phys. **51**, 591 (1979).

[14] M. Zapotocky, P. M. Goldbart and N. Goldenfeld, work in progress.

[15] Note that the order parameter tensor $Q_{\alpha\beta}$ can be expressed in terms of the components of the uniaxial axis $\pm\mathbf{u}$ and biaxial axis $\pm\mathbf{b}$ as $Q_{\alpha\beta} = \frac{3}{2}S_1(u_\alpha u_\beta - \frac{1}{3}\delta_{\alpha\beta}) + \frac{1}{2}S_2(b_\alpha b_\beta - v_\alpha v_\beta)$, where $\mathbf{v} = \mathbf{u} \times \mathbf{b}$. The scalars S_1, resp. S_2 determine the strength of uniaxial, resp. biaxial ordering.

[16] E. Gramsbergen, L. Longa and W. de Jeu, Phys. Rep. **135**, 196 (1986).

[17] see, e.g., P.-G. de Gennes and J. Prost, *The Physics of Liquid Crystals* (Clarendon, Oxford, 1993).

[18] Y. Oono and S. Puri, Phys. Rev. Lett. **58**, 836 (1987); Phys. Rev. A **38**, 434 (1988).

[19] I. M. Lifschitz, Zh. Eksp. Teor. Fiz. **42**, 1354 (1962) [Sov. Phys. JETP **15**, 939 (1962)]; S. M. Allen and J. W. Cahn, Acta Metall. **27**, 1085 (1979).

[20] A. J. Bray and K. Humayun, Phys. Rev. E **47**, 9 (1993)

[21] H. Toyoki, Phys. Rev. B **45**, 1965 (1992).

[22] See, however, the discussion of the contrary case in Sec. 5.5.1. In fact, Porod's law in the form $S(k,t) = A\,\rho_{\mathrm{def}}(t)\,k^{-\chi}$ is valid independently of any scaling assumptions. The exponent χ and the amplitude A were calculated exactly (from the order parameter-configuration of an isolated defect) in Ref. [20] for the $O(N)$ vector-model case. Analogous calculations have been performed by us for the uniaxial and biaxial nematic cases, and are reported in Appendix A of this thesis.

[23] T. De'Neve, M. Kleman and P. Navard, J. Phys. II (France) **2**, 187 (1992).

[24] Note that in the uniaxial quench case, intersections of four dark brushes (occasionally appearing in our Schlieren pictures) should not be interpreted as a topological defect. For example, the topologically trivial configuration in Fig. (5.12a), and the configurations generated during the escape of such a configuration to the uniform configuration in Fig. (5.12b), would appear as such an intersection.

[25] This is, of course, only valid provided topological defects can exist in the system. An example of a system where no singular topologically stable objects can exist is the $O(N)$ vector model in d dimensions for $N > d$ (see e.g. Ref. [13]).

[26] In 3 spatial dimensions, there is another consequence of the non-commutative character of the first homotopy group: some of the line defects (i.e., disclinations) classified by Π_1 cannot cross due to topological obstructions (see V. Poénaru and G. Toulouse, J. Phys. (Paris) **8**, 887 (1977), and our discussion of this property in Chapter 3 of the thesis). One may expect this to lead to a slowing down or complete impairment of the phase ordering process in 3-dimensional biaxial nematics. Extensions of the numerical simulations reported in this chapter to the case of three spatial dimensions (M. Zapotocky, P. M. Goldbart and N. Goldenfeld, manuscript in preparation) have, however, indicated that no entangled disclination loops occur in the system at late times after the quench to the biaxial nematic phase, and that the asymptotic rate of phase ordering in the studied system is not affected by the non-crossing property of non-abelian line defects. The lack of entanglement of disclination loops was also observed in the case of a quench to the *uniaxial* nematic phase. A study of the degree of generality, and reasons for, this striking property is currently in progress.

[27] A. J. Bray, S. Puri and K. Humayun, unpublished.

[28] Although we find that the correlation length and the separation of defects have slightly different growth exponents (see Sec. 5.5.1), over the range of times accessible in our simulation they remain comparable in magnitude.

[29] Ch. Kobdaj and S. Thomas, *Nonabelian vortices.* Nucl. Phys. B **413**, 689 (1994).

Chapter 6

Kinetics of phase ordering with topological textures

6.1 Introduction

Recent work has shown [1] that many features of phase ordering in systems supporting topologically stable singular defects (for example, in systems described by the O(N) vector model in d dimensions with $d \geq N$ [2], or in two and three-dimensional nematic liquid crystals [3]) can be understood theoretically by investigating the dynamics of the numerous topological defects generated during the quench. In systems where topologically stable singular objects cannot occur (for example, in the O(N) model system in dimension $d < N$), such an approach cannot be used. A special and interesting case is that of the O(N) model system in $N - 1$ spatial dimensions, which supports topologically stable, but non-singular objects—topological textures. In the present chapter, we report results from an investigation of the role played by topological textures during the phase ordering of an O(3) vector model system in two spatial dimensions. This system has been previously investigated by Toyoki [4], who calculated the time dependence of the order parameter correlation function, and by Bray and Humayun [5], who investigated the decay of the free energy in the system. A detailed analysis of the phase ordering process in terms of the behavior of the topological objects present in this system, however, has not been previously given [6]. The results described in this chapter were obtained in collaboration with Wojtek J. Zakrzewski.

6.2 The discretized non-linear O(3) sigma-model and the simulation method

The model investigated in our simulations is the non-linear O(3) sigma-model on a two-dimensional lattice. The order parameter $\mathbf{m}$ is correspondingly a 3-component vector with unit magnitude; the local value of the order parameter $\mathbf{m}(\mathbf{r}, t)$ will be referred to as the spin. The phase-ordering simulation is started with randomly oriented spins, corresponding to the configuration generated immediately after a quench to zero temperature. The configuration is then evolved using the dissipative dynamical equation

$$\frac{\partial \mathbf{m}}{\partial t} = \nabla^2 \mathbf{m} - (\mathbf{m} \cdot \nabla^2 \mathbf{m})\mathbf{m}\,, \tag{6.1}$$

where the second term on the right hand side enforces the constraint $\mathbf{m} \cdot \mathbf{m} = 1$. To adequately describe the phase-ordering process, Eq. (6.1) must be regularized on a scale given by the order parameter coherence length [7]; we effectively impose the regularization condition by considering Eq. (6.1) on a discrete lattice. We evolved Eq. (6.1) using the technique developed in Ref. [8] (based on the 4th order Runge-Kutta method) appropriately adapted to our case. The spatial discretization step was taken to be $dx = dy = 0.1$, the time step was $dt = 0.0002$, and we worked with periodic boundary conditions. We used system sizes between 252 and 512 lattice units, and our longest runs reached times $t = 40$.

6.3 The two competing processes: topological charge annihilation vs. single-texture unwinding

We now briefly review the concept of a topological texture [9]. The spin configuration of a single texture in an infinite continuum system is given by

$$m_x(\mathbf{r}) = \frac{4ax}{r^2 + 4a^2}\ ,\ m_y(\mathbf{r}) = \frac{4ay}{r^2 + 4a^2}\ ,\ m_z(\mathbf{r}) = \frac{r^2 - 4a^2}{r^2 + 4a^2}\ . \tag{6.2}$$

The orientation of the spin changes from up in the center of the texture ($r = 0$) to down at the boundary of the system ($r = \infty$), going through a vortex-like configuration with spins pointing radially outwards on the circle $r = 2a$. It is easily seen

that the spin configuration (6.2) covers the order parameter space (given in our case by the unit sphere in three dimensions) exactly once, corresponding to a topological charge of one (see Chapter 3 for a discussion of topological stability of the texture configuration). It is possible to show that the configuration (6.2) (or any global rotation thereof) has the minimum energy (with energy density taken as $\frac{1}{8\pi}(\nabla \mathbf{m})^2$) of all configurations with topological charge one. The value of the minimum total energy is $E = 1$. By an *antitexture*, we mean a configuration similar to (6.2), but with $m_y(\mathbf{r})$ replaced by $-m_y(\mathbf{r})$. This configuration wraps around the spin sphere once, but in the opposite sense compared to (6.2), corresponding to topological charge -1.

The crucial quantity for our investigation of the role of textures and antitextures in the phase ordering process is the *topological charge density* $q(\mathbf{r})$

$$q(\mathbf{r}) = \frac{1}{4\pi}\mathbf{m} \cdot (\partial_x \mathbf{m} \times \partial_y \mathbf{m}) \tag{6.3}$$

which, when integrated over the whole system, gives the total topological charge. For the single texture configuration (6.2), the topological charge density has the form $q(r) = \frac{1}{\pi} 4a^2/(r^2 + 4a^2)^2$, and exhibits a pronounced peak at $r = 0$ with half-width $1.287 \cdot a$. For a single antitexture, $q(r)$ is of the same form, only negative.

In Fig. (6.1) a-c, we plot the topological charge density at a progressive series of times in a section of a system undergoing phase ordering. The plots exhibit numerous well defined peaks and antipeaks, corresponding at later times to rather well separated textures and antitextures of varying sizes. The average separation between the textures (or antitextures) grows, and at the latest time, the system is strongly "intermittent" in the sense that the topological charge density differs significantly from zero only within very well localized regions, with the spin configuration practically homogeneous in between. Note that the "typical" texture size does not appreciably increase with time.

A detailed inspection of series of plots similar to Fig. (6.1), taken at closer values of time, reveals that the variations in topological charge density decay through two distinct processes: single texture (or antitexture) unwinding, and topological charge

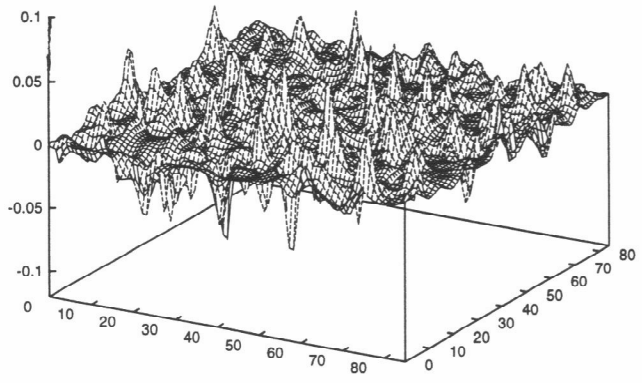

(a)

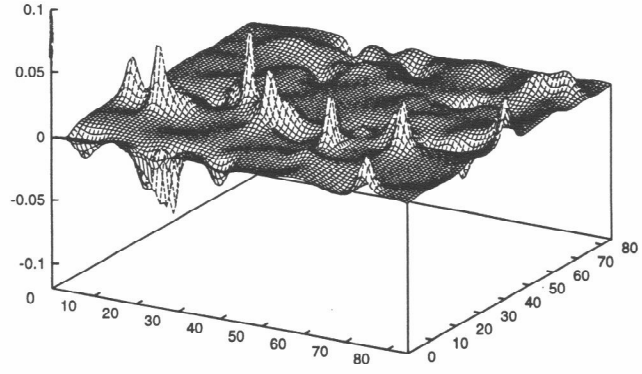

(b)

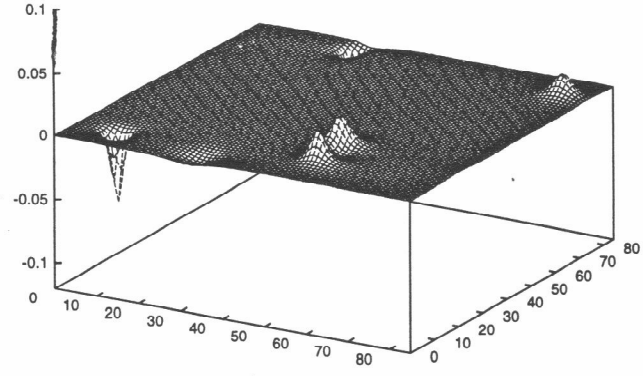

(c)

Figure 6.1: Surface plots of the topological charge density $q(\mathbf{r})$ in a 85×85 section of a phase ordering system at time (a) t=0.0356, (b) t=0.126, and (c) t=1.59. The horizontal scale is in units of one lattice spacing.

annihilation. The first process appears as a growing isolated peak in topological charge density, and corresponds to a localized configuration of type (6.2) with decreasing size a. Such a process would conserve the total topological charge and the total energy of the texture in a continuum system; in a discrete system, however, this conservation is strongly violated once the texture size decreases to several lattice spacings. Eventually, the texture comes (up to a global rotation) close to the extreme configuration where the spin points up at the center lattice point, and down everywhere else; such a configuration has only $1/2\pi$ of the original texture energy. This configuration is followed by a flip of the central spin, and the complete disappearance of the texture [10]. The size a of the shrinking texture in our simulation varied very roughly as $\tau^{1/4}$, where τ is the time remaining to the flip.

The second process visible in the topological charge density plots is the mutual annihilation of overlapping regions of positive and negative topological charge density (overlapping in the sense that they are not separated by a region where $q(\mathbf{r}) = 0$). In Fig. (6.2), we show the evolution starting from a slightly overlapping texture - antitexture pair. The height of the two peaks decays, and the overlap of the regions of positive and negative $q(\mathbf{r})$ increases with time. The peaks initially move slightly together, but later move significantly apart [11]. It is important to realize that this "texture-antitexture annihilation" process differs radically from the process of annihilation of a singular defect with it's antidefect (*e.g.* a vortex and an antivortex in the 2d O(2) model), where the singular cores keep their identities and gradually approach. In the texture-antitexture annihilation, the total charge enclosed by each of the regions of positive and negative $q(\mathbf{r})$ gradually decays to zero, and the annihilation of topological charge occurs independently of whether a complete texture and antitexture are present. In contrast to this, the mechanism of unwinding (discussed in the previous paragraph) occurs only if the unwinding region encloses a total topological charge close to 1 or -1.

In order to assess the relative importance of the two processes discussed above during phase ordering, we investigated the time dependence of the quantities Q_+ and

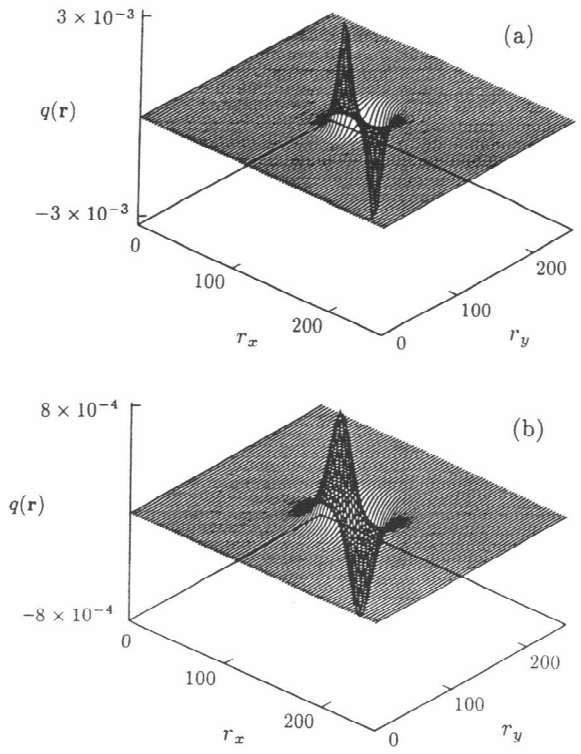

Figure 6.2: The process of topological charge annihilation, starting from an overlapping full texture and antitexture. The plots show $q(\mathbf{r})$ for (a) $t = 0$ (initial configuration) and (b) $t = 3.0$. Note that the vertical scale is different in (a) and (b). The quantity $P = \int d^2r|q(\mathbf{r}|$ decays from 1.54 in (a) to 0.89 in (b).

Q_-, defined by

$$Q_+ = \int d^2r \max[q(\mathbf{r}), 0], \qquad Q_- = \int d^2r \min[q(\mathbf{r}), 0] \tag{6.4}$$

where the integral is over the whole system. In a system with well separated textures and antitextures, Q_+ counts the number of textures, Q_- counts the number of antitextures, $Q = Q_+ + Q_-$ gives the total topological charge, and $P = Q_+ - Q_-$ counts the total number of topological objects in the system. Figure (6.3) shows that at late times, the the total topological charge $Q = Q_+ + Q_-$ varies only in sharp steps of size -1 or $+1$, corresponding to an unwinding of a single texture, resp. antitexture. The steps are also visible in the corresponding $Q_+(t)$ or $Q_-(t)$ curve (see Fig. (6.3)). Note, however, that while the $Q(t)$ curve is flat, the $Q_+(t)$ and $Q_-(t)$ curves decay significantly in between the unwinding steps. This demonstrates that the process of topological charge annihilation, as defined in the previous paragraph,

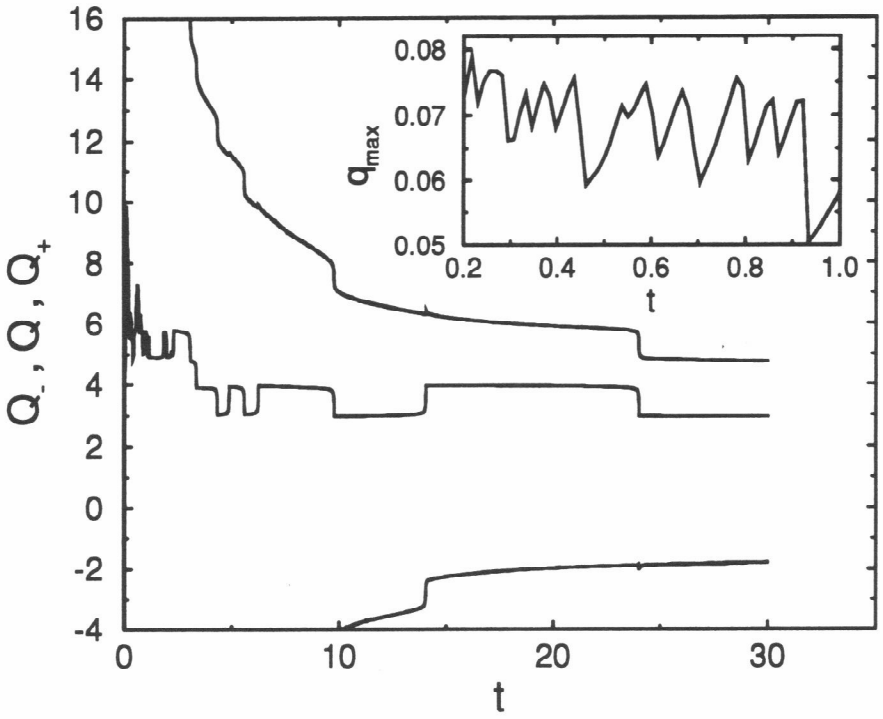

Figure 6.3: Time dependences of the quantities $Q_{-}(t)$ (lower curve), $Q(t)$ (middle curve), and $Q_{+}(t)$ (upper curve) during phase ordering of a system of size 252×252. Inset: Time dependence of $q_{max}(t)$.

takes place. The relative importance of the unwinding and annihilation processes in a given time range is given by the ratio of the number of steps in the $Q(t)$ curve to the total drop of the integrated absolute topological charge density $P = Q_{+} - Q_{-}$. In the time interval between $t = 3$ and $t = 30$, this ratio is $\rho = 0.45$, showing that in this time range, unwindings and the annihilation processes play almost equally important roles. At earlier times, it is difficult to calculate the ratio ρ, as the total topological charge Q of a large system no longer exhibits well separated steps. A lower bound for ρ, however, may be still obtained by counting the sharp peaks (see the inset in Fig. (6.3)) occurring in the curve $q_{max}(t)$, where q_{max} is defined as the maximum of $|q(\mathbf{r})|$ over the whole system. Each peak corresponds to the final stages of shrinking

and consequent flipping of a texture or antitexture; however, if two textures unwind at almost the same time in two different parts of the system, only one peak may be visible. Comparing the number of peaks with the drop in $P(t)$ in the time interval from $t = 0.5$ to $t = 1.0$ gives $\rho \geq 0.25$. This is consistent with the expectation that since the textures and antitextures are better separated as t increases [see Fig. (6.1)], ρ should increase with time.

6.4 Violations of dynamical scaling

We now present results averaged over 14 runs in a system of size 512, evolved until $t = 1.6$. Longer runs in systems of size 252 gave similar results. The total topological charge Q was approximately conserved and close to zero ($|Q(t)| < 5$ at all t). In Fig. (6.4), we plot the integrated absolute charge $P = Q_+ - Q_-$, the free energy E, and their difference. The asymptotic equality of E and P indicates that at late times, the system is well separated into textures and antitextures, each of energy 1. Note that the inequality $E(t) > P(t)$ is satisfied at all times; this is consistent with the well known [12] global inequality $E \geq |Q|$ being valid inside each region containing a texture or an antitexture [13]. Both P and E decay asymptotically as $t^{-0.64\pm0.02}$, indicating that the average separation $D(t)$ between topological objects (textures or antitextures) grows as $t^{0.32\pm0.01}$. Note that this differs significantly from the dimensional analysis prediction of a length scale growing as $t^{1/2}$, and points towards the presence of scaling violations. In contrast, the difference $E(t) - P(t)$, characterizing topologically trivial spin variations, decays asymptotically as $t^{-0.92\pm0.03}$ [see the inset in Fig. (6.4] which agrees much better with the dimensional analysis result. The onset of the approximate power-law regime for $P(t)$ occurs at $t \simeq 0.02$, corresponding to the time after which well formed textures and antitextures are seen in the topological charge density plots.

We calculated three separate correlation functions: the spin-spin correlation $C(r,t) = \langle \mathbf{m}(\mathbf{x},t) \cdot \mathbf{m}(\mathbf{x}+\mathbf{r},t) \rangle$, the topological charge density correlation $C_q(r,t) = \langle q(\mathbf{x},t) q(\mathbf{x}+\mathbf{r},t) \rangle / \langle q(\mathbf{x},t) q(\mathbf{x},t) \rangle$, and the correlation of the absolute topological charge density,

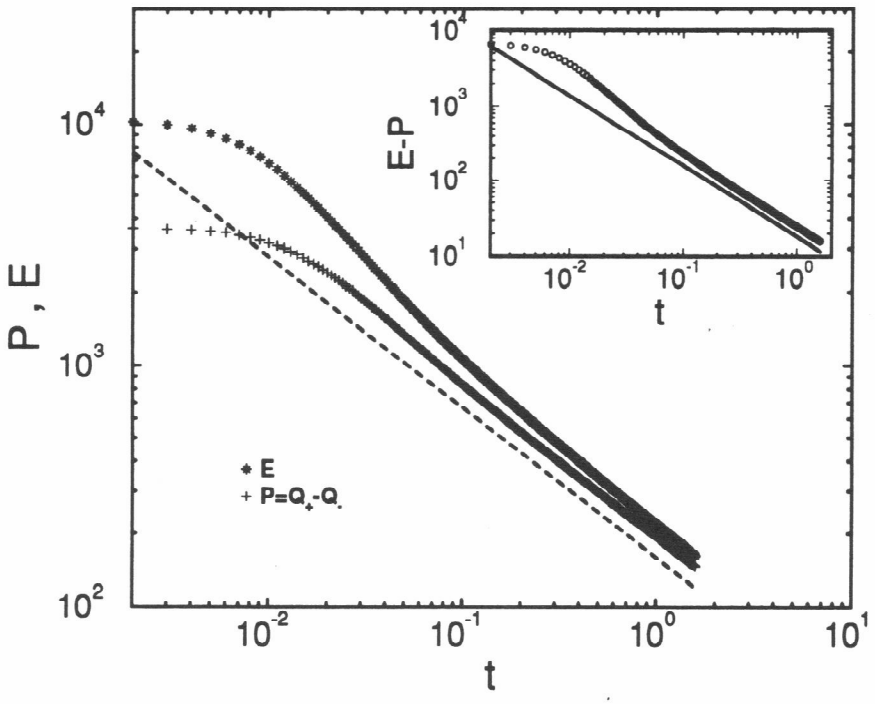

Figure 6.4: Time dependences of the integrated absolute charge $P(t)$ and the free energy $E(t) = \int d^2r \frac{1}{8\pi}(\nabla \mathbf{m})^2$ during phase ordering of a system of size 512×512, averaged over 14 initial conditions. The dashed line has a slope of -0.64. Inset: The decay of the difference $E(t) - P(t)$. The solid line has a slope of -0.92.

$C_p(r,t) = \langle p(\mathbf{x},t)p(\mathbf{x}+\mathbf{r},t)\rangle / \langle p(\mathbf{x},t)p(\mathbf{x},t)\rangle$ (here $p(\mathbf{x}) = |q(\mathbf{x})| - \langle |q| \rangle$, and $\langle .. \rangle$ denotes averaging over the whole system). We define the length scales $L(t)$, $L_q(t)$ and $L_p(t)$ as the half-widths of the central maxima of the correlation functions $C(r,t)$, $C_q(r,t)$ and $C_p(r,t)$, respectively. We find that these length scales grow differently from each other (see the inset in Fig. (6.5)) and from the average separation of topological objects $D(t)$, indicating that dynamical scaling is violated. The half-widths $L_q(t)$ and $L_p(t)$ do not grow as power-laws of time, but rather as $a\log(bt)$, where a and b are constants. The half-width of the spin-spin correlation, $L(t)$, grows much faster, and at late times fits the power law $L(t) \propto t^{0.38\pm0.02}$ [14].

We furthermore find that each family of the correlation functions individually does not collapse onto a universal curve, providing a further indication of the violation of dynamical scaling. In Fig. (6.5), we show an attempt to collapse the correlation functions $C(r,t)$, $C_q(r,t)$ and $C_p(r,t)$ using the lengths $L(t)$, $L_q(t)$ and $L_p(t)$. The lack of collapse is most readily apparent in the topological charge correlation $C_q(r,t)$ [15]. A more detailed discussion of our results for the topological correlation functions will be given separately.

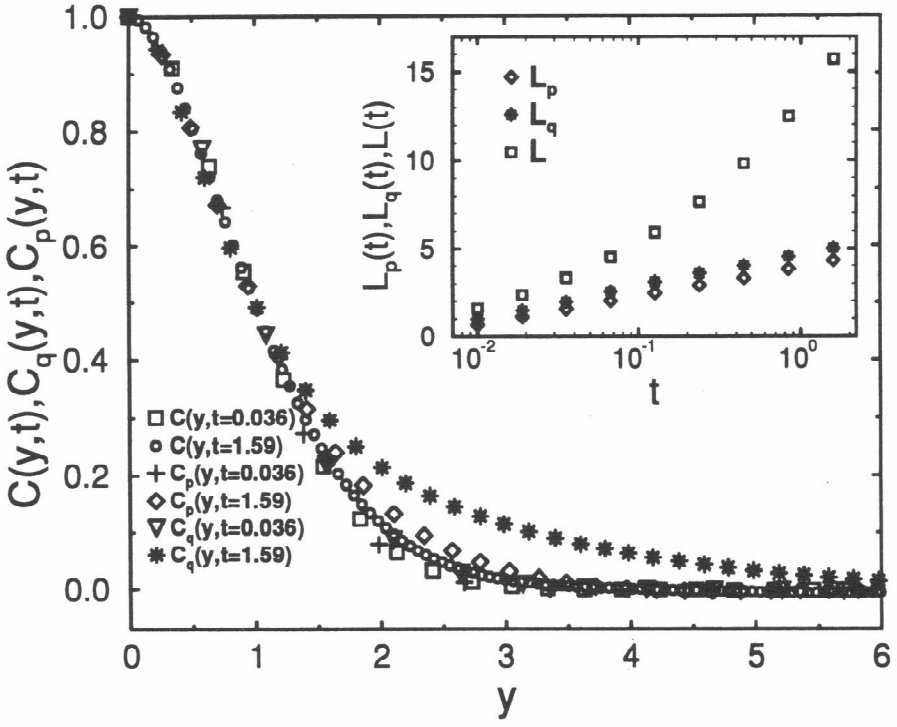

Figure 6.5: The rescaled correlation functions $C(r/L(t))$, $C_q(r/L_q(t))$ and $C_p(r/L_p(t))$ at specified times (see the main text for definitions). Inset: growth of the length scales $L(t)$, $L_q(t)$ and $L_p(t)$ (note that the graph is semilogarithmic).

6.5 Conclusions

In conclusion, we have characterized the phase ordering kinetics in the investigated system in terms of the distinct processes of single-texture unwindings and topological charge annihilation, and demonstrated that dynamical scaling is strongly violated. Most of the methods developed in this chapter should be equally well applicable to phase ordering in systems with topological textures in higher dimensions.

References

[1] For a recent review of the theory of phase ordering, see A. J. Bray, Advances in Physics (in press).

[2] A. J. Bray and K. Humayun, Phys. Rev. E **47**, 9 (1993); B. Yurke et al., Phys. Rev. E **47**, 1525 (1993).

[3] M. Zapotocky, P. M. Goldbart and N. Goldenfeld, Phys. Rev. E **51**, 1216 (1995); M. Zapotocky and P. M. Goldbart, manuscript in preparation, and Appendix A of this thesis.

[4] H. Toyoki, Mod. Phys. Lett. B **7**, 397 (1993).

[5] A. J. Bray and K. Humayun, J. Phys. A **23**, 5897 (1990).

[6] During the write-up of this article, we received a preprint by A. D. Rutenberg, who has independently investigated phase ordering in the Heisenberg model in two dimensions. Although the emphasis of the two articles is somewhat different, our numerical results agree where the two papers overlap.

[7] Considering the $O(3)$ non-linear σ-model *in the continuum* fails to take into account that when sufficiently strong spatial variations of the physical order parameter are present, its magnitude is significantly reduced due to the competition between the condensation and gradient parts of the free energy. The length scale on which the order parameter needs to vary for its magnitude to be substantially reduced is called the *coherence length*. Taking the lattice unit in our simulations to be smaller than the coherence length would be inconsistent with the

σ-model (i.e., fixed order parameter magnitude) character of our description of the system.

[8] R. A. Leese, M. Peyrard and W. J. Zakrzewski, Nonlinearity **3**, 387 (1990).

[9] See, *e.g.*, R. Rajaraman, *Solitons and Instantons* (North Holland, Amsterdam, 1982)

[10] The unwinding process occurs somewhat differently – through the reduction of the order parameter magnitude in the center of the texture – in the "soft-spin" continuum O(N) vector model. In both the discrete non-linear sigma model and the continuum "soft-spin" model, however, the texture disappears once it reaches a certain *finite* radius.

[11] Details of our investigation of the annihilation process will be reported separately.

[12] A. A. Belavin and A. M. Polyakov, JETP Lett. **22**, 245 (1975).

[13] Neighboring regions with small amounts of positive and negative topological charge, undergoing annihilation, can have E substantially larger than P [10]. However, the contribution of such regions to the total values of E and P in the whole system is small.

[14] This is roughly consistent with the result $L(t) \propto t^{0.42\pm0.03}$ in [4].

[15] M. Zapotocky and W. J. Zakrzewski, abstract submitted to the March 1995 Meeting of the APS, Bull. Amer. Phys. Soc. (in press).

Chapter 7

Dynamical multi-scaling in quenched Skyrme systems

7.1 Introduction

In the previous chapter, we investigated the phase ordering process in the two-dimensional $O(3)$ non-linear σ-model, and found that dynamical scaling was strongly violated in the time range studied. We diagnosed the violations of scaling by computing several distinct length scales characterizing the system and showing that they grow differently in time, as well as by showing that it is not possible to achieve to collapse of our data for the correlation functions of either the order parameter and or the topological charge density. We also found that at late times after the quench, the order parameter variations in the system are predominantly due to the presence of numerous topological textures and antitextures—non-singular, but topologically stable objects of variable size. The late stages of phase ordering were found to occur through two distinct processes—topological charge annihilation, and single-texture (or single-antitexture) unwinding. It is natural to ask whether the scaling violations are a direct result of the competition of these two distinct processes during the evolution of the system. In the present chapter, we eliminate the texture unwindings from the system through appropriate modifications of the free energy, and study how the behavior of the system is affected when only topological charge annihilation occurs. The results described in this chapter were obtained in collaboration with Andrew D. Rutenberg and Wojtek J. Zakrzewski.

In Sec. 6.3, the process of single-texture unwinding was found to be the conse-

quence of the lattice discretization, with the lattice unit corresponding physically to the coherence length of the order parameter. As discussed in the previous chapter, the lattice has the effect of lowering the energy of smaller textures (i.e. textures spread over a smaller number of lattice sites), and therefore destabilizes the textures towards shrinking. Similarly, it was found in [1] that textures are destabilized and unwind in the two-dimensional Heisenberg model (differing from the non-linear $O(3)$ σ-model by permitting variations in the magnitude of the order parameter). In general, the texture shrinking can be understood as coming from modifications to the basic form of the free energy

$$E_{\rm ex} = \frac{1}{8\pi}\int d^2r\,(\nabla \mathbf{m})^2 \equiv \frac{1}{8\pi}\int d^2r\,\sum_{i=1}^{3}(\partial_x m_i \partial_x m_i + \partial_y m_i \partial_y m_i)\,, \qquad (7.1)$$

which effectively induces higher-order gradient terms in the energy density given in Eq. (7.1), and thus breaks the invariance of Eq. (7.1) with respect to the texture size. It is clear that if the coefficient of the leading higher-order gradient term is negative—thus reducing the energy if order parameter gradients are large—the textures will be destabilized towards shrinking. We can thus prevent the textures from unwinding by adding a fourth-order gradient term having a sufficiently large *positive* coefficient. In general, it is difficult to achieve real stabilization (i.e., invariance with respect to the size) of the textures in this way, and we shall instead work with *weakly expanding* textures. The replacement of texture shrinking by texture expansion is a significant *qualitative* change, as now the absolute value of the topological charge (the quantity P of the previous chapter) can decay only through mutual annihilation of regions of positive and negative charge, and the system no longer tends to increase order parameter gradients at any fixed location. We shall see that this leads to very significant modifications in the (multi-)scaling properties of the system.

7.2 The Skyrme term

What fourth order gradient term should be added to E_{ex} to prevent the unwinding events? A natural candidate for the stabilizing energy E_s to be added is

$$E_s = \frac{\theta_1}{16\pi} \int d^2r \, |(\partial_x \mathbf{m} \times \partial_y \mathbf{m})|^2 \,, \tag{7.2}$$

where θ_1 is a positive constant. The energy E_s is (in the sense explained in Refs. [2, 3]) the precise analog of the Skyrme term [4] used to stabilize topological textures in the $SU(2)$ model in three spatial dimensions. In that model, with solely the $(\nabla \mathbf{m})^2$–type term in the energy density, the textures would be unstable towards shrinking even in the continuum [5]. The Skyrme term ensures a fixed non-zero size of the textures (called skyrmions in this model); these are then identified with baryons in a corresponding quantized relativistic field theory [4].

In our case, the addition of the term Eq. (7.2) (with a sufficiently large value of θ_1) will make textures weakly unstable towards expansion rather than stabilizing them in size; however, that will be sufficient for our purposes. It is possible to stabilize a given texture in the two-dimensional $O(3)$ system by adding a third term of form $E_z = -g \int d^2r \, \mathbf{m}(\mathbf{r}) \cdot \mathbf{u}$ (with $g > 0$), where $\mathbf{u}$ is a unit vector giving the orientation of $\mathbf{m}$ at the center of the texture. This corresponds to a coupling of the order parameter $\mathbf{m}$ to an external field pointing in a fixed direction; the dynamics and interactions of skyrmion-like objects in such models [6] have been extensively studied in Refs. [2, 7, 8, 9]. However, the addition of such a term to our model would break the global $O(3)$ symmetry, thus significantly modifying the nature of the phase ordering problem. [A visible consequence of such symmetry breaking would be that as textures generated during the quench have random orientations of the order parameter $\mathbf{m} \equiv \mathbf{u}$ at the texture centers, coupling to a constant external field $\mathbf{B}$ would stabilize some of the textures (those with $\mathbf{u}$ pointing approximately anti-parallel to $\mathbf{B}$), but destabilize even more strongly the others (with $\mathbf{u}$ approximately parallel to $\mathbf{B}$).] We therefore content ourselves with using solely the Skyrme term Eq. (7.2), and having weakly expanding textures.

It is useful to note the following explicit relation of E_s, as defined in Eq. (7.2), to the second moment of the topological charge density $q(\mathbf{r})$. The quantity

$$4\pi q = \mathbf{m} \cdot (\partial_x \mathbf{m} \times \partial_y \mathbf{m}) \tag{7.3}$$

is simply the projection of the vector $\partial_x \mathbf{m} \times \partial_y \mathbf{m}$ on the direction given by the unit vector $\mathbf{m}$. As $\mathbf{m} \cdot \mathbf{m} = 1$, we have $\partial_x \mathbf{m} \cdot \mathbf{m} = \partial_y \mathbf{m} \cdot \mathbf{m} = 0$; therefore the vector $\partial_x \mathbf{m} \times \partial_y \mathbf{m}$ is parallel to $\mathbf{m}$, and has the same magnitude as $\mathbf{m} \cdot (\partial_x \mathbf{m} \times \partial_y \mathbf{m})$. Consequently, we have

$$(\partial_x \mathbf{m} \times \partial_y \mathbf{m}) \cdot (\partial_x \mathbf{m} \times \partial_y \mathbf{m}) = |\mathbf{m} \cdot (\partial_x \mathbf{m} \times \partial_y \mathbf{m})|^2 , \tag{7.4}$$

i.e., the Skyrme term Eq. (7.2) can be alternatively expressed as

$$E_s = \theta_1 \pi \int d^2 r \, q^2(\mathbf{r}) . \tag{7.5}$$

The term E_s can therefore be used as a local approximation to the Coulomb energy in the investigation [10] of the dynamics of skyrmionic excitations [11] in the quantum Hall effect, where the topological charge q is equivalent to the electric charge of electrons carrying the magnetization $\mathbf{m}$. (Note that in the quantum Hall effect model, it is appropriate also to add the term $E_z = g \int d^2 r \, \mathbf{m}(\mathbf{r}) \cdot \mathbf{B}$, where $\mathbf{B}$ has the direct physical significance of the external magnetic field). We shall not be concerned with the physics of quantum Hall systems in this chapter; however, the identity Eq. (7.5) still provides useful insight into the nature of the Skyrme term, and, furthermore, permits to check the consistency of our results for the scaling of the moments of the topological charge density (see Sec. 7.4).

7.3 Phase ordering with Skyrme dynamics

We now present numerical results for phase ordering in the presence of the Skyrme term. As in the previous chapter, we use purely dissipative dynamics: the equation of motion is obtained from $\partial \mathbf{m}(\mathbf{r}, t)/\partial t = -\delta(E_{ex} + E_s)/\delta \mathbf{m}(\mathbf{r}, t)$, with E_{ex} and E_s given by Eqs. (7.1) and (7.2), respectively, and with the variation with respect to

$\mathbf{m}(\mathbf{r}, t)$ carried out subject to the constraint $\mathbf{m} \cdot \mathbf{m} = 1$. We performed simulations on systems with size 512×512, using the numerical method briefly described in the previous chapter. The programming code for the evolution of the equation of motion was developed by Wojtek J. Zakrzewski. Values of the parameter θ_1 in the Skyrme term Eq. (7.2) investigated by us were in the range $0 - 0.012$. For most of the non-zero θ_1 values, only one or two runs were performed, and the error bars for our measurements are therefore greater than in the case $\theta_1 = 0$, where we averaged over 10 to 14 different initial conditions. The statistical accuracy achieved in our $\theta_1 > 0$ results is nevertheless sufficient to demonstrate the profound influence of the Skyrme term on the phase-ordering process.

In Fig. 7.1, we show a series of plots of topological charge density in a phase-ordering system with $\theta_1 = 0.012$, at times $t = 0.0356$, 0.126, and 1.59 after the quench. The plots should be compared to Fig. 1 in the previous chapter, where the topological charge density was plotted for the same times in a system with $\theta_1 = 0$. It can be seen that at $t = 0.0356$, the system with the stabilizing Skyrme term in fact appears more "random" than the system with no Skyrme term, where individual textures and antitextures can already be discerned. However, at $t = 0.126$, the configuration of the Skyrme system is already visibly more smooth than the configuration of the non-Skyrme ($\theta_1 = 0$) $O(3)$ system, and this difference grows even more pronounced at $t = 1.59$. It is seen that in the Skyrme system, no sharp peaks, corresponding to incipient unwinding textures or antitextures, occur at the later two times, and the Skyrme term with $\theta_1 = 0.012$ therefore appears adequate for preventing the singular unwinding events in the time range of interest. To verify this, we plot (in Fig. 7.2) the time dependencies of the maximum of total energy density $e_{\max}$ for runs in systems with Skyrme amplitudes $\theta_1 = 0.0039$, $\theta_1 = 0.006$, and $\theta_1 = 0.012$. The sharp peaks in $e_{\max}(t)$ with a gradual build-up on the left side, corresponding to the gradual shrinking of a small texture or antitexture, followed by a sharp drop on the right side, corresponding to its final unwinding, do occur at early times in each run. There is, however, a crossover to a regime where no unwindings are observed, and $e_{\max}(t)$

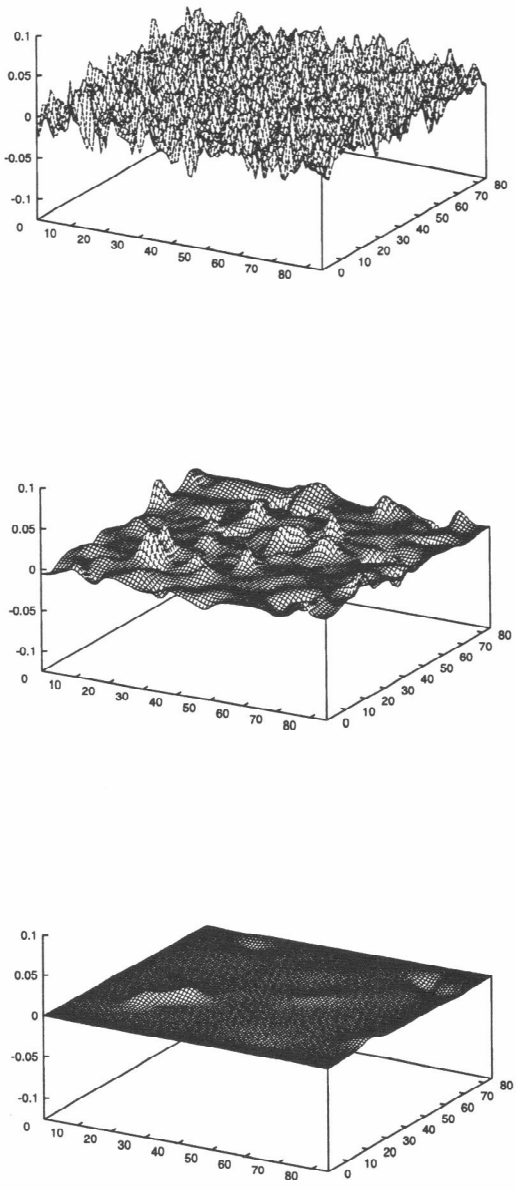

Figure 7.1: Surface plots of the topological charge density $q(\mathbf{r})$ in an 85×85 section of a phase-ordering system with Skyrme-term amplitude $\theta_1 = 0.012$. The plots correspond to configurations at time: (a) t=0.0356, (b) t=0.126, and (c) t=1.59 after the quench. The horizontal scale is in units of one lattice spacing.

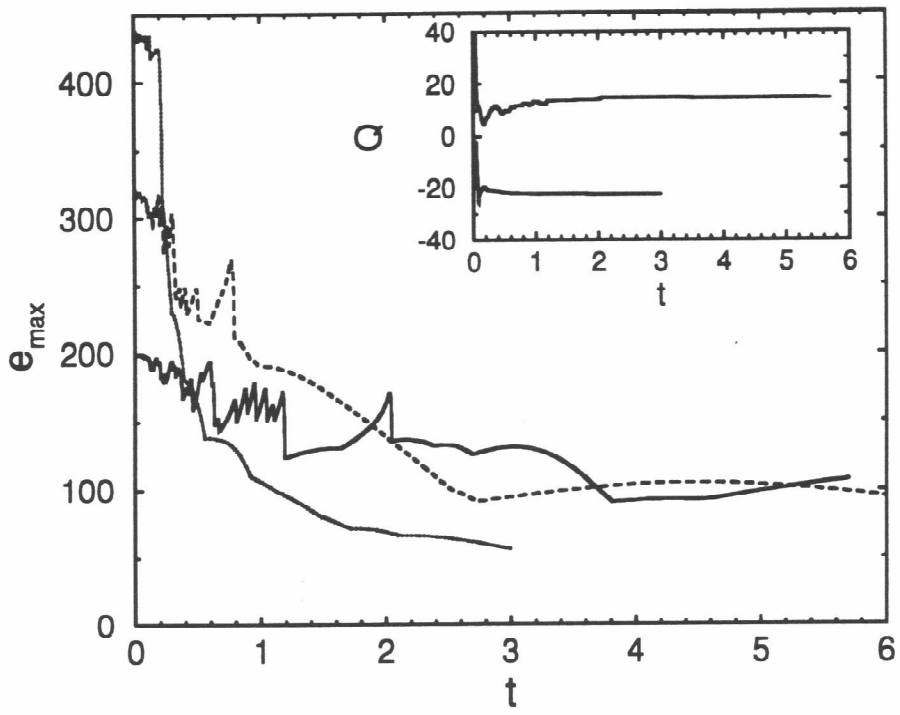

Figure 7.2: The maximum e_{max} of total energy in a system of size 512×512 as a function of time t. The three curves correspond to three different runs with Skyrme-term amplitudes $\theta_1 = 0.0039$ (full line), $\theta_1 = 0.006$ (dashed line) and $\theta_1 = 0.012$ (dotted line). Inset: total topological charge Q for the runs with $\theta_1 = 0.0039$ (upper curve) and $\theta_1 = 0.012$ (lower curve).

exhibits only slow oscillations. The crossover time is smaller for higher values of θ_1; for $\theta_1 = 0.012$, the crossover occurs at $t \simeq 0.2$ which, as we shall see, corresponds approximately to the time where a new (multi-)scaling regime develops in the system. The inset in Fig. 7.2 shows the time dependencies of the total charge Q in the system for $\theta_1 = 0.0039$ and $\theta_1 = 0.012$; it is seen that the time at which $Q(t)$ saturates to a constant value corresponds to the time at which the peaks in $e_{max}(t)$ stopped occurring for each of the θ_1 values. This is again consistent with topological charge annihilation (which conserves Q) being the only active mechanism for eliminating

topological charge variations in the system at the later times. (Below we shall refer to the corresponding time range for a given non-zero θ_1 value as the "pure annihilation regime", or "the regime with prevented unwindings".)

We have thus confirmed that adding the Skyrme term Eq. (7.2) with $\theta_1 = 0.012$ is sufficient to prevent unwindings in the system at late times . Does a Skyrme term of such strength dominate the energetics of the whole system? It can be seen from Fig. 7.3 that the answer is negative. Both the exchange energy $E_{\rm ex}$ and the Skyrme energy $E_{\rm s}$ decay as power laws of time after $t = 0.2$; however, $E_{\rm s}$ is smaller than $E_{\rm ex}$ by a factor of 20 at the beginning of the power-law regime, and the ratio further increases with time, because the exponent $\phi_{\rm s}$ in $E_{\rm s} \propto t^{-\phi_{\rm s}}$ is larger than the exponent $\phi_{\rm ex}$ in $E_{\rm ex} \propto t^{-\phi_{\rm ex}}$. In this sense, the exchange energy dominates the Skyrme energy at late times, and we have achieved our goal of stabilizing the textures against unwinding by adding a "small" corrective term.

Eliminating the unwindings, however, does have a profound influence on the scaling properties of the system. This can already be seen from the fact that $\phi_{\rm ex} = 0.5 \pm 0.05$ in Fig. 7.3; recall that for the case $\theta_1 = 0$, we obtained (in the previous chapter) $\phi_{\rm ex} = 0.64 \pm 0.02$. In Fig. 7.4, we compare the exchange energies for runs in systems with $\theta_1 = 0$, 0.0039, 0.006, and 0.012. It is seen that by increasing θ_1, the onset of the time when $E_{\rm ex}$ starts to drop significantly is shifted to higher times; for $\theta_1 = 0.012$, $E_{\rm ex}$ is still at its initial value at time $t = 0.02$, when the $E_{\rm ex}$ curve for the pure $O(N)$ system has already entered the scaling regime with $\phi_{\rm ex} = 0.64$. A sharp drop in $E_{\rm ex}$ occurs at later times, though, followed by an apparent power-law regime with $\phi_{\rm ex} = 0.5 \pm 0.05$, for all the runs with non-zero θ_1. The time of the crossover into the final power-law regime occurs earlier for larger θ_1 values, and approximately corresponds to the time characterizing the beginning of the unwinding-free regime in Figs. 7.2. While the behavior in the intermediate regime (in the approximate range $t = 0.02$–0.2) depends strongly on the value of θ_1, the late-time regime, once entered, is similar for all non-zero values of θ_1. The data presented point towards the existence of a new, annihilation-dominated scaling regime, with properties distinct from those

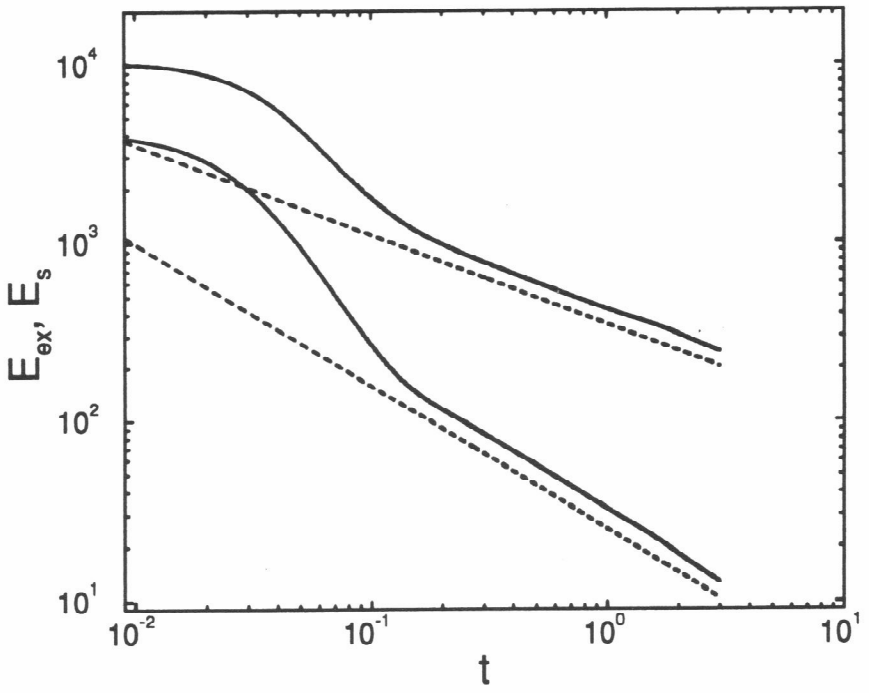

Figure 7.3: The exchange energy E_{ex} (upper solid curve) and Skyrme energy E_s (lower solid curve) for a run with $\theta_1 = 0.012$. The straight lines have slopes -0.5 (upper dashed line) and -0.8 (lower dashed line).

of the scaling regime in the non-Skyrme system. In the next section, we develop a systematic technique for studying the change in the (multi-)scaling properties, based on a detailed analysis of the distribution of the topological charge density.

7.4 Scaling of the moments of the topological charge density – the β_n curve

In the previous chapter we have seen that, at late times, non-Skyrme $O(3)$ σ-model exhibits a power-law dependence on time for various quantities—total energy, total positive charge, and the correlation lengths—that characterize the system. In contrast

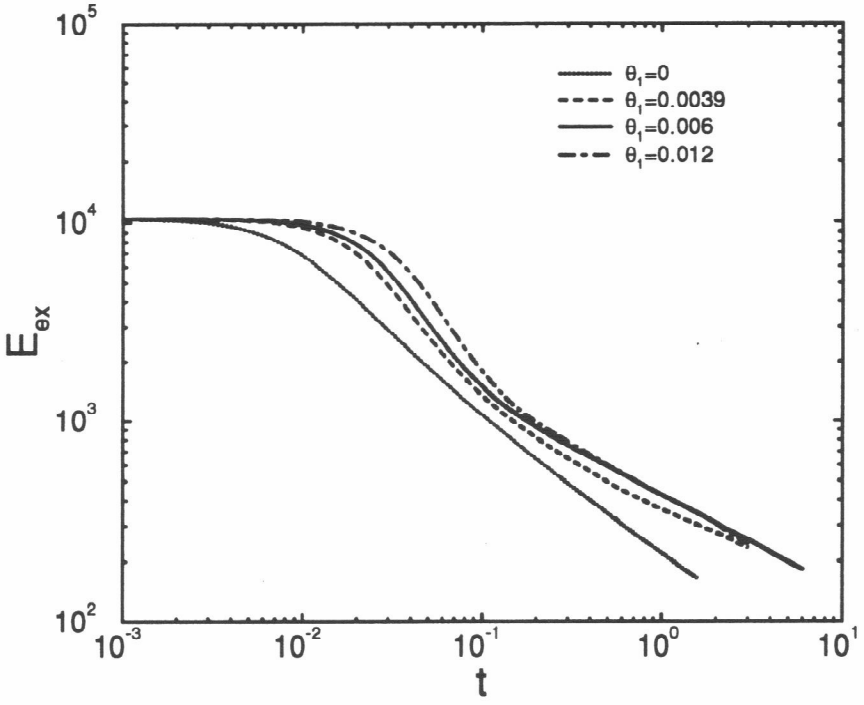

Figure 7.4: Exchange energies E_{ex} for runs with Skyrme-term amplitudes $\theta_1 = 0$, 0.0039, 0.006, and 0.012.

to the usual case of dynamical scaling, however, these characteristic length scales have distinct growth exponents. We shall refer to this situation as "multi-scaling" in the present section; in fact, it will be seen that a good correspondence holds to what is usually called multi-scaling in *equilibrium* statistical physics.

In the system with a non-zero Skyrme term, we saw in the previous section that at least one of the growth exponents—corresponding to the exchange energy E_{ex}—changed significantly compared to the non-Skyrme $O(3)$ σ-model case. Rather than just repeating the analysis of the correlation lengths—which is of limited use as the correlation functions do not collapse, leading to ambiguities in the definition of the corresponding characteristic length scales—we now attempt to develop a different

general method for characterizing multi-scaling in phase-ordering systems. In the present section we apply this method to the two-dimensional $O(3)$ σ-model with and without Skyrme term, and in Sec. 7.6 we give a more general discussion of its usefulness for the study of phase ordering in other systems.

We are motivated by the techniques used to study multi-scaling in equilibrium and steady states. Recall that a fractal system [12] is characterized by self-similarity and the lack of a characteristic length scale in the system. This leads to non-trivial power-law scaling of appropriate quantities in terms of the measuring length scale l ("the yardstick"). A *multifractal* system [13] can be characterized through anomalous scaling properties of the various moments of the investigated quantities. A well-known physical example is that of the scaling of the moments of the velocity gradients (in the inertial range) in hydrodynamic turbulence [14]. Here the n^{th} moment of the velocity gradient (averaged over the whole system) scales as l^{ϕ_n}, where l is the length scale on which the gradient is measured. There are indications that ϕ_n is not directly proportional to n in turbulent systems (thus violating the well-known Kolmogorov scaling form $\phi_n = n/3$). The system can then be characterized as a multifractal, and appropriate techniques, such as the "$f(\alpha)$ spectrum" [15, 16], may be used to study it's physical properties, starting from the information about the values of ϕ_n. In the case of phase-ordering kinetics, the system of course does not, at any given time, have a fractal or multifractal character. However, the system is characterized by growing values of the characteristic length scales (such as the correlation length of the order parameter) as the system evolves. If dynamical scaling is violated, and multiple characteristic length scales growing differently in time occur, one may expect that the techniques of multifractal analysis may be useful, if one replaces the "measuring yardstick" l by the inverse time $1/t$ elapsed since the quench.

This leads us to consider the scaling, *in time*, of the various *moments* of a suitable quantity in our evolving system. The natural quantity to investigate in the context of the $O(3)$ σ-model is the topological charge density $q(\mathbf{r})$. We define the set of

exponents β_n by the relation

$$\langle |q(\mathbf{r},t)|^n \rangle \sim t^{-\beta_n}\,, \tag{7.6}$$

where $\langle \cdots \rangle$ denotes, as usual, spatial averaging over the whole system at the time t after the quench. Since $q(\mathbf{r},t)$ is a density in a two-dimensional system, exponents characterizing the growth of a length scale may be extracted as $\beta_n/2n$. For a system characterized by a *single* length-scale, we therefore expect

$$\beta_n = 2n\phi\,, \tag{7.7}$$

where ϕ is the growth exponent as usually defined in phase ordering. For systems with multiple characteristic length scales, deviations from a straight line are expected in the β_n curve. The precise connection between the shape of the β_n curve and the property of dynamical scaling as usually defined in phase ordering will be clarified later in this section and in Sec. 7.6.

In Fig. 7.5, we show the results for the β_n curve in the pure $O(3)$ σ-model, obtained from the same simulation runs as those analyzed in the previous chapter. [The data shown are for n in the range $-1/2 \leq n \leq 10$; we have also calculated $\langle |q(\mathbf{r},t)|^n \rangle$ for even lower negative n values, but found that the statistical error of the corresponding β_n exponent diverges for $n \leq -1$.] Not surprisingly, the β_n curve obtained deviates from a straight line. A striking feature, however, is that while for low moments ($n < 2$), the relation $\beta_n = n/3$ holds at least approximately [corresponding to the power law $E_{\rm ex} \sim t^{-2/3}$ exhibited in Fig. 4 of the previous chapter], the β_n curve *saturates* and approaches a constant value of approximately 1.5 for high moments n. This is also seen directly in Fig. 7.6, showing $\langle |q(\mathbf{r},t)|^n \rangle$ as a function of time for $n \geq 1$ — the curves with the highest n values are approximately parallel to each other in the log-log plot.

As the high moments of $q(\mathbf{r})$ are dominated by regions where the topological charge density is large in absolute value, we may expect that the behavior of β_n at large n is strongly influenced by the single-texture (or single-antitexture) unwinding

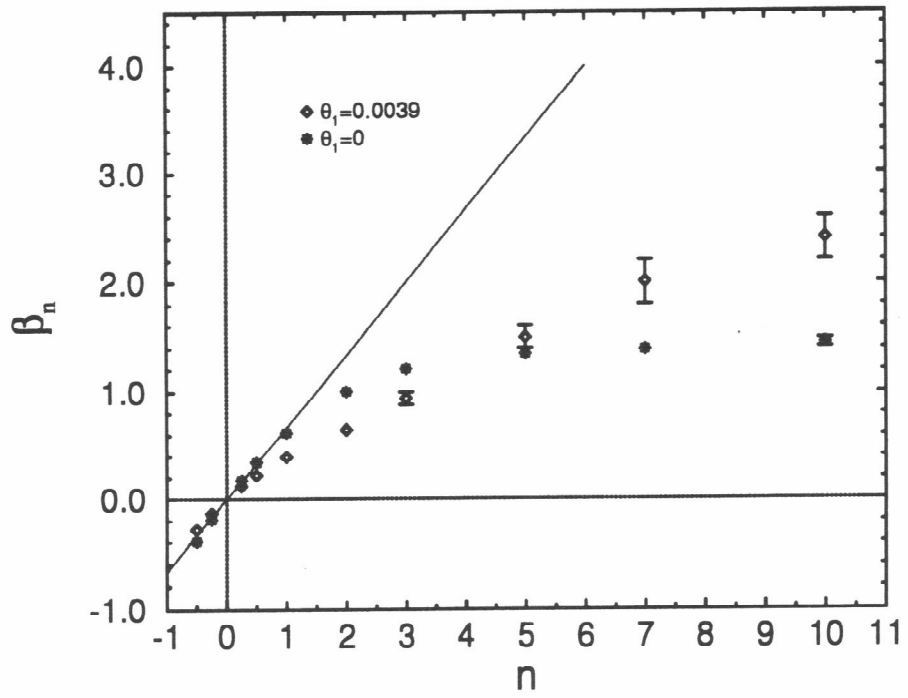

Figure 7.5: Growth exponents β_n for the n^{th} moment of the topological charge density [see Eq. (7.6)]. Shown are the β_n curves for a system with no Skyrme term (obtained by averaging over 10 runs in a 512×512 system) and with Skyrme-term amplitude $\theta_1 = 0.0039$ (obtained from a single run in a 512×512 system). The error bars are shown only when they exceed the size of the data point symbol. The full line has a slope of 2/3.

events, where $|q(\mathbf{r})|$ reaches it's maximum possible value for a short interval of time. If that is the case, we should see significant changes in the β_n curve for systems where unwindings are prevented by the Skyrme term. This is confirmed in Figs. 7.5 and 7.7, showing the β_n curve for the Skyrme term amplitudes $\theta_1 = 0.0039$ and $\theta_1 = 0.012$. It is seen that preventing the unwindings has the effect of straightening the curve, and for $\theta_1 = 0.012$, we obtain a β_n curve close to a straight line with slope 0.4, corresponding to approximate scaling with a growth exponent close to $\phi = 0.2$. Some

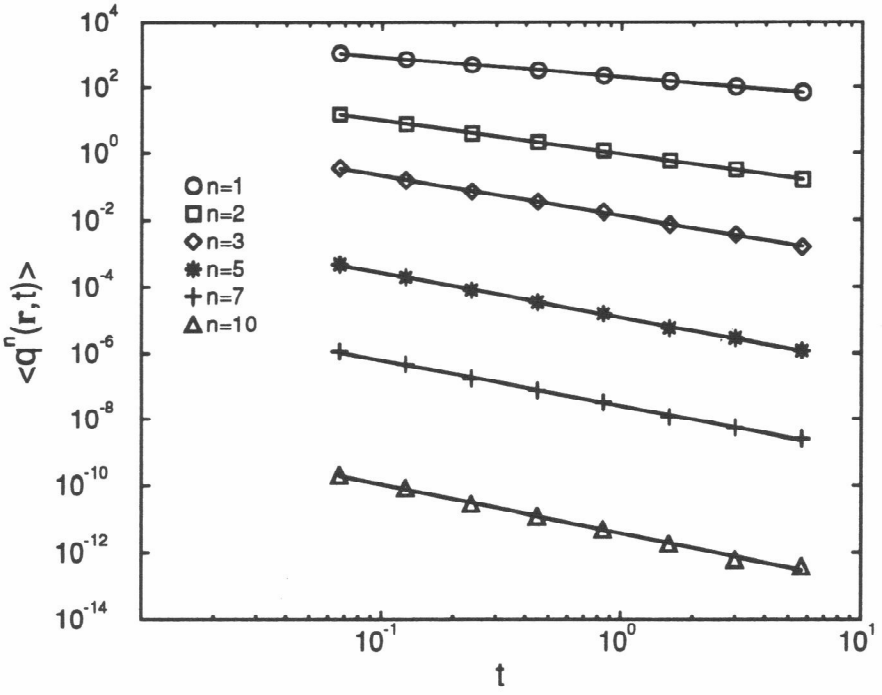

Figure 7.6: Time dependence of the moments of the topological charge density $\langle |q(\mathbf{r},t)|^n \rangle$ for $n \geq 1$ in a system with no Skyrme term. The full lines are power-law fits with exponents given in Table 7.1.

scaling violations still remain—recall that in Fig. 7.3, we observed a growth law, with exponent $\phi = 0.25 \pm 0.02$, of the length scale corresponding to the exchange energy E_{ex}. However, the extent of the scaling violations as defined by the β_n curve appears to be dramatically reduced.

The values of β_n obtained from runs in systems with Skyrme term amplitudes $\theta_1 = 0$, 0.0039, 0.006, and 0.012 are listed in Table 7.1. It appears that (at least in the runs investigated) increasing θ_1 beyond 0.006 does not significantly alter the results for β_n in the fitted time range, and that an approximately straight (rather than saturating) β_n curve is therefore a general characteristic of the regime with prevented unwindings. It is difficult to judge from only several runs of limited length if the true

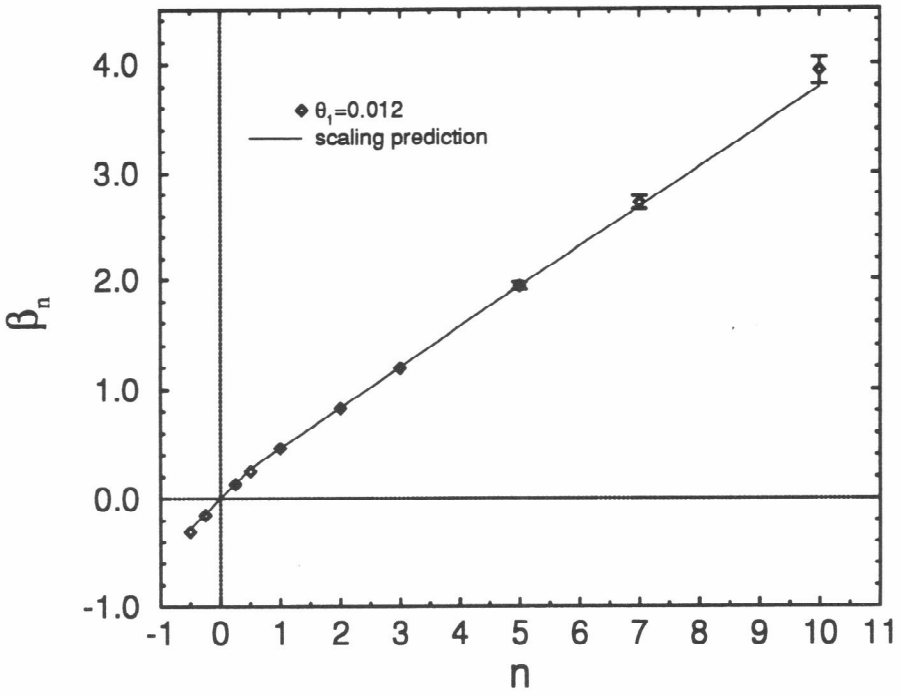

Figure 7.7: The β_n curve for $\theta_1 = 0.012$. The full line shows the two–length-scale prediction of Table 7.2 with $\phi_R = 0.185$ and $\phi_D = 0.23$.

asymptotic (late-time) β_n curve is indeed a straight line throughout the measured range of n. In fact, we shall argue below that it consists of two straight segments with differing slopes.

In Ref. [1], the second ($n = 2$), as well as the first ($n = 1$), moments of the topological charge density were calculated, and a simple two–length-scale picture for relating the values of their growth exponents to the growth exponents of the correlation lengths was developed. We now generalize the scaling argument given in [1] to obtain a prediction for the shape of the β_n curve investigated in this section. The arguments given below are independent of any information about the correlation functions. In Sec. 7.5, we shall attempt to relate the conclusions of this section to the

Table 7.1: Growth exponents β_n [defined in Eq. (7.6)] for the indicated values of the Skyrme-term amplitude θ_1. The errors stated correspond to the standard error of the least squares fitting procedure in the power-law regime in each indicated run. For $\theta_1 = 0$, the results were obtained from averaging over 10 runs in a system of size 512×512 up to $t = 5.6$. For each of the remaining θ_1 values, only one run was performed.

n	β_n for $\theta_1 = 0$	β_n for $\theta_1 = 0.0039$	β_n for $\theta_1 = 0.006$	β_n for $\theta_1 = 0.012$
-0.5	0.390 ± 0.005	0.28 ± 0.01	0.32 ± 0.02	0.31 ± 0.01
-0.25	0.190 ± 0.002	0.135 ± 0.004	0.155 ± 0.005	0.147 ± 0.006
0.25	0.177 ± 0.002	0.121 ± 0.001	0.137 ± 0.003	0.133 ± 0.005
0.5	0.340 ± 0.003	0.225 ± 0.001	0.254 ± 0.005	0.25 ± 0.01
1	0.621 ± 0.005	0.388 ± 0.002	0.447 ± 0.007	0.46 ± 0.01
2	1.004 ± 0.007	0.65 ± 0.02	0.78 ± 0.01	0.83 ± 0.02
3	1.21 ± 0.01	0.94 ± 0.06	1.15 ± 0.01	1.19 ± 0.02
5	1.35 ± 0.02	1.5 ± 0.1	1.93 ± 0.04	1.94 ± 0.03
7	1.39 ± 0.02	2.0 ± 0.2	2.7 ± 0.2	2.72 ± 0.06
10	1.45 ± 0.04	2.4 ± 0.2	3.8 ± 0.6	3.9 ± 0.1

data for the order parameter and topological charge correlations.

Picture the system as divided into regions of size D, each containing a texture or anti-texture of size R. Figures 1 of the present and previous chapters suggest that at late times such a picture is qualitatively correct. As a first approximation, let us represent each texture as a circle of radius R, with constant topological charge density $q = 1/\pi R^2$ inside the circle, and $q = 0$ outside the circle. The n^{th} moment ($n > 0$) of the topological charge density per unit area is then given by $\pi R^2 (1/\pi R^2)^n / D^2$, and scales as $R^{2-2n} D^{-2}$. We now show that provided $n > 1/2$, this scaling result is unaffected by allowing for a smooth profile of the texture. Inside each region of size D, we have a texture with topological charge density profile approximately given by

the ideal Belavin-Polyakov solution [17] for an isolated texture centered at $r = 0$:

$$q(\mathbf{r}) = \frac{1}{\pi} \frac{4R^2}{(r^2 + 4R^2)^2} \,. \tag{7.8}$$

The n^{th} moment of $q(\mathbf{r})$ per unit area is now given (omitting time-independent multiplicative factors) by $D^{-2} R^{2n} \int_0^D r\, dr\, (r^2 + 4R^2)^{-2n}$. For $n > 1/2$, the integral is dominated by the regions of small r, so that we may replace D by ∞ in the upper bound and obtain $\int_0^\infty r\, dr\, (r^2 + 4R^2)^{-2n} \sim R^{-4n+2}$, giving the previously derived scaling result $\langle |q(\mathbf{r}, t)|^n \rangle \sim R^{2-2n} D^{-2}$. For $n < 1/2$, on the other hand, the integral $\int_0^D r\, dr\, (r^2 + 4R^2)^{-2n}$ is dominated by the large-r regions, and the length scale determining it's scaling is the upper cutoff D, giving $\langle |q(\mathbf{r}, t)|^n \rangle \sim R^{2n} D^{-4n}$. In the marginal case, $n = 1/2$, we obtain $\int_0^D r\, dr\, (r^2 + 4R^2)^{-1} \sim \log(D/R)$, and consequently $\langle |q(\mathbf{r}, t)|^{1/2} \rangle \sim R D^{-2} \log(D/R)$.

The scaling arguments given above is applicable to the configuration of a system at any given time t. If we now *assume* that the length scales D and R grow as power-laws with exponents ϕ_{D} and ϕ_{R}, i.e.,

$$D(t) \sim t^{\phi_{\text{D}}} \quad \text{and} \quad R(t) \sim t^{\phi_{\text{R}}} \,, \tag{7.9}$$

and use the scaling expressions from the previous paragraph, then we obtain the following predictions for the exponent β_n for the growth of $\langle |q(\mathbf{r}, t)|^n \rangle$: $\beta_n = 2n\phi_{\text{R}} + 2(\phi_{\text{D}} - \phi_{\text{R}})$ for $n > 1/2$, and $\beta_n = n(4\phi_{\text{D}} - 2\phi_{\text{R}})$ for $n < 1/2$. In the case $n = 1/2$, simple power-counting gives $\beta_{1/2} = 2\phi_{\text{D}} - \phi_{\text{R}}$; however, at any finite t the presence of the logarithmic term $\log(D/R) \sim \log(t)$ will tend to suppress the effective growth exponent below the true asymptotic value of $2\phi_{\text{D}} - \phi_{\text{R}}$. [Note that for the consistency of this argument, and some other arguments given above, it is necessary to assume that the characteristic separation $D(t)$ between textures grows (at least asymptotically) *faster* than the characteristic texture size $R(t)$; it is seen from Figs. 1 of the present and previous chapter that such an assumption is indeed justified.]

Our predictions based on the two–length-scale picture are summarized in Table 7.2. In order to compare these predictions to the measured β_1 curves, we proceed as

Table 7.2: Predictions for the scaling of the moments of the topological charge density based on the two–length-scale argument [see the text following Eq. (7.8)]. The second column gives the scaling of the n^{th} moment of topological charge density in terms of the characteristic separation D between textures and the characteristic texture size R; the third column gives the growth exponent β_n defined by Eq. (7.6), assuming that the length scales D and R scale according to Eq. (7.9).

moment	scaling in terms of R, D	β_n value in terms of $\phi_{\rm D}$, $\phi_{\rm R}$
$n > 1/2$	$R^{2-2n}D^{-2}$	$2n\phi_{\rm R} + 2(\phi_{\rm D} - \phi_{\rm R})$
$n = 1/2$	$D^{-2}\log(D/R)$	$\leq 2\phi_{\rm D} - \phi_{\rm R}$
$n < 1/2$	$R^{2n}D^{-4n}$	$n(4\phi_{\rm D} - 2\phi_{\rm R})$

follows. We first calculate the exponents $\phi_{\rm D}$ and $\phi_{\rm R}$ from the measured β_n values for two selected moments n, and then check how the remaining β_n values compare with the predictions of Table 7.2. The most natural moment to use to obtain $\phi_{\rm D}$ is $n = 1$: by definition, $\langle |q(\mathbf{r}, t)| \rangle$ gives the number of textures and antitextures in the system (assuming that no multiply-charged topological objects occur), and consequently the growth exponent for the average texture (or antitexture) separation $D(t)$ is given by $\phi_{\rm D} = \beta_1/2$. Which value of n should be used to obtain $\phi_{\rm R}$ is a matter of choice; we use $n = 2$, i.e., we take $\phi_{\rm R} = (\beta_2 - 2\phi_{\rm D})/2$. It is expected that the half-widths $L_{\rm q}$ and $L_{\rm p}$ of the topological correlation functions $C_{\rm q}(r, t)$ and $C_{\rm p}(r, t)$ should provide a good indication of the characteristic texture size, and their scaling can therefore be used as a check of consistency.

We first apply this approach to the runs with single-texture unwindings prevented. We use the values of β_n measured in the system with Skyrme term amplitude $\theta_1 = 0.012$ (Table 7.1). We obtain $\phi_{\rm D} \simeq 0.46/2 = 0.23$ and $\phi_{\rm R} \simeq (0.83 - 20.23)/2 = 0.185$. Using these values in the expressions for β_n given in Table 7.2 yields the full curve shown in Fig. 7.7. A very good agreement with the the data for β_n is observed throughout the measured n range. Note that the measured value $\beta_{1/2} = 0.25 \pm 0.01$ is slightly lower than the predicted value of 0.275, as expected from the influence of

the logarithmic term in $\langle |q(\mathbf{r},t)|^{1/2} \rangle \sim R(t) D^{-2}(t) \log[D(t)/R(t)]$.

The predictions of Table 7.2, however, are not consistent with the β_n data for the pure $O(N)$ σ-model with no Skyrme term. It is clear that the $n > 1/2$ prediction $\beta_n = 2n\phi_{\rm R} + 2(\phi_{\rm D} - \phi_{\rm R})$ can agree with the saturating curve in Fig. 7.5 only if $\phi_{\rm R} = 0$; this is, however inconsistent with the data for lower n. [Proceeding as in the $\theta_1 = 0.012$ case, we would obtain $\phi_{\rm D} \simeq 0.621/2 = 0.31$ and $\phi_{\rm R} \simeq (1.004 - 20.31)/2 = 0.19$, resulting in a slope of the β_n curve at high n comparable to the $\theta_1 = 0.012$ case.] To resolve this apparent contradiction, we now discuss the effects of having a *distribution* of texture sizes R. In general, we may expect that a stationary distribution $H(R)$ of texture sizes develops in the asymptotic ordering regime. By stationary, we mean that $H(R(t), t)$ depends on t only through the time-dependence in $R(t)$. Let us assume, for the moment, that $H(R)$ is a power-law, i.e., $H(R) \sim R^{\alpha}$. There are no textures smaller than the lattice size, or in general, the coherence length of the order parameter. We shall denote this ultra-violet cutoff length scale by ξ. The natural upper (infra-red) cutoff scale for the texture distribution is given by D. By using the results in Table 7.2 separately for each single-texture region, we obtain

$$\langle |q(\mathbf{r},t)|^n \rangle \sim \int_{\xi}^{D} dR\, H(R)\, R^{2-2n}\, D^{-2} \sim D^{-2} \int_{\xi}^{D} dR\, R^{\alpha-2n+2}\,, \quad \text{for} \quad n > 1/2\,; \tag{7.10}$$

$$\langle |q(\mathbf{r},t)|^n \rangle \sim \int_{\xi}^{D} dR\, H(R)\, R^{2n}\, D^{-4n} \sim D^{-4n} \int_{\xi}^{D} dR\, R^{\alpha+2n}\,, \quad \text{for} \quad n < 1/2\,. \tag{7.11}$$

It is evident that for *any* value of α, there exist sufficiently large positive values of n such that the integral over R in Eq. (7.10) is dominated by *small* textures. In that case (i.e., for $n > \max[1/2, (\alpha+3)/2]$), we obtain $\langle |q(\mathbf{r},t)|^n \rangle \sim D^{-2}(\xi^{-(2n-\alpha-3)} - D^{-(2n-\alpha-3)}) \sim D^{-2}$ (recall that ξ is independent of t, and can be therefore treated as a constant in our scaling arguments).

The saturation of the β_n curve at large n in Fig. 7.5 can be therefore understood as a consequence of the texture distribution being dominated by textures of the smallest possible sizes. For this argument, it is immaterial whether the $H(R)$ distribution has precisely a power-law form, as assumed above, or not. In essence, we simply apply the prediction of Table 7.2 for $n > 1/2$, but replace the general texture size R by the

time-independent length scale ξ, yielding $\langle |q(\mathbf{r},t)|^n \rangle \sim D^{-2}$, and therefore $\beta_n = 2\phi_D$, independently of n. This predicts that the β_n curve for the system with no Skyrme term should saturate at the value 0.621, while the observed β_n values in the range $5 \leq n \leq 10$ are $1.35 - 1.45$, giving a serious quantitative disagreement. One reason may be our assumption of the stationary nature of the texture-size distribution $H(R)$; for a more general form $H(t, R(t))$, it is possible to obtain an asymptotic value of β_n higher than $2\phi_D$, if the relative proportion of textures of the smallest size increases with t. (See Sec. 7.6 for an example where arguments analogous to those given in the previous two paragraphs lead to a somewhat better agreement with simulation results.)

It is interesting to note that for very *low* moments, satisfying the condition $n < (\alpha - 1)/2$, Eq. (7.11) implies the scaling relation $\langle |q(\mathbf{r},t)|^n \rangle \sim D^{-4n}$. This can be expected to be relevant mainly for large negative values of n; we find, however, that the exponent β_n is not well defined for $n \leq -1$, due to the domination of $\langle |q(\mathbf{r},t)|^n \rangle$ by small $q(\mathbf{r})$ fluctuations, leaving us unable to check such a scaling law. In the range $(\alpha - 1)/2 < n < \max[1/2, (\alpha + 3)/2]$, it is easy to see that Eqs. (7.10,7.11) imply the scaling form $\langle |q(\mathbf{r},t)|^n \rangle \sim D^{\alpha - 2n + 1}$. The values of β_n for $n = 0.25$ and $n = 0.5$ from the $\theta_1 = 0$ column of Table 7.2 are well fit by taking $\alpha = -1$ and $\phi_D = 1/3$ (see the straight line in Fig. 7.5). Such value of α would imply saturation of the β_n curve for moments $n > \max[1/2, (\alpha + 3)/2] = 1$; it is seen in Fig. 7.5 that the crossover to saturation indeed starts at $n \simeq 1$. Note, however, that $\alpha = -1$ would also imply $\langle |q(\mathbf{r},t)|^n \rangle \sim D^{-4n}$ for all $n < 0$, which is not observed. This again suggests that although the arguments leading to Eqs. (7.10,7.11) are useful on a qualitative level, our *Ansatz* $H(R) \sim R^\alpha$ for the texture size distribution is inadequate.

The analysis presented in Secs. 7.3 and 7.4 suggests the following overall picture of phase ordering in our implementation of the two-dimensional $O(3)$ σ-model. With no Skyrme term ($\theta_1 = 0$), textures (or antitextures) are not prevented from unwinding, sharp jumps by ± 1 are observed in the time dependence $Q(t)$ of the topological charge, and the occurrence of textures with size $R \simeq \xi$ is necessarily reflected in the saturation

of the β_n curve for sufficiently high positive moments n. With a sufficiently strong Skyrme term ($\theta_1 = 0.006$ or 0.012), the singular unwinding events are prevented, and phase ordering proceeds purely through the annihilation of regions of positive and negative topological charge density. No small textures occur, the average texture size $R(t)$ is sharply defined, and the two–length-scale arguments resulting in the predictions of Table 7.2 may be used. For intermediate θ_1 values ($\theta_1 = 0.0036$), it is difficult to analyze our data in terms of either one of these scenarios; it is possible that at sufficiently late times, a crossover to either the unwinding-free or the unwinding-dominated regime will always occur.

7.5 Scaling of the correlation functions.

To test whether the straightening of the β_n curve occurring for sufficiently large Skyrme-term amplitudes θ_1 can be identified with improved scaling in the standard sense, we have calculated the correlation functions of the order parameter and the topological charge for the run with $\theta_1 = 0.012$. The results of our attempt to collapse the data for the correlation functions at different times are shown in Fig. 7.8, with the correlation functions $C(y)$, $C_{\mathrm{q}}(y)$, and $C_{\mathrm{p}}(y)$ defined as in the previous chapter. The correlation functions are taken at somewhat later times than those in Fig. 5 of the previous chapter (where analogous results for the case $\theta_1 = 0$ were presented), as the power-law regime, where scaling may be expected to hold, starts only after $t = 0.2$ in the $\theta_1 = 0.012$ case. From a comparison of the two figures, we see that, somewhat surprisingly, the quality of collapse of any of the correlations is not improved in the Skyrme case (even taking into account the fact that data in Fig. 7.8 are obtained from just one run, while the data in Fig. 5 of the previous chapter were obtained by averaging over 14 runs). The strongest violation of scaling is again observed in the topological correlation function C_{q}.

As seen in the inset to Fig. 7.8, the length scales $L(t)$, $L_{\mathrm{q}}(t)$, and $L_{\mathrm{p}}(t)$ appear to be well fit by the form $L(t) = a\log(bt)$ throughout a wide time range. It is

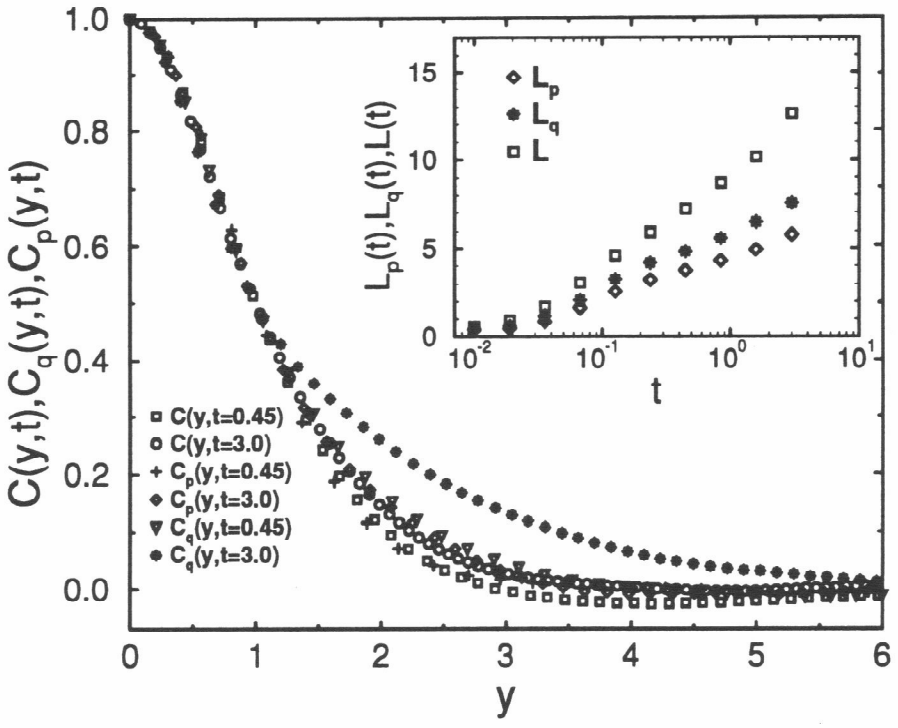

Figure 7.8: The rescaled correlation functions $C(r/L(t))$, $C_{\rm q}(r/L_{\rm q}(t))$ and $C_{\rm p}(r/L_{\rm p}(t))$ at the specified times, in a system with Skyrme-term amplitude $\theta_1 = 0.012$. Inset: the half-widths $L(t)$, $L_{\rm p}(t)$ and $L_{\rm q}(t)$ on a semi-logarithmic scale.

difficult, however, to distinguish logarithmic growth from a power-law growth with a small exponent; in fact, the half-widths $L_{\rm p}(t)$ and $L_{\rm q}(t)$ of the topological correlation functions in a system with no Skyrme term were fit to a power-law form in Ref. [1], and it was found that at very late times their growth was consistent with the power law $t^{0.21\pm0.02}$. In Fig. 7.9, we re-plot the data from the inset of Fig. 7.8 on a log-log scale. It appears that a well-defined crossover to a power-law regime for all three length scales occurs at time $t \simeq 0.2$. While the logarithmic form seems to fit the data for $L(t)$, $L_{\rm q}(t)$, and $L_{\rm p}(t)$ better in the intermediate time range, the coincidence of the crossover location $t \simeq 0.2$ with the beginning of the unwinding-free regime (see Sec. 7.3) suggests that the crossover is physical, and that the power-law growth

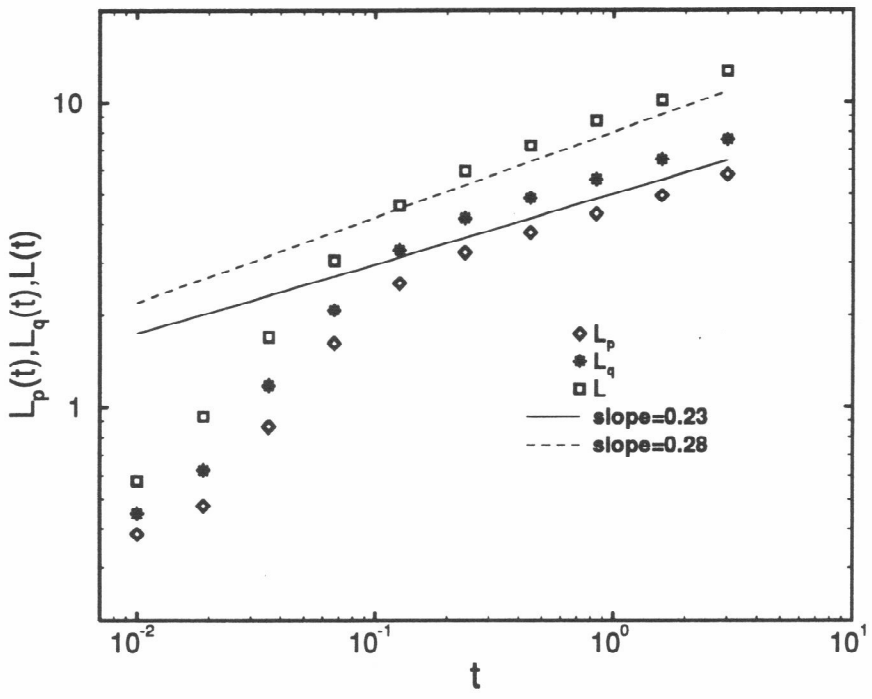

Figure 7.9: The half-widths $L(t)$, $L_{\mathrm{p}}(t)$ and $L_{\mathrm{q}}(t)$ from Fig. (7.8) on a log-log scale. The straight lines have slopes 0.23 (full line) and 0.28 (dashed line).

with global exponent $\phi_{\mathrm{C}} = 0.28 \pm 0.03$, observed in Fig. 7.9, should be taken as an indication of the true asymptotic behavior of $L(t)$. For the length scales $L_{\mathrm{p}}(t)$ and $L_{\mathrm{q}}(t)$, we obtain in a similar way an asymptotic power-law growth with exponents $\phi_{L_{\mathrm{p}}} = \phi_{L_{\mathrm{q}}} = 0.22 \pm 0.03$.

It is tempting to identify the half-width L_{q} of the correlation function $C_{\mathrm{q}}(r,t)$ for the topological charge density with the typical size of a texture or antitexture in the system. Such a relation can be expected to be valid if $C_{\mathrm{q}}(r,t)$ is strongly dominated by the well-separated regions of maxima or minima of $q(\mathbf{r})$ (i.e., the central regions of textures or antitextures). The regions in between the textures, containing fluctuations of positive and negative $q(\mathbf{r})$, however, also contribute to $C_{\mathrm{q}}(r,t)$. At late times, the

typical magnitude of $q(\mathbf{r})$ in those regions is much smaller than in the texture peaks—on the other hand, those regions occupy an increasing proportion of the system area. The relation of L_{q} to the characteristic texture size R is therefore not entirely clear. With this caveat, we may attempt to identify the growth exponent ϕ_{R} used in the previous section with the growth exponent for $L_{\mathrm{p}}(t)$ [or $L_{\mathrm{q}}(t)$]. The obtained value of 0.22 ± 0.03 is in only approximate agreement with the value $\phi_{\mathrm{R}} = 0.185$ that was independently given by our analysis of the β_n curve data. It is interesting to note, however, that the same values of $\phi_{L_{\mathrm{q}}}$ and $\phi_{L_{\mathrm{p}}}$ are obtained in the $O(3)$ model case with no Skyrme term [1]. This suggests that although (as demonstrated in Sec. 7.4) the distribution of texture sizes in the $\theta_1 = 0$ and $\theta_1 > 0$ cases is significantly different, the "typical" texture size behaves in a rather similar way in both cases.

A further indication of the different character of the texture size distribution in the non-Skyrme $O(N)$ system and the Skyrme system is provided by our data for the structure factor $S(k,t)$ [the Fourier transform of the order parameter correlation function $C(r,t)$]. While the large-k region of $S(k,t)$ in the system with $\theta_1 = 0$ can be approximately fit by a power law $S(k) \propto k^{-\chi}$ with the Porod exponent $\chi = 6 \pm 1$ [18], the asymptotic structure factor in the system with $\theta_1 = 0.012$ is approximately fit by an exponential form, $S(k,t) \propto e^{-a(t)k}$. This agrees with our picture of the texture size distribution being dominated by very small textures for $\theta_1 = 0$ (leading to a singularity in the short-range order parameter correlation, analogously to systems with singular topological defects [19]), and with the expectation that for $\theta_1 = 0.012$, there are no textures of size comparable to the lattice spacing.

7.6 The β_n curve and dynamical scaling in general.

In Sec. 7.4, we saw that studying the growth exponents β_n for the moments $\langle |q(\mathbf{r},t)|^n \rangle$ of the topological charge density yielded useful information on the short-scale properties of the system and on the distribution of the sizes of topological textures and antitextures during the phase ordering process. We now discuss in greater generality

the usefulness of the method, and possible applications of it to other phase ordering systems.

We saw that the shape of the β_n curve depended dramatically on the value of the Skyrme-term amplitude θ_1, with β_n saturating at a finite value for large positive n in the $\theta_1 = 0$ case, but growing indefinitely and approaching a straight line with a well-defined slope in the $\theta_1 = 0.012$ case. At the same time, we concluded in Sec. 7.5 that the straightening of the β_n curve was not associated with an improved quality of collapse of the correlation functions. In what sense, then, is measuring the β_n curve a useful diagnostic for the investigation of dynamical scaling ?

Let us first define β_n in an alternative way, applicable to any phase-ordering system. The topological charge density $q(\mathbf{r})$ is a meaningful quantity only in the two-dimensional $O(3)$ model (or in general, in an $O(N)$ model in dimension $d = N-1$); for a general system, it is natural to consider instead the usual form of the inhomogeneous part of the *free energy density*, given by $e(\mathbf{r}, t) \equiv |\nabla \mathbf{m}(\mathbf{r}, t)|^2$ in the case of an $O(N)$ order parameter. We now define the set of exponents β_n through

$$\langle |\nabla \mathbf{m}(\mathbf{r}, t)|^{2n} \rangle \sim t^{-\beta_n} . \tag{7.12}$$

[Recall that in the case of the two-dimensional $O(3)$ model, the topological charge density $q(\mathbf{r})$ and the "exchange" energy density $e(\mathbf{r})$ are closely related in the late stages of ordering; either quantity can be used for the β_n-curve analysis in this model. The scaling arguments presented in Sec. 7.4 were based on the single texture profile Eq. (7.8); the profile of the energy density $e(r)$ has an identical form [17], and none of the scaling arguments developed by us is therefore altered if we use the definition Eq. (7.12).]

It is clear that for large positive n, the β_n values are determined primarily by the regions with large order parameter gradients, while for $n < 1$ (and particularly for $n < 0$), regions where the order parameter varies slowly contribute the most. The β_n curve, as a whole, probes the entire range of length scales that characterize the system. The saturation of β_n for high n is expected to occur if a short *time-independent* length

scale comes into play. We saw a corresponding example in Sec. 7.4, where such a length scale was the minimum possible texture size, approximately given by one lattice spacing. Generally, in any system where singularities of the order parameter occur—meaning that significant variations of the order parameter are present on the scale of the (time-independent) order parameter coherence length—a saturation of the β_n curve is expected. In addition to the system with unwinding textures, this will occur in any system with stable topological defects.

To illustrate this, we calculated the β_n exponents as defined by Eq. (7.12) for the case of a two-dimensional uniaxial nematic. Phase ordering in such a system was studied in detail in [20]; it was shown that the system orders through the mutual annihilation of numerous point defects, and the average defect separation $D(t)$ was found to grow as $t^{0.374\pm0.005}$ in the time range investigated. By using the simulation method described in [20], we have calculated the β_n curve in a system of size 256×256, averaged over 20 configurations. The result is seen in Fig. 7.10; the β_n curve apparently approaches saturation, and the β_n values for $2 \leq n \leq 10$ are in the range $0.8 - 1.05$. The two–length-scale analysis given for textures in Sec. 7.4 is easily modified for the present case: instead of Eq. (7.8), we now have the divergent profile of energy density $e(r)$ around a point defect given by $e(r) \sim 1/r^2$; for all $n > 1$, this implies that the integral in $\langle e(\mathbf{r},t)^n \rangle \sim D^{-2} \int_\xi^D r\, dr\, r^{-2n}$ is dominated by the lower cut-off region $r \simeq \xi$, where ξ is the defect core size, and is therefore time-independent. This leads to $\beta_n = 2\phi_{\rm D} = 0.75 \pm 0.01$ for $n > 1$, which is not far from the observed values. For $n < 1$, we obtain the "usual" scaling prediction $\beta_n = 2n\phi_{\rm D}$, which is seen to agree approximately with the data. A crossover between the two regimes occurs at $n \simeq 1$; the value of β_1 is affected by the logarithmic correction in $\langle e(\mathbf{r},t) \rangle \sim D(t)^{-2} \log[D(t)/\xi]$.

In any system with stable topological defects (having a time-independent core size), we will similarly obtain (for all n higher then some threshold value n_s) the saturation of the β_n curve at $\beta_n = d\phi_{\rm D}$, where d is the dimensionality of the system and $\phi_{\rm D}$ is the growth exponent for the average separation between defects. Such

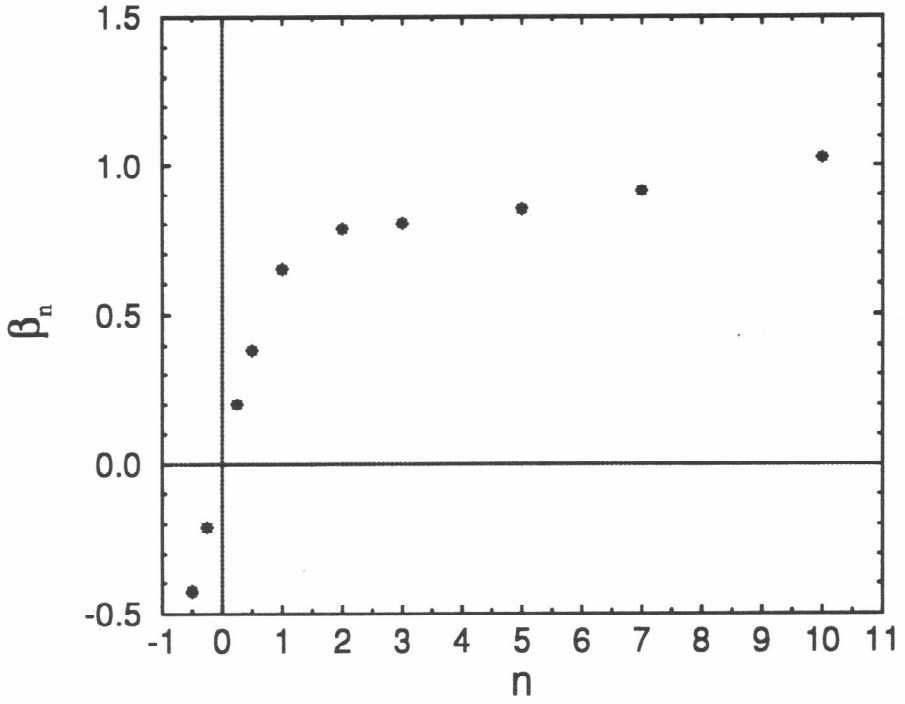

Figure 7.10: Growth exponents β_n for the n^{th} moment of the energy density in a two-dimensional uniaxial nematic, obtained from averaging over 20 configurations in a 256×256 system.

saturation should not be taken as an indication of a violation of dynamical scaling. For all $n < n_s$, however, the standard one–length-scale prediction $\beta_n = nd\phi_{\text{D}}$ is obtained; any observed deviation from this prediction would indicate the violation of dynamical scaling.

In any system with topological textures, an analysis similar to that carried out in Sec. 7.4 will lead to non-trivial predictions with at least two time-dependent length scales. In addition, if texture unwindings occur, the β_n curve will saturate at a high enough n. We can therefore expect no saturation for textures in spatial dimension $d = 1$, which are unstable towards expansion; saturation is expected for textures in $d = 3$ and higher, where textures are unstable towards collapse.

In systems with no topological objects, the β_n exponents cannot be predicted using the type of arguments developed by us in this chapter, as no direct analogs of the length scales D or R exist. However, it is not expected that the β_n curve will saturate, and a system satisfying dynamical scaling should therefore obey $\beta_n \sim n$ for all n. It would be interesting to see how the violations of dynamical scaling that were shown to occur in the conserved spherical model [21] are reflected in the shape of the corresponding β_n curve.

References

[1] A. D. Rutenberg, Phys. Rev. E **51**, R2715 (1995).

[2] B. M. A. G. Piette, B. J. Schroers, and W. J. Zakrzewski, Z. Phys. C **65**, 165 (1995).

[3] N. S. Manton, Commun. Math. Phys. **111**, 469 (1987).

[4] T. H. R. Skyrme, Proc. R. Soc. A **260**, 127 (1961).

[5] G. H. Derrick, J. Math. Phys. **5**, 1252 (1964).

[6] To avoid confusion, we note that an alternative expression for the Skyrme energy density, namely, $(\partial_x \mathbf{m}\cdot\partial_x \mathbf{m})(\partial_y \mathbf{m}\cdot\partial_y \mathbf{m}) - (\partial_x \mathbf{m}\cdot\partial_y \mathbf{m})^2$, was used in Refs. [2, 7, 8, 9]. This form is immediately obtained from our form $[(\partial_x \mathbf{m}\times\partial_y \mathbf{m})]\cdot[(\partial_x \mathbf{m}\times\partial_y \mathbf{m})]$ by applying the identity $[\mathbf{A}\times\mathbf{B}]\cdot[\mathbf{C}\times\mathbf{D}] = (\mathbf{A}\cdot\mathbf{C})(\mathbf{B}\cdot\mathbf{D}) - (\mathbf{A}\cdot\mathbf{D})(\mathbf{B}\cdot\mathbf{C})$.

[7] B. M. A. G. Piette, B. J. Schroers, and W. J. Zakrzewski, Nucl. Phys. B **439**, 205 (1995).

[8] N. Papanicolaou and W. J. Zakrzewski, Physica D **80**, 225 (1995).

[9] N. Papanicolaou and W. J. Zakrzewski, Phys. Lett. A **210**, 328 (1996).

[10] A. D. Rutenberg, W. J. Zakrzewski, and M. Zapotocky (unpublished).

[11] S. L. Sondhi, A. Karlhede, S. A. Kivelson, and E. H. Rezayi, Phys. Rev. B **47**, 16419 (1993).

[12] B. B. Mandelbrot, *The Fractal Geometry of Nature* (W. H. Freeman, New York, 1982).

[13] See, e.g., G. Paladin and A. Vulpiani, Phys. Rep. **156**, 147 (1987).

[14] See, e.g., U. Frisch, *Turbulence : the legacy of A. N. Kolmogorov* (Cambridge University Press, Cambridge, 1995).

[15] U. Frisch and G. Parisi, in *Turbulence and Predictability in Geophysical Fluid Dynamics and Climate Dynamics*, edited by M. Ghil, R. Benzi and G. Parisi (North Holland, Amsterdam, 1985), pp. 84-88.

[16] T. C. Halsey, M. H. Jensen, L. P. Kadanoff, I. Procaccia, and B. I. Shraiman, Phys. Rev. A **33**, 1141 (1986).

[17] See, e.g., R. Rajaraman, *Solitons and Instantons* (North Holland, Amsterdam, 1982).

[18] This is consistent with the results of the cell dynamical scheme simulation of the two-dimensional $O(3)$ model in H. Toyoki, Mod. Phys. Lett. B **7**, 397 (1993), where the value $\chi = 6.9 \pm 0.3$ was obtained.

[19] A. J. Bray and K. Humayun, Phys. Rev. E **47**, 9 (1993); see also Sec. IV.D in A. D. Rutenberg and A. J. Bray, Phys. Rev. E **51**, 5499 (1995), for a discussion of the structure factor tail in systems with topological textures.

[20] M. Zapotocky, P. M. Goldbart and N. Goldenfeld, Phys. Rev. E **51**, 1216 (1995).

[21] A. Coniglio and M. Zannetti, Europhys. Lett. **10**, 575 (1989).

Appendix A

Topological defects and the short-distance behavior of the structure factor in nematic liquid crystals

A.1 Introduction

The dynamics of ordered systems containing numerous topological defects has been the subject of much recent interest, both in the context of phase ordering dynamics in condensed matter [1, 2] and of the formation of large-scale structures in cosmological models [3, 4]. In both cases, the defects are introduced into the system during a quench from a higher-symmetry phase into a lower-symmetry phase. After the quench, the system orders primarily through the mutual annihilation of the numerous defects.

The process of phase ordering has been successfully studied experimentally in systems described by a scalar order parameter (e.g., in binary alloys—see Ref. [5]). However, analogous experiments were found to be very difficult to perform in systems with continuous symmetries (such as ferromagnets or liquid He^4). In the recent years, a series of experiments [6, 7, 8, 9] have demonstrated that nematic liquid crystals provide a system in which phase ordering (following a quench from the isotropic to the nematic phase) is accessible to experimental investigation. It is therefore of importance to extend the available theoretical results for phase ordering in $O(N)$ symmetric *vector* model systems (e.g., Refs. [10, 11, 12, 13]) to systems described by the *tensorial* nematic order parameter.

The principal quantity of interest in both the theoretical and the experimental investigations of phase ordering is the structure factor $S(\mathbf{k}, t)$, which is the Fourier transform of the real-space correlation function of the order parameter at a time t after the quench. This quantity, which is directly measurable via the appropriate scattering experiment, characterizes the degree of inhomogeneity of the order parameter at length scales of order k^{-1}.

Only approximate calculations are available for the function $S(\mathbf{k}, t)$ in systems supporting topological defects (see Refs. [10, 11] for the scalar and $O(N)$ vector models, and Ref. [16] for the uniaxial nematic case). A common feature of both the experimentally determined [8, 9] and the approximate analytical structure factors, however, is that $S(k, t)$, the average of $S(\mathbf{k}, t)$ over the orientations of $\mathbf{k}$, becomes a power-law function of k in the region of large k: $S(k, t) \sim k^{-\chi}$. In scalar systems, this power-law behavior has long been understood as arising from sharp changes in the order parameter across the domain walls present in the system [17, 18]. Recently, Bray and Humayun [13] presented purely geometric arguments showing that the power-law behavior in the $O(N)$ vector model comes from the singular variations of the order parameter in the vicinity of the defect cores. Their approach permits the determination of not only the exponent χ but also the amplitude A in the asymptotic relation $S(k, t) = A\rho(t)k^{-\chi}$, where $\rho(t)$ is the number density of topological defects at time t. Their analytical results agree well with data available from numerical simulations of phase ordering in $O(N)$ vector model systems [15].

In the present chapter, we calculate analytically the Porod-law exponents χ and amplitudes A arising from topological defects occurring in uniaxial and biaxial nematic systems in both two and three spatial dimensions. We also discuss how our results may be used to extract information about the defects present in the system and the degree of biaxiality of the nematic order parameter from the experimentally-determined structure factor. The results presented here were obtained in collaboration with Paul M. Goldbart.

This chapter is organized as follows. In Sec. A.2, we give a general discussion of

the origin of the Porod tail (i.e., the behavior for large wave vectors) of the structure factor, and briefly review the method used by Bray and Humayun [13] to calculate the Porod-law amplitudes in the $O(N)$ vector model. Then, in Sec. A.3, we re-derive their main results in a simple way, working directly in Fourier space and taking full advantage of the symmetries of the problem. In Sec. A.4 the simplified method is used to calculate the Porod tail forms corresponding to hedgehog defects, disclination lines, and ring defects in a uniaxial nematic system. A case of special interest is that of a ring defect (disclination loop) in a uniaxial nematic—in Sec. A.4.3, we show that in this case, two separate Porod regimes exist, having distinct exponents and amplitudes, arising for length scales larger than and smaller than the radius of the disclination loop. The presence of two Porod regimes is specific to the nematic case, and does not occur for ring defects in $O(N)$ vector model systems. In Sec. A.5, we generalize our results for the uniaxial nematic to the case of non-abelian defects in *biaxial* nematics, the dynamics of which has recently been investigated experimentally [20] and theoretically [19]. The Porod amplitudes depend in this case on the strength of the biaxiality of the nematic order parameter. In Sec. A.6, we point out an explicit connection between the total *elastic energy* (in the one-constant approximation) of a nematic defect and the Porod amplitude, and argue that deformations of the defect core region due to defect interactions can only *increase* this amplitude.

The results described in this chapter were obtained in collaboration with Paul M. Goldbart.

A.2 The generalized Porod law

Consider an ordered system characterized by a suitable order parameter field. Scattering experiments using an appropriate experimental probe that couples to the order parameter in question (e.g., neutron scattering for ferromagnets, or light scattering for nematics) permit one to measure directly the structure factor $S(\mathbf{k}, t)$, describing the correlations of the order parameter, via its proportionality to the scattering in-

tensity. The structure factor $S(\mathbf{k},t)$ is defined as the Fourier transform of the real space correlation function $C(\mathbf{r},t)$:

$$S(\mathbf{k},t) = \int d^d r\, e^{i\mathbf{k}\cdot\mathbf{r}}\, C(\mathbf{r},t). \tag{A.1}$$

In the case of a system described by the $O(N)$ vector model order-parameter field $\mathbf{\Phi}(\mathbf{r},t)$, the correlation function $C(\mathbf{r},t)$ is given by

$$C(\mathbf{r},t) = \frac{1}{M_{O(N)}} \int d^d x\, \mathbf{\Phi}(\mathbf{x},t)\cdot\mathbf{\Phi}(\mathbf{x}+\mathbf{r},t)\,, \tag{A.2}$$

where the integration is over the whole system. Here $M_{O(N)}$ is a normalization factor,

$$M_{O(N)} = \int d^d x\, \mathbf{\Phi}(\mathbf{x},t)\cdot\mathbf{\Phi}(\mathbf{x},t)\,, \tag{A.3}$$

to ensure that $C(\mathbf{r},t)|_{\mathbf{r}=\mathbf{0}} = 1$. Equivalently, the structure factor may be expressed as

$$S(\mathbf{k},t) = \frac{1}{M_{O(N)}} \mathbf{\Phi}(\mathbf{k},t)\cdot\mathbf{\Phi}(-\mathbf{k},t)\,, \tag{A.4}$$

where $\Phi(\mathbf{k},t)$ is the Fourier-transformed order parameter,

$$\mathbf{\Phi}(\mathbf{k},t) = \int d^d r\, e^{i\mathbf{k}\cdot\mathbf{r}} \mathbf{\Phi}(\mathbf{r},t)\,. \tag{A.5}$$

For systems that are isotropic on macroscopic scale (such as a bulk system undergoing phase ordering), $S(\mathbf{k},t)$ depends on $\mathbf{k}$ through the magnitude $k = |\mathbf{k}|$ only.

Numerous experimental and computational studies have shown that in systems that support topologically stable defects (walls, lines, or points), the structure factor $S(k,t)$ decays asymptotically as a power law in k:

$$S(k,t) \sim B(t) k^{-\chi} \quad (k \gg k_p). \tag{A.6}$$

In phase ordering systems the inverse length k_p beyond which the power-law regime is exhibited depends on the time t that has elapsed since the quench, viz., k_p decreases with increasing t. Similarly, the time-dependent amplitude B decays with t. This behavior is easily understood for systems with a *scalar* order parameter, containing

domain walls, as follows. Consider for simplicity a one-dimensional system with a kink. Viewed on length scales larger than the kink width (given by the coherence length of the order parameter), the order parameter abruptly changes from -1 to 1 at the kink location. For k values smaller than the inverse kink width, we consequently obtain $\Phi(k,t)$ in Eq. (A.5) as the Fourier transform of $\mathrm{sgn}(r)$, giving $\Phi(k,t) \sim k^{-1}$, and therefore due to Eq. (A.4), $S(k,t) \sim k^{-2}$. For domain walls in dimension d higher then one, additional factors of $1/k$ arise due to the spatial extent of the domain walls, with the result $S(k) \propto k^{-(d+1)}$. In regions between the domain walls, the order parameter does not vary, and therefore there are no extra contributions to the structure factor for k values larger than the inverse domain size. We therefore obtain a structure factor that has a power-law form for k^{-1} in the range between the domain wall separation and the domain wall width. The decrease of the lower threshold k_p with time is then seen to be a consequence of the increase in the average domain size as the system evolves. For a given value of k in the power-law range, $S(k,t)$ is proportional to the total domain wall area in the system at the time t, which similarly explains the decay of the amplitude B in Eq. (A.6) with time.

Bray and Humayun [13] investigate in detail how the singular variation of the order parameter around a point or line defect in a system with continuous symmetry will likewise lead to an asymptotic power-law dependence on k of the structure factor $S(k,t)$. In this work, they calculate exactly the exponent and the amplitude of the contribution $Ak^{-\chi}$ to the structure factor coming from an isolated defect in the $O(N)$ vector model order parameter configuration. They then argue that in the region of large k, the structure factor of a system containing a number of topological defects can be obtained by multiplying $Ak^{-\chi}$ by the number of defects. The reason is as follows. Variations in the order parameter on very short scales (probed by $S(k,t)$ with k large) occur only in the singular regions surrounding the defect cores. It is therefore appropriate to treat the contribution from each defect independently, and as coming from a defect with a symmetrical (i.e., equilibrium) configuration, *provided that the configuration in the vicinity of the defect core is not affected by the presence*

of other defects. This last assumption of this reasoning is non-trivial: in fact, it was argued in Ref. [14] that for the case of point defects in the $O(3)$ vector model in $d = 3$, a singular, string-like configuration develops between the defects. It is not clear, however, to what degree the static calculation in Ref. [14] is relevant to the case of defect dynamics, and in fact the prediction for $S(k,t)$ based on the assumption of symmetrical defect cores has been found to be in good agreement with numerical simulations in several systems [15]. In the calculations we present in Secs. A.3–A.5, we shall assume that the regions close to the defect cores in a phase ordering system do possess the structure of an isolated defect, and we shall comment on the nature of possible corrections to our results in Sec. A.6.

The discussion in the previous paragraph leads us to the following formulation of the *generalized Porod law* for the structure factor of a system containing topological defects:

$$S(k,t) \sim A\rho(t)k^{-\chi}\,, \tag{A.7}$$

where $\rho(t)$ is the *defect density* (i.e., the domain wall area, string length, or number of point defects, per unit volume of the system), and A is a time-independent amplitude characterizing the given type of defect. The generalized Porod law is expected to be valid in the range $L(t)^{-1} \ll k \ll \xi^{-1}$, where $L(t)$ is the average separation between defects present in the system at time t, and ξ is the size of the defect cores. Specific cases exemplifying the validity of Eq. (A.7) will be given throughout the rest of the Paper. It will be seen that the Porod exponent χ is always given by $d+c$, where d is the dimensionality of the system, and c is the *co-dimension* of the topological defects (that is, $c = d$ for point defects, $c = d-1$ for string defects, and $c = d-2$ for domain walls). The amplitude A, however, depends in more detail on the order parameter in question. For example, we shall see that the amplitudes A for the nematic hedgehog and for the $O(3)$ monopole in $d = 3$ differ substantially.

A.3 O(N) symmetric vector systems

The exponent χ and the amplitude A of a contribution to $S(\mathbf{k},t)$ from a single defect in the configuration of an $O(N)$ vector model is computed in Ref. [13] by first calculating the real-space correlation function $C(\mathbf{r},t)$, Eq. (A.2), and then Fourier-transforming the result to obtain $S(\mathbf{k},t)$. During this calculation, the authors discard the "analytic terms" (see Ref. [13]), which do not contribute to the power-law part of the Fourier transform; also, for $O(N)$ systems with N even, the calculation is complicated by the appearance of logarithmic terms in the intermediate result for $C(\mathbf{r},t)$. We shall show below that the results of Ref. [13] can be obtained in a more simple way by working directly in Fourier space, i.e., by first Fourier-transforming the order-parameter configuration, and then using Eq. (A.4) to obtain the structure factor [21]. Besides being shorter, this method does not discard any terms, and does not involve any logarithmic terms.

A.3.1 Point defects in O(N) symmetric vector systems

We first perform the calculation for the case of the $O(N)$ vector model system in $d = N$ spatial dimensions. In this case, only point defects (i.e., hedgehogs) are topologically stable; the configuration of a stable point defect is described by (see [22])

$$\mathbf{\Phi}(\mathbf{r}) = \frac{\mathbf{r}}{r}. \tag{A.8}$$

Due to spherical symmetry, the Fourier transform of $\phi(\mathbf{r})$ takes the form

$$\mathbf{\Phi}(\mathbf{k}) = \mathbf{k}\, f(k^2)\,, \tag{A.9}$$

where f is a certain scalar function of the scalar k^2. Taking the scalar product of Eq. (A.9) with $\mathbf{k}$ and solving for f allows us to write

$$\mathbf{\Phi}(\mathbf{k}) = \mathbf{k}\, k^{-2} \int d^d r\, r^{-1}\, \mathbf{k}\cdot\mathbf{r}\, \mathrm{e}^{i\mathbf{k}\cdot\mathbf{r}} = -i\mathbf{k}\, k^{-2} \frac{\partial}{\partial\lambda}\bigg|_{\lambda=1} F(\lambda^2 k^2)\,, \tag{A.10}$$

where the function F is defined via

$$F(\lambda^2 k^2) \equiv \int d^d r\, r^{-1}\, \mathrm{e}^{i\lambda\mathbf{k}\cdot\mathbf{r}}\,, \tag{A.11}$$

i.e., F is the d-dimensional Fourier transform of the Coulomb potential r^{-1}, which can readily be shown, for $\mathbf{k} \neq \mathbf{0}$, to be

$$F(\lambda^2 k^2) = \frac{(4\pi)^{(d-1)/2}}{k^{d-1}} \Gamma\left(\frac{d-1}{2}\right). \tag{A.12}$$

Evaluating the derivative of F, and inserting it into Eq. (A.10), leads to

$$\mathbf{\Phi}(\mathbf{k}) = i\mathbf{k}(d-1)(4\pi)^{(d-1)/2} \Gamma\left(\frac{d-1}{2}\right) \frac{1}{k^{d+1}}. \tag{A.13}$$

The normalization factor $M_{O(N)}$, given by Eq. (A.3), is the volume V of the system. It follows from Eq. (A.4) that the structure factor of a single point defect $S(k)$ is then given by

$$S(k) = \frac{1}{V}\frac{1}{\pi}(4\pi)^d \Gamma\left(\frac{d+1}{2}\right)^2 \frac{1}{k^{2d}}. \tag{A.14}$$

For a system having ρ defects per unit volume, the factor V^{-1} is replaced by ρ. The expression A.14 is then seen to be in agreement with the result for $S(k)$ given in Ref. [13]. It should be noted that by fully exploiting the spherical symmetry at hand, this method enables us to pass from a calculation involving vector quantities to a calculation involving only scalar ones. In Sec. A.4.1, we will similarly be able to pass from a tensorial to a scalar calculation, appropriate for the case of the nematic order parameter.

A.3.2 Vortex lines in three-dimensional O(2) vector systems

We now turn to the case of line defects in $O(N)$ vector systems, specifically concentrating on the physically prominent case of vortex lines in three-dimensional $O(2)$ vector systems.

In the case of the spherically symmetric point defect in the $O(N)$ vector system, investigated in the previous subsection, the final result, Eq. (A.14), is independent of the orientation of the wave vector $\mathbf{k}$, due to the spherical symmetry. In contrast, the structure factor of a segment of a line defect does depend on the angle between $\mathbf{k}$ and the orientation of the line segment: $S(\mathbf{k})$ is dominated by contributions from

defect segments that are perpendicular to the vector $\mathbf{k}$, as there are no short-distance order-parameter gradients in the direction along the defect line. As we shall now see, the contribution to the structure factor from a straight segment of a line defect can readily be obtained by using the structure factor of the appropriate point defect in the planar system that forms the cross-section of the line defect, along with an appropriate additional factor. As we are ultimately concerned with large systems that are undergoing phase ordering under isotropic conditions, all orientations of defects occur with equal probability, and the resulting structure factor will be again isotropic.

We therefore begin by considering the structure factor of a single vortex line. Now, if the orientation of the defect line varies on a scale larger than k^{-1} then this orientation variation does not substantially influence the structure factor at wave vector k. Thus, for values of k^{-1} lying between the core size and the typical orientation variation length (i.e., the characteristic radius of curvature of the vortex lines) it is sufficient to consider straight vortex lines, and subsequently average over the their orientation.

Consider, then, a straight vortex line segment in $d = 3$ with its core located on $(x, y) = (0, 0)$, and extending from $z = -L/2$ to $z = L/2$. The order parameter $\mathbf{\Phi}$ does not depend on z, and the configuration of $\mathbf{\Phi}$ in the xy plane is identical to the configuration of a point defect in the corresponding $O(2)$ vector model in $d = 2$. Thus, the structure factor is given by

$$S(\mathbf{k}) = \mathbf{\Phi}(\mathbf{k}) \cdot \mathbf{\Phi}(-\mathbf{k}) = S^{(2)}(k_x, k_y) \int_{-L/2}^{L/2} dz\, e^{ik_z z} \int_{-L/2}^{L/2} dz'\, e^{-ik_z z'}\,, \qquad \text{(A.15)}$$

where $S^{(2)}(k_x, k_y)$ is the structure factor for the $d = 2$ point defect configuration. From Porod's law in $d = 2$ we have $S^{(2)}(k_x, k_y) = A^{(2)}/(k_x^2 + k_y^2)^2 \equiv A^{(2)}/k^4 \sin^4\theta$, where $A^{(2)} = 4\pi^2$ and θ is the angle between $\mathbf{k}$ and the defect orientation. Thus, we may write $S^{av}(k)$, i.e., the average of the structure factor $S(\mathbf{k})$ over all orientations of the defect, as

$$S^{av}(k) = \frac{A^{(2)}}{k^4} \frac{1}{2} \int_0^\pi d\theta \, \frac{\sin\theta}{\sin^4\theta} \int_{-L/2}^{L/2} dz\, e^{ikz\cos\theta} \int_{-L/2}^{L/2} dz'\, e^{-ikz'\cos\theta}\,. \qquad \text{(A.16)}$$

We now let $L \to \infty$ and calculate the structure factor per unit length of the defect, $S_u(k) = \lim_{L\to\infty} S^{av}(k)/L$. By using the identity

$$\lim_{L\to\infty} L^{-1} \int_{-L/2}^{L/2} dz \, \exp(iuz) \int_{-L/2}^{L/2} dz' \exp(-iuz') = 2\pi\delta(u) \tag{A.17}$$

we see that $S_u(k)$ can readily be evaluated:

$$S_u(k) = \pi A^{(2)} \frac{1}{k^5} \,. \tag{A.18}$$

exemplifying the generalized form of Porod's law, Eq. (A.7).

We therefore reach the conclusion that the Porod amplitude of a line defect in three dimensions, $A^{(3)}$, can be obtained from the Porod amplitude of the corresponding point defect in two dimensions, $A^{(2)}$, via

$$A^{(3)} = \pi A^{(2)} \,. \tag{A.19}$$

Specifically, by using the result (A.14) for $d = N = 2$ (i.e., $A^{(2)} = 4\pi^2$) we obtain the Porod amplitude corresponding to the $O(2)$ line defect in $d = 3$, viz., $A^{(3)} = 4\pi^3$, in agreement with Ref. [13].

A.4 Uniaxial nematic systems

A.4.1 Hedgehog defects in uniaxial nematic systems

For the case of nematic liquid crystals the local order-parameter field $Q_{\alpha\beta}(\mathbf{r}, t)$ is a symmetric, traceless, rank-2 tensor, with Cartesian indices $\alpha, \beta = 1, 2, 3$ (see, e.g., Ref. [23]). In general we may write

$$Q_{\alpha\beta} = \frac{3}{2} S_1 (u_\alpha u_\beta - \frac{1}{3}\delta_{\alpha\beta}) + \frac{1}{2} S_2 (b_\alpha b_\beta - v_\alpha v_\beta) \,, \tag{A.20}$$

where $\pm\mathbf{u}$ is the uniaxial director, $\pm\mathbf{b}$ is the biaxial director, $\mathbf{v} = \mathbf{u} \times \mathbf{b}$, and the amplitudes S_1 and S_2 determine, respectively, the strength of uniaxial and biaxial ordering. For the nematic, the real-space correlation function $C(\mathbf{r}, t)$ is defined as

$$C(\mathbf{r}, t) = \frac{1}{M_{\text{nem}}} \int d^3x \, \text{Tr} \left[Q(\mathbf{x}, t) \, Q(\mathbf{x} + \mathbf{r}, t) \right] , \tag{A.21}$$

where $\mathrm{Tr}[AB] \equiv A_{\alpha\beta}B_{\beta\alpha}$ [cf. Eq. (A.2)], and the normalization factor M_{nem} is given by

$$M_{\mathrm{nem}} = \int d^3x \, \mathrm{Tr}\left[Q(\mathbf{x},t)\, Q(\mathbf{x},t)\right]. \tag{A.22}$$

For the nematic, Eq. (A.4) becomes

$$S(\mathbf{k},t) = \frac{1}{M_{\mathrm{nem}}} \mathrm{Tr}\left[Q(\mathbf{k},t)\, Q(-\mathbf{k},t)\right]. \tag{A.23}$$

A three-dimensional uniaxial nematic system, for which $S_2 = 0$, admits topologically stable point defects (i.e., nematic hedgehogs) as well as line defects (i.e., nematic disclinations). (For a discussion of topological stability, see, e.g., Ref. [24].) In the configuration of the nematic hedgehog defect, the "director" points everywhere radially outwards from the center of the defect (up to a global rotation), and the configuration may therefore be expressed as (see [22])

$$Q_{\alpha\beta}(\mathbf{r}) = \frac{3}{2} S_1 \left(\frac{r_\alpha}{r} \frac{r_\beta}{r} - \frac{1}{3}\delta_{\alpha\beta} \right), \tag{A.24}$$

with S_1 independent of $\mathbf{r}$.

The following calculation of $S(\mathbf{k})$ closely mirrors the steps Eqs. (A.9)–A.14) in our $O(N)$ vector model calculation. First, we observe that the Fourier transform of $Q_{\alpha\beta}(\mathbf{r})$ is itself a symmetric, traceless, rank-2 tensor, and that due to symmetry it can depend only on the direction $\pm\mathbf{k}$. The general form of such a tensor is

$$Q_{\alpha\beta}(\mathbf{k}) = \frac{3}{2} S_1 (k_\alpha k_\beta - \frac{1}{3}\delta_{\alpha\beta}\, k^2)\, g(k^2), \tag{A.25}$$

where $g(k^2)$ is an scalar function of the scalar k^2. By contracting Eq. (A.25) with $k_\alpha k_\beta$ and solving for g we can rewrite Eq. (A.25) as

$$\begin{aligned} Q_{\alpha\beta}(\mathbf{k}) &= \frac{9S_1}{4k^4} \left(k_\alpha k_\beta - \frac{1}{3}\delta_{\alpha\beta}\, k^2 \right) \int d^3r \left[\left(\frac{\mathbf{k}\cdot\mathbf{r}}{r} \right)^2 - \frac{k^2}{3} \right] \mathrm{e}^{i\mathbf{k}\cdot\mathbf{r}} \\ &= -\frac{9S_1}{4k^4} \left(k_\alpha k_\beta - \frac{1}{3}\delta_{\alpha\beta}\, k^2 \right) \left[(2\pi)^3 \frac{k^2}{3} \delta(\mathbf{k}) + \left. \frac{\partial^2}{\partial\lambda^2} \right|_{\lambda=1} G(\lambda^2 k^2) \right]. \end{aligned} \tag{A.26}$$

The δ-function part corresponds to the forward-scattered beam, and will be dropped henceforth, as it does not influence the large-k behavior. The function G is defined

via

$$G(\lambda^2 k^2) \equiv \int d^d r \, r^{-2} \, \mathrm{e}^{\mathrm{i}\lambda \mathbf{k}\cdot\mathbf{r}} \,, \tag{A.27}$$

i.e., G is the d-dimensional Fourier transform of the potential r^{-2}, which can readily be shown to be

$$G(\lambda^2 k^2) = \frac{2\pi^2}{\lambda k} \,. \tag{A.28}$$

Evaluating the second derivative of G, and inserting it into Eq. (A.26), leads to

$$Q_{\alpha\beta}(\mathbf{k}) = -\frac{9\pi^2 S_1}{4k^5} \left(k_\alpha k_\beta - \frac{1}{3}\delta_{\alpha\beta} \, k^2 \right) \,. \tag{A.29}$$

¿From Eq. (A.22) we see that the normalization factor M_{nem} takes the value $3VS_1^2/2$. Thus, combining Eqs. (A.23) and (A.29) gives for the structure factor $S(k)$ of a single nematic hedgehog defect in a system of volume V

$$S(k) = \frac{36\pi^4}{V} \frac{1}{k^6} \,. \tag{A.30}$$

A.4.2 Disclination lines in uniaxial nematic systems

We now address the issue of the calculation of $S(\mathbf{k})$ for the case of a disclination line defect in a uniaxial nematic system. It should be clear from the derivation given in Sec. A.3.2 that Eq. (A.19), which relates the Porod-law amplitude for a line defect in $d = 3$ with that of the corresponding point defect in $d = 2$, is valid independently of the order parameter in question and may, therefore, also be used for nematic systems.

In the point defect configuration in a two-dimensional uniaxial nematic (corresponding to the cross-section of a disclination line) the director rotates about the core by 180° (see, e.g., Ref. [24]). The approach of Sec. A.4.1, which is based on rotational symmetry, cannot therefore be directly applied. It is readily seen, however, that the calculation of the Porod-law amplitude for the 180° nematic defect can be mapped on to the corresponding calculation for the 360° defect in the $O(2)$ model in $d = 2$. For the 180° uniaxial nematic defect, the order-parameter configuration is given by Eq. (A.20) with $S_2 = 0$ and $\mathbf{u}(\mathbf{x}) = (\cos\frac{1}{2}\phi(\mathbf{x}), \sin\frac{1}{2}\phi(\mathbf{x}), 0)$, where $\phi(\mathbf{x})$ is

the polar angle for the radius vector $\mathbf{x}$ in the plane perpendicular to the disclination line. The correlation function Eq. (A.21) then becomes

$$C^{(2)}_{180^\circ}(r) = \frac{(3S_1/2)^2}{M_{\rm nem}} \int d^2x \, \cos^2[\frac{1}{2}\phi(\mathbf{x}) - \frac{1}{2}\phi(\mathbf{x}+\mathbf{r})] + k_1 \qquad \text{(A.31)}$$

$$= \frac{(3S_1/2)^2}{M_{\rm nem}} \int d^2x \, \frac{1}{2} \cos[\phi(\mathbf{x}) - \phi(\mathbf{x}+\mathbf{r})] + k_2 \,, \qquad \text{(A.32)}$$

where k_1 and k_2 are numerical constants. On the other hand, for the 360° defect in the $O(2)$ model in $d = 2$, the order-parameter configuration is given by $\mathbf{\Phi}(\mathbf{x}) = (\cos\phi(\mathbf{x}), \sin\phi(\mathbf{x}))$, and the corresponding correlation function, Eq. (A.2), is

$$C^{(2)}_{360^\circ}(r) = \frac{1}{M_{O(2)}} \int d^2x \, \cos[\phi(\mathbf{x}) - \phi(\mathbf{x}+\mathbf{r})] \,. \qquad \text{(A.33)}$$

After Fourier-transforming Eqs. (A.32,A.33) and omitting the δ-function term arising from the constant k_2 in Eq. (A.33), we obtain that the structure factors of the two defects are related simply by

$$S^{(2)}_{180^\circ}(k) = \frac{(3S_1/2)^2 M_{O(2)}}{2M_{\rm nem}} S^{(2)}_{360^\circ}(k) \,. \qquad \text{(A.34)}$$

Using the result $S^{(2)}_{360^\circ}(k) = A^{-1} 4\pi^2 k^{-4}$ (i.e., Eq. (A.14) for $d = 2$, with the area of the system denoted by A), and the normalization factors $M_{O(2)} = A$, $M_{\rm nem} = A3S_1^2/2$, we finally obtain the structure factor $S^{(2)}_{180^\circ}(k)$ for the 180° point defect in a two-dimensional nematic:

$$S^{(2)}_{180^\circ}(k) = \frac{1}{A} 3\pi^2 \frac{1}{k^4} \,. \qquad \text{(A.35)}$$

By using Eq. (A.18) we find that the contribution to the structure factor from a segment of length L of a nematic disclination is given by

$$S(k) = \frac{L}{A} 3\pi^3 \frac{1}{k^5} \,. \qquad \text{(A.36)}$$

In a system with numerous disclination lines, the area A in Eq. (A.36) is determined by D^2, where D is the average distance (in the direction perpendicular to the considered disclination segment) to the next disclination line. It follows that the structure factor is given by $S(k) = \rho 3\pi^3 k^{-5}$, with the defect density ρ having the meaning of the *total disclination length per unit volume of the system.*

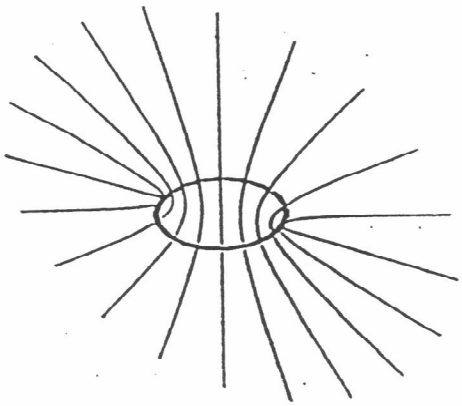

Figure A.1: Order parameter configuration around a ring defect in a uniaxial nematic system.

A.4.3 Ring defects in uniaxial nematic systems

Next, we investigate the structure factor for a ring defect formed by a closed-loop wedge disclination. The configuration of the director around such a defect (up to a global rotation) is depicted in Fig. A.1. The energetic stability of such a configuration was investigated in Refs. [25] and [26]. There, it was found that (provided that cetain restrictions on the elastic constants in the nematic free energy are satisfied) there exists an equilibrium radius of the loop, for which the ring defect is stable: a ring of a larger (smaller) radius will tend to shrink (expand). This prediction was recently verified in numerical simulations [27]. The existence of a nonzero equilibrium radius is connected to the fact that at large length-scales (larger than the ring radius), the nematic ring has the configuration of a topologically stable point defect—the nematic hedgehog (see Fig. A.1). The singularity associated with the ring defect cannot therefore be removed by shrinking the ring to zero size; rather, the ring will stop shrinking at a finite radius R_{eq}, where the energy of the ring configuration has a minimum (and is lower than the energy of a hedgehog). Depending on the values

of the nematic elastic constants, Ref. [26] predicts R_{eq} in the range 10ξ–$10^4\xi$, where ξ is the nematic coherence length (i.e., ξ is of the order of 10–100 Å).

It is readily seen that the topologically nontrivial nature of the ring defect configuration at large scale leads to the presence of two distinct Porod law regimes in the structure factor $S(k)$ characterizing such a defect. For $k < 1/R$, where R is the ring radius, $S(k)$ probes correlations on length scales larger than R, leading to a power-law contribution characterizing the nematic hedgehog (Eq. A.30) in $d = 3$:

$$S(k) = 36\pi^4 \frac{1}{k^6} . \tag{A.37}$$

For $1//\xi < k < 1/R$, the function $S(k)$ probes the configuration in the vicinity of the disclination core, leading to a power-law characterizing the nematic disclination of length $2\pi R$, which is, from Eq. (A.36),

$$S(k) = 6\pi^4 R \frac{1}{k^5} . \tag{A.38}$$

Therefore, the large-k region of the structure factor measured in a system containing nematic ring defects of equal size R, separated by an average distance larger than R, is expected to exhibit a crossover between two power-law regimes with exponents 6 and 5 (Fig. A.2). The crossover point, as defined in Fig. A.2 , is predicted to occur at the value of $k_c = 6/R$. Note that this allows us to obtain information on the ring defect size R from *un-normalized* data for $S(k)$; this is in contrast to the standard use of the Porod law, where the total string length is extracted from the normalized structure factor. In principle, the Porod tail crossover may be used to monitor the dynamics of the population of shrinking (expanding) loops with radii R larger (smaller) than the equilibrium radius.

It should be noted that the assumption that the ring defects are well separated (i.e., that the average distance between the rings is larger than their radius) is important—otherwise, the k^{-6} Porod regime will be suppressed. Based on the experience from simulations of phase ordering in $O(2)$ vector model systems [28], one may expect that a configuration satisfying such an assumption will develop in the late

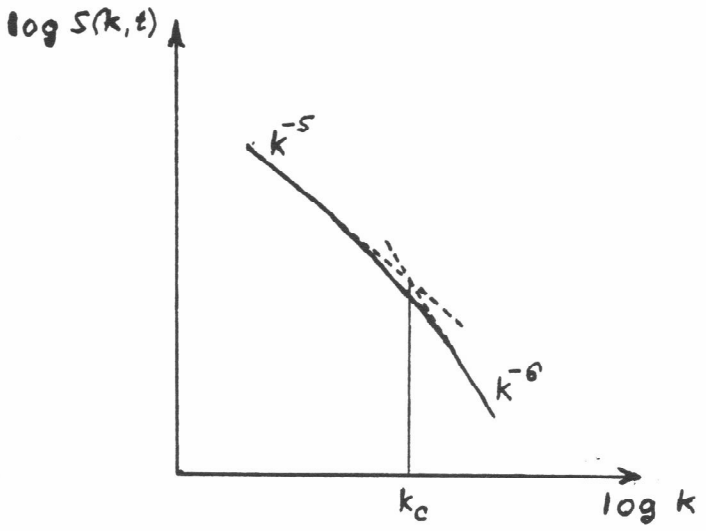

Figure A.2: Structure factor $S(k)$ of the ring defect configuration in Fig. A.1. The two Porod regimes, arising for length scales much larger and much smaller than the ring radius R, are shown as the dashed line ($S(k) = 36\pi^4 k^{-6}$) and the dotted line ($S(k) = 6\pi^4 R k^{-5}$), respectively. The solid curve schematically shows the crossover between the two power-law regimes. The crossover wavevector k_c, as defined in the picture, is given by $k_c = 6/R$.

stages of ordering following an off-critical quench in a uniaxial nematic system (to our knowledge, such a quench has not been investigated experimentally or numerically).

The ring defects in a configuration generated during a critical quench are not expected to be of uniform size; rather, a wide distribution of ring sizes, spanning the interval from the core size ξ to the average ring separation D, is expected. If the number density $n(R,t)$ of rings of radius R were known, the structure factor for wave vectors k such that typical ring separation is larger than k^{-1} would be given by [29]

$$S(k,t) = L_{\rm tot}(t) 3\pi^3 \frac{1}{k^5} + N_{\rm tot}(t) 36\pi^4 \frac{1}{k^6}\,, \tag{A.39}$$

where $L_{\rm tot}(t) \equiv \int_{1/k}^{D} dR\, 2\pi R\, n(R,t)$ is the total disclination length in rings with radii $R > 1/k$, and $N_{\rm tot}(t) \equiv \int_{\xi}^{1/k} dR\, n(R,t)$ is the total number of rings with radii $R < 1/k$. Equation (A.39) could, in principle, be used to extract the size distribution $n(R,t)$ from a measured structure factor $S(k,t)$.

Parenthetically, we comment on the differences between the dynamics of nematic ring defects and of vortex loop defects in the $O(2)$ model in three spatial dimensions. The $O(2)$ vortex loop defect does not have the structure of a topologically non-trivial point defect at large length-scales, and is therefore unstable towards shrinking to zero size. By equating the flux (in number density space) of shrinking vortex loops at a given scale to the rate of annihilation of the loops and assuming dynamical scaling, it is possible to derive [30] the R-dependence of the number density of such defects $n(R)$. In the case of nematic rings, however, $n(R)$ is expected to develop a strong maximum at the equilibrium ring radius, so that the scaling approach cannot be applied directly.

It should be noted, however, that in the experimental investigations of phase ordering in nematic liquid crystals [7], numerous disclination loops that are apparently composed of disclination segments with opposite winding numbers were observed. Such defects do not have a hedgehog-like structure at large length-scales, and therefore behave like $O(2)$ vortex loops (in the sense that only the Porod-law regime with exponent 5 is exhibited in the structure factor), rather than like the nematic ring defects investigated in the present section [31]. It is, consequently, not clear to what degree the calculations in this section are relevant to the recent Porod-tail measurements reported in Refs. [8, 9], in which the value of the Porod exponent was reported to lie close to 6, even though disclinations, rather than hedgehogs, are believed to dominate in phase-ordering nematic systems [6, 7, 27, 32].

A.5 Biaxial nematic systems

Thus far, our discussion of defects in nematics has concentrated on the case of uniaxial systems. It is straightforward to generalize this discussion to the case of biaxial systems. As there are no topologically stable point defects in a three-dimensional biaxial nematic [24], we need only consider line defects. Biaxial nematics admits four topologically distinct classes of line defects [24], which are disclination lines distinguished

by the angles of rotation of the uniaxial director **u** and the biaxial director **b** [defined in Eq. (A.20)] around the defect core. In the C_x class of disclinations **u** rotates by $\pm 180°$ and **b** does not rotate; in C_y disclinations **u** does not rotate and **b** rotates by $\pm 180°$; in C_z disclinations both **u** and **b** rotate by $\pm 180°$; finally, in $\overline{C}_0$ disclinations either **u** or **b** (or both) rotate by 360°. These four distinct disclination types were observed experimentally in a thermotropic nematic polymer [20], and their properties where found to be in agreement with the predictions of the topological classification scheme.

In the minimum energy configuration for the C_x, C_y, and C_z defects, the 180° rotations of the **u** and **b** director are uniform [33]. The configuration of a C_x disclination is correspondingly given (up to a global rotation) by Eq. (A.20) with

$$\mathbf{u}(\mathbf{x}) = (\cos\frac{1}{2}\phi(\mathbf{x}), \sin\frac{1}{2}\phi(\mathbf{x}), 0), \tag{A.40}$$

$$\mathbf{b}(\mathbf{x}) = (0, 0, 1), \tag{A.41}$$

$$\mathbf{v}(\mathbf{x}) = (\cos(\frac{1}{2}\phi(\mathbf{x}) + \frac{\pi}{4}), \sin(\frac{1}{2}\phi(\mathbf{x}) + \frac{\pi}{4}), 0), \tag{A.42}$$

where $\phi(\mathbf{x})$ is the polar angle in the plane perpendicular to the disclination. The correlation function (A.21) for this configuration can be expressed (up to an additive constant) as the correlation function (A.32) for the uniaxial nematic disclination, multiplied by the biaxiality-strength–dependent factor $R(3S_1 + S_2)^2/4$, where $R \equiv 3S_1^2/(3S_1^2 + S_2^2)$ is the ratio of the uniaxial ($S_2 = 0$) and biaxial ($S_2 \neq 0$) normalization factors M_{nem}. The corresponding factors for the case of the C_y and C_z disclinations are likewise readily evaluated. By using the result (A.36) for the uniaxial disclination, we obtain the structure factors per unit length for the biaxial disclinations C_x, C_y and C_z:

$$S(k)_{C_x} = \frac{3\pi^2}{2}\frac{3}{4}\frac{S_1^2(3S_1 + S_2)^2}{3S_1^2 + S_2^2}\frac{1}{k^5}, \tag{A.43}$$

$$S(k)_{C_y} = \frac{3\pi^2}{2}3\frac{S_1^2 S_2^2}{3S_1^2 + S_2^2}\frac{1}{k^5}, \tag{A.44}$$

$$S(k)_{C_z} = \frac{3\pi^2}{2}\frac{3}{4}\frac{S_1^2(3S_1 - S_2)^2}{3S_1^2 + S_2^2}\frac{1}{k^5}. \tag{A.45}$$

It should be noted that in the case $3S_1 = S_2$, the amplitude in the Porod law for the C_z defect is zero, whereas the amplitudes for the C_x and C_y defects are non-zero and equal [see Eqs. (A.43)–(A.45)]. This reflects the fact that for $3S_1 = S_2$, the order parameter (A.20) describes a *uniaxial discotic* phase [34] with uniaxial axis **v**. Correspondingly, the C_z configuration in this case does not represent a defect (**v** does not rotate), whereas the C_x and C_y configurations are equivalent.

It remains to consider the $\overline{C}_0$ disclination. For the case $S_1 > S_2$ (i.e., needle-like ordering [34]), the minimum energy configuration of type $\overline{C}_0$ is given by Eq. (A.20) with

$$\mathbf{u}(\mathbf{x}) = (0,0,1), \tag{A.46}$$

$$\mathbf{b}(\mathbf{x}) = (\cos\phi(\mathbf{x}), \sin\phi(\mathbf{x}), 0), \tag{A.47}$$

$$\mathbf{v}(\mathbf{x}) = (\cos(\phi(\mathbf{x}) + \frac{\pi}{4}), \sin(\phi(\mathbf{x}) + \frac{\pi}{4}), 0), \tag{A.48}$$

where $\phi(\mathbf{x})$ is the polar angle in the plane perpendicular to the disclination. The correlation function (A.21) for the point defect in the planar cross-section through this disclination can then be expressed as $R(2S_2/3S_1)^2$, By using Eq. (A.18) one obtains the structure factor per unit length of the $\overline{C}_0$ disclination:

$$S(k) = 12\pi^2 \frac{S_2^2}{3S_1^2 + S_2^2} \frac{1}{k^5}. \tag{A.49}$$

For the case $S_1 < S_2$ (i.e., discotic ordering [34]) the **v** director (and not the **u** director, in contrast with the needle-like case) corresponds to the eigenvalue of the order parameter tensor $Q_{\alpha\beta}$ largest in absolute value, and the lowest energy configuration that can be taken by the $\overline{C}_0$ disclination has directors

$$\mathbf{u}(\mathbf{x}) = (\cos\phi(\mathbf{x}), \sin\phi(\mathbf{x}), 0), \tag{A.50}$$

$$\mathbf{b}(\mathbf{x}) = (\cos(\phi(\mathbf{x}) + \frac{\pi}{4}), \sin(\phi(\mathbf{x}) + \frac{\pi}{4}), 0), \tag{A.51}$$

$$\mathbf{v}(\mathbf{x}) = (0,0,1). \tag{A.52}$$

The corresponding structure factor is

$$S(k) = \frac{8}{3}\pi^2 \frac{(3S_1^2 - S_2)^2}{3S_1^2 + S_2^2} \frac{1}{k^5}. \tag{A.53}$$

Finally, we note that in a biaxial nematic film (i.e., a system having two spatial dimensions but three dimensions for the nematic order parameter), C_x, C_y, C_z and $\overline{C}_0$ are point-like defects (the dynamics of which was studied in [19]). The Porod-law amplitudes for these defects are obtained from the amplitudes in the results (A.43)–(A.45), (A.49) and (A.53) by dividing by π [see Eq. (A.19)], and the corresponding Porod-law exponents take the value 4 instead of 5.

A.6 Corrections to Porod's law

An interesting question, already alluded to in Sec. A.2, is whether the order parameter configuration in the vicinity of the defect core is or is not affected by the interactions with the other defects present in the system. [In other to avoid confusion with the core region, where the order parameter magnitude is reduced, we shall refer to the region close to, but outside, the core, as the "central" defect region.] It is important to distinguish the static and the dynamic effects. In the case of the $O(2)$ model with the usual gradient free energy given by $\int dx^d (\nabla \mathbf{m})^2$, the minimum energy configuration of a collection of defects with fixed locations is obtained simply by taking the superposition of the angles characterizing the order parameter $\mathbf{m}$ around isolated defects; their central regions are therefore not affected. A deformation does occur, however, once the defects are allowed to move [35]. For sufficiently slow defect velocities, this effect may be neglected. The situation is different in the $O(3)$ model case. Here, Ostlund [14] showed that the energy minimization argument for a monopole-antimonopole pair leads to the concentration of the gradient energy along a string connecting the two point defects. We are not aware of any investigation of how this argument would get modified in a dynamical situation.

Independently of the precise nature of the deformation of the central defect region, it is possible to make a general argument about it's effect on the Porod amplitude A. We use the connection between the gradient free energy E_{el} and the structure factor

$S(k)$,

$$E_{el} = \int dx^d (\nabla \mathbf{m})^2 = \int dk^d k^2 S(k). \tag{A.54}$$

Deforming the symmetrical ($\mathbf{m} = \mathbf{x}/x$) order parameter configuration in any smooth way increases E_{el}, but cannot change the exponent χ in the Porod law $S(k) = Ak^{-\chi}$; Eq. (A.54) then implies an increase in A. We therefore reach the conclusion that a defect configuration minimizing the free energy of form $\int dx^d (\nabla \mathbf{m})^2$ gives the minimum possible value of the Porod amplitude A for the given type of defect. Indeed, it was found in a numerical investigation [36] of the Porod law from a point defect in the $O(2)$ model in $d = 2$ that the amplitude A increased (and the exponent χ remained unchanged) when the defect configuration was deformed.

It should be noted that the direct connection Eq. (A.54) between E_{el} and $S(k)$ is valid only if the energy density has the standard $(\nabla \mathbf{m})^2$ form, or in the case of the nematic order parameter, the simplest possible form $(\partial_\alpha Q_{\beta\gamma})(\partial_\alpha Q_{\beta\gamma})$. In the general case of unequal nematic elastic constants, the Porod amplitude A is no longer necessarily minimal for the equilibrium defect configuration.

References

[1] J. D. Gunton, M. San Miguel and P. S. Sahni, in *Phase Transitions and Critical Phenomena*, Vol. 8, C. Domb and J. L. Lebowitz, Eds., (Academic Press, New York, 1983).

[2] A. J. Bray, Adv. Phys. **43**, 357 (1994).

[3] T. W. B. Kibble, J. Phys. A**9**, 1387 (1976).

[4] A. Vilenkin and E. P. S. Shellard, *Cosmic Strings and other Topological Defects* (Cambridge University Press, 1994).

[5] B. D. Gaulin, S. Spooner and Y. Morii, Phys. Rev. Lett. **59**, 668 (1987).

[6] I. Chuang, R. Durrer, N. Turok and B. Yurke, Science **251**, 1336 (1991).

[7] I. Chuang, B. Yurke, A. N. Pargelis and N. Turok, Phys. Rev. E **47**, 3343 (1993).

[8] A. P. Y. Wong, P. Wiltzius and B. Yurke, Phys. Rev. Lett. **69**, 3583 (1992).

[9] A. P. Y. Wong, P. Wiltzius, R. G. Larson and B. Yurke, Phys. Rev. E **47**, 2683 (1993).

[10] G. F. Mazenko, Phys. Rev. B **42**, 4487 (1990).

[11] A. J. Bray and K. Humayun, Phys. Rev. E **48**, 1609 (1993).

[12] M. Mondello and N. Goldenfeld, Phys. Rev. A **42**, 5865 (1990).

[13] A. J. Bray and K. Humayun, Phys. Rev. E **47**, 9 (1993).

[14] S. Ostlund, Phys. Rev. B **24**, 485 (1981).

[15] R. E. Blundell and A. J. Bray, Phys. Rev. E **49**, 4925 (1994).

[16] A. J. Bray, S. Puri, R. E. Blundell and A. M. Somoza, Phys. Rev. E **47**, 2261 (1993).

[17] P. Debye, H. R. Anderson and H. Brumberger, J. Appl. Phys. **28**, 679 (1957).

[18] G. Porod, in *Small-Angle X-Ray Scattering*, edited by O. Glatter and O. Kratky (Academic, New York, 1982).

[19] M. Zapotocky, P. M. Goldbart and N. Goldenfeld, Phys. Rev. E **51**, 1216 (1995).

[20] T. De'Neve, M. Kleman and P. Navard, J. Phys. II (France) **2**, 187 (1992).

[21] This method was already used in Ref. [12] to obtain the Porod exponent for defects in the two-dimensional $O(2)$ symmetric vector model.

[22] Note that we have omitted any spatial variation in the amplitude of the order parameter. This corresponds to our focusing on length scales larger that the so-called core of the defect, in which the competition between condensation and gradient free energies gives rise to significant modification of the order-parameter amplitude(s).

[23] see, e.g., P.-G. de Gennes and J. Prost, *The Physics of Liquid Crystals* (Clarendon, Oxford, 1993).

[24] N. D. Mermin, Rev. Mod. Phys. **51**, 591 (1979).

[25] H. Mori and H. Nakanishi, J. Phys. Soc. Jpn. **57**, 1281 (1988).

[26] O. D. Lavrentovich and E. M. Terentjev, unpublished.

[27] H. Toyoki, J. Phys. Soc. Jpn. **63**, 4446 (1994).

[28] M. Mondello and N. Goldenfeld, Phys. Rev. A **45**, 657 (1992).

[29] We thank Andrew Rutenberg for a useful discussion on the effect of the distribution of the ring sizes.

[30] A. D. Rutenberg and A. J. Bray, Phys. Rev. E **51**, 5499 (1995).

[31] The Porod-law regime with exponent 6 is also expected to be absent from the structure factor arising from satellite defect rings, which have been predicted to occur around macroscopic particles suspended in a nematic liquid crystal [see, e.g., E. M. Terentjev, Phys. Rev. E **51**, 1330 (1995)]. Here, the effect of the ring defect is to compensate for the radial boundary condition on the director at the surface of the particle, thus permitting a homogeneous director configuration at large distances from the particle (without the need for other particles or defects).

[32] M. Hindmarsh, Phys. Rev. Lett. **75**, 2502 (1995).

[33] Ch. Kobdaj and S. Thomas, Nucl. Phys. B **438**, 607 (1995).

[34] See Ref. [23], or the discussion in Sec. II of Ref. [19].

[35] L. M. Pismen and J. D. Rodriguez, Phys. Rev. **A** 42, 2471 (1990).

[36] A. D. Rutenberg, private communication.

Vita

Martin Zápotocký was born in Prague, Czechoslovakia, on May 18, 1966. He grew up both in Prague and in Geneva, Switzerland, where his family worked for extended periods of time. After graduating from the Wilhelm Pieck Gymnasium in Prague, he enrolled, in 1984, as a student at the Faculty of Mathematics and Physics of Charles University, Prague, and obtained his RNDr. (Dipl.) degree from the Department of Mathematical Physics in 1989. The beginning of his graduate study at the Institute of Physics, Czechoslovak Academy of Sciences, was interrupted by a one-year military service as a communications officer in the Czechoslovak Army. In September 1990, he became a graduate student in the Physics Department of Columbia University in New York, and obtained the M.A. degree in February 1992. In June 1992, he transfered to the University of Illinois at Urbana-Champaign to pursue his Ph.D. in condensed matter theory. While at the University of Illinois, he was supported by a Physics Department fellowship, a teaching assistantship, and research assistantships administered through the Materials Research Laboratory.